Swansea University

Double Rotating Wall Compression of Positron Clouds and Towards Resistive Cooling

Hywel Turner Evans MPhys

Submitted to Swansea University in fulfilment of the requirements for the Degree of Doctor of Philosophy

Department of Physics
College of Science

2022

Abstract

Low energy positron clouds from a buffer gas trap have been characterised and compressed by a novel double rotating wall (RW) electric field. A theoretical and experimental study comparing compression due to dipolar single and double RW electric fields is presented, with details of a custom-built function generator capable of operating on two sets of four, six, and eight-segment electrodes. The installation of a cylindrical Penning trap with two sets of six-segment RW electrodes has allowed the implementation of a double RW, which provides a better approximation to the electric potential in the model for independent charged particle compression. A reduction in particle heating has been observed with the double RW, whilst obtaining at least equivalent compression as the single RW, which may in future allow a reduction in the minimum attainable cloud width.

Without the use of RW electric fields, optimisations to positron ejection and recapture techniques led to positron clouds being held in a deep, harmonic potential well for over 100 s, enabling time to study RW electric fields and to perform resistive cooling experiments.

Crynodeb

Mae cymylau o bositronau egni isel sy'n dod o drap nwy byffer wedi cael eu nodweddu a hefyd wedi'u cywasgu gan faes trydanol wal cylchdroöl (RW) dwbl newydd. Cyflwynir astudiaeth ddamcaniaethol ac arbrofol sy'n cymharu'r cywasgiad gan feysydd trydanol deupol RW sengl a dwbl, a hefyd cynhwysir manylion am eneradur ffwythiant a gafodd ei adeiladu'n arbennig gyda'r gallu i weithredu dwy set o electrodau segmentiedig gyda phedwar, chwech neu wyth segment. Gosodwyd trap Penning silindrog gyda dwy set o electrodau RW chwe-segment i weithredu'r RW dwbl, sy'n rhoi brasamcan gwell o'r potensial trydanol sydd yn y model ar gyfer cywasgu gronynnau gwefredig annibynnol. Gwelwyd gostyngiad mewn gwresogiad gronynnau gyda'r RW dwbl, tra bod o leiaf cywasgiad sy'n gyfatebol â'r RW sengl. Yn y dyfodol, gallai hyn ganiatáu gostyngiad mewn isafswm lled cwmwl o ronynnau gwefredig.

Heb ddefnyddio meysydd trydanol RW, arweiniodd optimeiddiaeth o'r technegau allyrru ac ail-ddal positronau at gymylau yn cael eu trapio mewn pant potensial dwfn harmonig am dros 100 s, gan roi amser digonol i astudio meysydd trydanol RW ac i berfformio arbrofion oeri gwrtheddol.

Declarations and Statements

Declaration

This work has not previously been accepted in substance for any degree and is not being concurrently submitted in candidature for any degree.

Signed: [redacted] ..... (Candidate)

Date: 26/11/2021

Statement 1

This work is the result of my own investigations, except where otherwise stated. Other sources are acknowledged by footnotes giving explicit references and a bibliography is appended.

Signed: [redacted] ..... (Candidate)

Date: 26/11/2021

Statement 2

I hereby give consent for my thesis, if accepted, to be available for photocopying and for inter-library loan, and for the title and summary to be made available to outside organisations.

Signed: [redacted] ..... (Candidate)

Date: 26/11/2021

Contents

Acknowledgements

Most of my thanks go to Dr Aled Isaac who is a great educator and always made time for me. I enjoyed my studies and learnt a vast amount from him. Not every supervisor trusts their PhD student to do a live liquid nitrogen show at a youth festival.

A presentation about antimatter by Professor Mike Charlton originally convinced me to study undergraduate Physics and I have been hooked ever since, so he has a lot to answer for, and I have a lot to thank him for. His feedback on my work was invaluable and I invariably learnt something when in his company. In addition, I would like to thank Dr Chris Baker for thorough discussions about my data and for his mantra that the beamline should be used as much as possible, as it won't work for long. He was right, although even he had not foreseen that a lengthy shutdown could be caused by a virus. As my internal assessor, Dr William Bryan provided advice from outside my positron-centric world, for this I was thankful. Some words of wisdom from Professor Dirk van der Werf also stuck with me throughout: "if it was easy, then everyone would do it". I now appreciate why everyone does not do it.

This work was supported by research scholarships from the Coleg Cymraeg Cenedlaethol (YSG17/04) and the College of Science, Swansea University. The Coleg Cymraeg Cenedlaethol were unequivocally supportive of me throughout these studies and the pandemic. I would especially like to thank Dr Dylan Phillips and Lois McGrath – diolch yn fawr iawn. I have had many opportunities to share my experiences as a physicist and to hear from researchers in wide-ranging fields, which I believe has made me a better scientist, communicator, and citizen of Cymru.

The College of Science technical support staff were supportive by both name and nature, these were Julian Kivell, Hugh Thomas, Phil Hopkins, and Jonathan Woodman-Ralph, who were always nearby to lend their expertise and to put things in perspective. Visiting the workshop was like going to a sweet shop. Their knowledge was vital to the experiment and hearing tales from the past ensured I was aware of my finite lifetime as a student. During the first year, I enjoyed studying alongside Donovan Newson, which

was lucky as we spent a considerable amount of time training together. I would also like to wish Rob Clayton and Phil John all the best with the remainder of their studies in the positron group.

The administrative team of Gill Oliver, Liz Kenny, Sian Conti, Carolyn Martin, and Sara Fenn always endeavoured to help with paperwork and lend an ear – I was thankful for their patience. There were also many interesting lunchtime discussions with the rest of the staff in the Physics department, putting the world to rights whilst overlooking Swansea Bay.

I would like to express my inexpressible thanks to Meg for being so understanding and supportive throughout my time at university, she saw the highs and the lows – diolch o galon. Spending time with friends also provided a welcome tonic and their faith in me often gave me a boost, although they may not have realised it. Finally, my family gave me the freedom to choose what I wanted to do and only ever tried to pressure me to work less, for that I am very grateful. These years were the hardest of my life for many reasons but I always aimed to make you proud.

List of Figures

List of Tables

List of Symbols

This list describes several symbols used within the body of the document.

$\mathbf{v}$	Vectors are given in bold typeface
$\hat{\mathbf{z}}$	Unit vectors are given using 'hat' notation
$\mathbf{r}$	The radial vector ($\mathbf{r} = x\hat{\mathbf{x}} + y\hat{\mathbf{y}}$)
$\dot{x}$, $\ddot{x}$	Dot notation for first and second derivatives with respect to time
∇	The gradient operator
∇^2	The Laplace operator
$\exp(x)$	The exponential function (e^x)
$I_n(x)$	The modified Bessel function of the first kind of order n, with argument x
∞	Infinity
ϵ_0	The permittivity of free space
μ_0	The permeability of free space
π	Pi ($3.14159\ldots$)
c	The speed of light in a vacuum
e	The elementary charge
h	The Planck constant
i	The imaginary unit ($\sqrt{-1}$)
k_B	The Boltzmann constant
m_e	The electron mass

Chapter 1

Introduction

> "We are obsessed with ourselves, we study *our* history, *our* psychology, *our* gods. Much of our knowledge revolves around man himself, as if we were the most important thing in the universe. I think I like physics because it opens a window through which we can see further. It gives me the sense of fresh air entering the house."
>
> Carlo Rovelli [2018]

During the Big Bang, our current understanding is that matter and antimatter should have been created in equal amounts. Despite this, the observable universe has more matter than antimatter [Farrar and Shaposhnikov, 1993] and this baryon asymmetry cannot be explained by the standard model which accounts for the electromagnetic, weak and strong interactions, nor general relativity which accounts for gravitational interactions. The origin of matter is still one of the great unanswered mysteries in physics. Dark matter [de Swart *et al.*, 2017] and dark energy [Peebles and Ratra, 2003] also point towards physics beyond the standard model, and it is therefore possible that the study of antimatter will further our understanding of the universe.

1.1 Positrons

Antimatter was predicted in 1931 by Paul Dirac [Dirac, 1931]. When attempting to unify the theory of special relativity with quantum mechanics, he discovered that there were negative solutions for the electron (e^-) energy [Dirac, 1928]. As negative solutions have importance in quantum mechanics and cannot be ig-

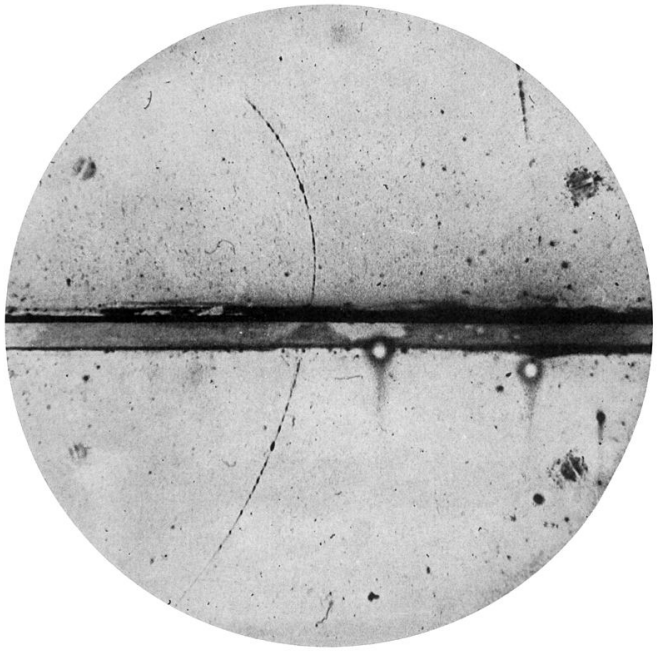

Figure 1.1: The first published image of a positron in 1933 by Carl Anderson [Anderson, 1933]. The positron came from a cosmic ray and was detected in a cloud chamber. The positron travelled through a 6 mm thick lead plate from below to above, with a magnetic field directed into the page. Due to the measured change in energy from 63 MeV below the plate to 23 MeV above the plate, the particle's trajectory proved that it had a positive charge and a mass comparable to the electron.

nored, Dirac interpreted these negative energy states as holes in a sea of positive states which are filled by negative charges (electrons) according to Pauli's exclusion principle [Dirac, 1930]. The 'hole' would appear as a new particle with a positive charge, and would annihilate with an electron. Dirac discussed the possibility of the proton as an island in the sea, as it was the only known positively charged particle at the time, but he recognised that its significantly larger mass was problematic. This idea of the proton being the negative energy solution faced opposition from Robert Oppenheimer [Oppenheimer, 1930a,b], who argued that this could not be true due to their mass. Dirac was persuaded by these arguments and proposed the existence of an anti-electron in 1931.

Only two years later in 1933, Carl Anderson discovered a charged particle which had comparable mass to the electron but with opposite charge. No link was initially made between Dirac's theory and this discovery, so the name for this positive electron became the 'positron', represented by the symbol e^+. The first

image of a positron is shown in figure 1.1. The positron is the anti-electron and it is therefore also a fermion. It has an intrinsic spin of 1/2 and following the CPT theorem (charge, parity, and time reversal symmetry), the positron mass is the same as the electron mass, but as an antiparticle it has opposite charge ($+e$ instead of $-e$). A significant feature of positrons is that they are distinguishable from electrons, which is useful in a variety of cases, such as when studying solids. In a solid, electrons are lost in a sea of identical electrons, whereas positron diffusion can be followed until annihilation. The positive charge of a positron also allows the study of processes which are not possible with electrons, such as being trapped at negatively charged lattice defects and impurities, which provides new insights.

In modern experimental research, positrons have many uses due to the creation of low-energy near mono-energetic beams in vacuum [Danielson *et al.*, 2015]. A positron exists for a finite time within a material before annihilating, dependent upon many properties including the structure of the material and the number of voids or defects. Therefore, positron annihilation lifetime spectroscopy (PALS) is a technique used to study solids [Siegel, 1980]. It allows sensitive characterisation and importantly is non-destructive to the material. As a result, in materials science, positrons are used to study lattice defects and the electronic structure of solids such as metals and semiconductors e.g., [Coleman, 2000; Schultz and Lynn, 1988; Tuomisto and Makkonen, 2013]. They are also used as a sensitive probe in atomic and molecular physics e.g., [Charlton and Humberston, 2000; Surko *et al.*, 2005; Gribakin *et al.*, 2010].

The development of new technologies has permitted the control and manipulation of beam properties [Danielson *et al.*, 2015] and positron trapping and accumulation [Murphy and Surko, 1992; Jørgensen *et al.*, 2005] has allowed the study of non-neutral positron plasmas. Positron plasmas are used to produce positronium (Ps) which is an electrically neutral exotic atom, consisting of the quasi-stable bound state of an electron and a positron. Ps exists in only two spin states, the S = 0 singlet state and S = 1 triplet state. The singlet state is called para-positronium (p-Ps) and has antiparallel electron and positron spin, whilst the triplet state is called ortho-positronium (o-Ps) and has parallel spins. Ps production has applications in fundamental and applied studies [Rich, 1981; Jean *et al.*, 2003], and it can be laser excited into Rydberg states, where spectroscopy allows its structure to be probed [Cassidy, 2018]. Contemporary Ps spectroscopy is achieved by single-shot positron annihilation spectroscopy (SSPALS) [Cassidy

et al., 2006b; Deller, 2019], which uses an intense pulse of positrons, in contrast to the individual positrons used in PALS. The technique is useful for studying Ps, but it is foreseeable that it will improve the characterisation of solids [Cassidy *et al.*, 2006b].

Experiments which study the simplest anti-atom, antihydrogen ($\overline{\mathrm{H}}$), require an intense positron source [Ahmadi *et al.*, 2017; Aghion *et al.*, 2015; Imao *et al.*, 2010; Fitzakerley *et al.*, 2016]. Antihydrogen is formed from an antiproton ($\overline{\mathrm{p}}$) and a positron, and as the AD (Antiproton Decelerator) at CERN is currently the only place that can produce slow antiprotons, this is the only place low energy antihydrogen can be produced and trapped, e.g. by ATHENA [Amoretti *et al.*, 2002], ATRAP [Gabrielse *et al.*, 2002], ALPHA [Andresen *et al.*, 2010], and ASACUSA [Enomoto *et al.*, 2010]. Historically, most laboratory antimatter experiments have been conducted with positrons, as they are easier to obtain than antiprotons and other antiparticles.

1.2 Positron Sources

There exist three main ways of obtaining positrons in a laboratory environment, using: radioactive sources, accelerators, and lasers. Generally, devices utilising pair production of positrons using nuclear reactors [van Veen *et al.*, 1999; Hugenschmidt *et al.*, 2008; Hawari *et al.*, 2011; Sato *et al.*, 2015] or large accelerator facilities [Kurihara *et al.*, 2000; Wagner *et al.*, 2018] generate the largest positron flux but they involve technical challenges and great expense, thus radioactive sources are often favoured in a laboratory environment.

Accelerators or nuclear reactors may be used to generate radioactive positron sources. The radioactive positron source used for most beamline systems is sodium-22, which is a man-made isotope and has a half-life of 2.6 years. This half-life is desirable as the specific activity is sufficiently high for experimentation, while not needing to be replaced often due to fast decay. Sodium-22 emits a positron and an electron neutrino (ν_e) by β^+ decay, due to the weak force, which has a branching ratio of $\sim 90\%$*, turning into an excited nuclear state of neon-22,

$$^{22}\mathrm{Na} \rightarrow \ ^{22}\mathrm{Ne}^* + e^+ + \nu_e. \tag{1.1}$$

*The other 10% of the decay's branching ratio is accounted for by electron capture, in which a bound inner electron is absorbed by a proton, changing to a neutron and ν_e.

This excited state has a lifetime of 3.7 ps, before emitting a gamma ray of 1275 keV as it decays into the ground state

$$^{22}\mathrm{Ne}^{*} \rightarrow \ ^{22}\mathrm{Ne} + \gamma_{(1275\ \mathrm{keV})}. \tag{1.2}$$

The emitted positron annihilates with an electron to predominantly produce two 511 keV gamma rays, which are back-to-back in the centre-of-mass rest frame due to the pair annihilation

$$e^{+} + e^{-} \rightarrow \ 2\gamma_{(511\ \mathrm{keV})}. \tag{1.3}$$

The Swansea University positron beamline uses a sealed sodium-22 β^{+} emitter from iThemba LABS. A new radioactive source was installed on the system in December 2018, with an activity of 1.85 GBq (50 mCi).

Some other experiments choose particle accelerators, which use radio frequency (RF) fields to accelerate electrons beyond the threshold energy to collide with a target and produce positrons via pair production [Coleman, 2000]. The threshold energy in this case is equal to the rest mass energies of a positron and an electron, 2×511 keV $= 1.022$ MeV. Bremsstrahlung gamma rays with an energy greater than the threshold energy are produced as the electron decelerates during the collision, and the photon energy is converted to mass following Einstein's mass-energy equivalence, $E = mc^2$. Increasingly, linear accelerators are chosen for this purpose as they are more compact than circular accelerators, e.g., in the GBAR experiment [Niang *et al.*, 2020].

The third method, which is newest, uses lasers to provide positrons. By pulsing a laser at a thin solid [Chen *et al.*, 2009] or through a gas which is ionised by the strong electric field [Sarri *et al.*, 2013], a plasma of electrons can be generated. These electrons may then be accelerated and collided with a target to produce positrons, in the same way as with an accelerator.

In addition, positrons are formed by pair production without human intervention, such as due to the strong gravitational fields from black holes and neutron stars [Wardle *et al.*, 1998], which are observed in cosmic rays that travel through the universe. Extraterrestrial cosmic rays can also cause air showers in the Earth's atmosphere [Grieder, 2010]. As a primary cosmic ray collides with the nucleus of an atom in the air, the production and subsequent decay of energetic hadrons causes a cascade of ionised particles, known as an air shower, where some of these secondary particles are positrons. The strong electric fields during lightning storms

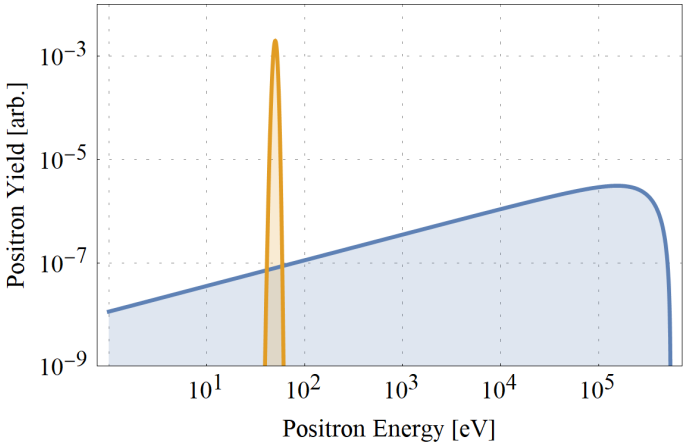

Figure 1.2: Comparison of the typical energy spectrum of β^+ particles from a radioactive sodium-22 source (blue) with the narrow energy distribution of moderated positrons by a typical neon moderator (orange). Moderation results in an increased positron yield at low energy and a narrower energy distribution.

also produce positrons [Briggs *et al.*, 2011], but they too are highly energetic and currently untrappable for experimentation.

1.3 Moderation

The β^+ particles ejected from a radioactive source have a range of kinetic energies that is too broad for effective trapping and accumulation. For ^{22}Na the energy range is 0 – 545.5 keV, which is a problem, as for solid-state and atomic physics experiments with positron beams, the positrons must be slowed to eV energies or less and desirably have a narrow energy distribution. To increase the number of low energy positrons, moderation is required, which decreases both the mean energy and its spread, as shown in figure 1.2. During moderation, positrons are implanted into a solid and lose energy until they are near thermal equilibrium with the crystal lattice [Schultz and Lynn, 1988], which takes $\sim$ 1 ps [Coleman, 2000]. A diagram showing the interactions between positrons and a material is shown in figure 1.3.

Two main types of positron moderator exist. The first is a solid foil or mesh, typically made of annealed tungsten, which as a conductor, causes the positrons to lose energy primarily through ionisation, thereby causing a relatively short diffusion length. Due to the dipole caused by the free electron cloud at the surface

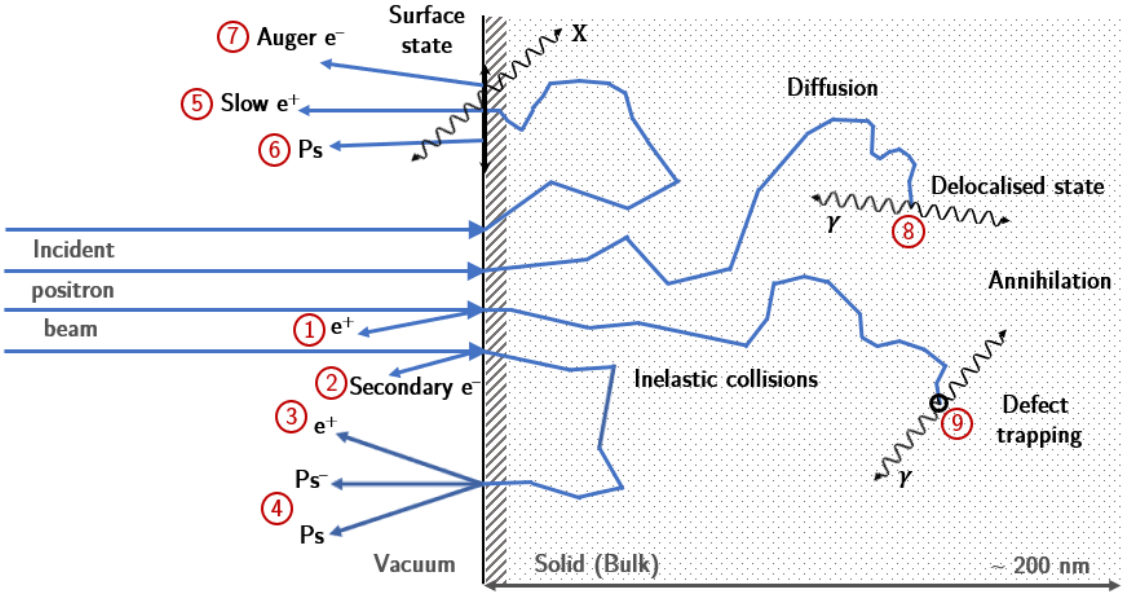

Figure 1.3: Positron interaction with a material: at the surface positrons can be (1) reflected and diffracted, or (2) cause the emission of secondary electrons. Nonthermal positrons can be emitted from the solid (3) epithermally or (4) as positronium. After thermalisation and back diffusion to the surface, positrons may be emitted (5) as moderated positrons (for materials with a negative positron work function) with a well-defined energy characteristic of the material or (6) as thermal positronium. Annihilation from a surface state can cause (7) the emission of Auger electrons and characteristic X-rays. In the bulk, positrons either annihilate (8) from a delocalised state in the lattice, or (9) when trapped in a defect.

of the metal, the resultant work function is negative for positrons, which means it is favourable to emit them and they gain energy when leaving the metal. Positrons must have reached thermal energy within a diffusion length of the surface, which is $\sim$ 100 nm [Charlton and Humberston, 2000], for a chance to be emitted. This results in an energy distribution full width at half maximum of $\sim$ 0.3 eV [Canter and Mills Jr., 1982], but is around 0.1% efficient[†] [Vehanen *et al.*, 1983]. At the surface, annihilation and positronium formation limit the moderator efficiency, so high temperature annealing of the metal prior to its use removes vacancies and voids, and cleans most contamination from the surface [Liszkay *et al.*, 2002] to reduce these undesirable effects.

The first successful positron moderator was demonstrated in 1958 by W. H. Cherry

[†]Moderator efficiency is defined as the ratio of the number of emitted low energy positrons to the number of incident β^+.

as a PhD student [Cherry, 1958]. β^+ bombardment resulted in positrons being transmitted through a thin layer of chromium coated mica held in vacuum, resulting in an increase of particles with an energy < 10 eV. This pioneering positron moderator was never published in a journal and only had an efficiency of 10^{-8}.

The second type of positron moderator, which is the one implemented in this system, uses a rare gas solid (RGS) e.g., neon, which causes the positrons to lose energy via ionisation, excitation and phonon scattering until they become epithermal, i.e. with an energy slightly greater than the thermal energy. As the positron mass is much smaller than the mass of an RGS atom, each phonon scattering event causes a small energy loss. Once the positron energy is smaller than the RGS band gap energy, phonon scattering is the only process that can occur. Therefore, positrons diffuse through the moderator and as a RGS has a positive work function, the positrons must be sufficiently energetic to overcome the potential barrier to be emitted. This results in an energy distribution width of several eV coming out, as in figure 1.2. Good RGS moderators are only $\sim 1\%$ efficient [Mills and Gullikson, 1986], therefore most of the positrons produced by a radioactive source cannot be utilised. Although RGS moderators have a factor of ~ 10 greater efficiency compared with metal foils, the resultant energy distribution is wider, and they rely on expensive (and sometimes unreliable) technology such as compressors. RGS moderators must also be 'regrown' every few weeks, so many positron research groups instead opt for a tungsten moderator.

1.4 Penning Traps

Earnshaw's theorem states that it is impossible to confine a static charged particle in all three dimensions by using a static electromagnetic field [Earnshaw, 1848; Jackson, 1998]. Paul traps, which are radiofrequency traps, overcome this problem by using a rapidly oscillating electric field. In contrast, a Penning trap uses a static electric field with a magnetic field in the axial direction to provide confinement, and is the type of charged particle trap used in this work.

The Penning trap was first built by Hans Georg Dehmelt. It was named after Frans Michel Penning, as Dehmelt's inspiration was the Penning vacuum gauge, where the current through a discharge tube in a B-field is proportional to pressure. The trap was simply a central ring electrode with two voltage biased endcaps, as shown in figure 1.4, which was able to trap electrons for about 10 s [Dehmelt,

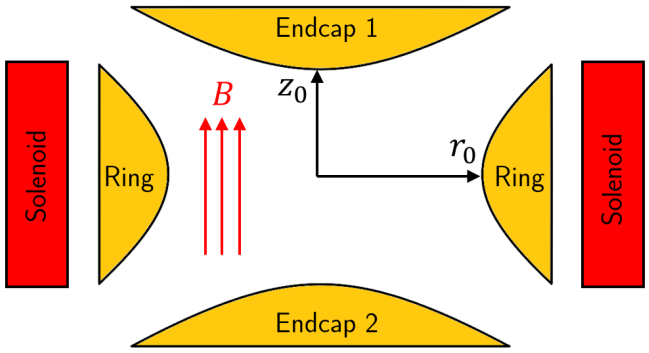

Figure 1.4: Schematic cross-section at the centre of a hyperbolic Penning trap. Both endcaps are connected and a DC potential is applied between them and the ring electrode to trap charged particles along the z–axis. The uniform magnetic field from the solenoid (red) ensures trapping in the x–y plane.

1968, 1969]. The B-field ensured ion confinement in the plane perpendicular to its field, whilst the E-field applied to the electrodes ensured confinement along the B-field. Dehmelt shared the Nobel Prize in Physics in 1989 with Wolfgang Paul, for their development of the ion trap technique [Paul, 1990].

Cylindrical Penning traps, consisting of a series of cylindrical ring electrodes, were introduced to allow access along the trap axis for particle injection, ejection, and manipulation [Gabrielse *et al.*, 1989]. In cylindrical Penning traps the B-field is supplied by a solenoid, whilst the electrostatic fields are produced by an array of cylindrical electrodes inside the vacuum chamber, which replace the endcaps from a conventional Penning trap to provide axial confinement [Malmberg and Driscoll, 1980]. Cylindrical Penning traps are the type of charged particle trap used in this work.

Cylindrical coordinates are typically used to describe Penning traps as they suit the symmetry of the fields. The z-axis is the axial axis parallel to the B-field, where $z = 0$ is at the centre of the ring electrodes. The plane perpendicular to the z-axis is the radial plane described by the radius, r, and the angular position, θ.

1.5 Thesis Outline

This thesis details the implementation of a harmonic potential well with an innovative double rotating wall electric field, as opposed to a conventional single rotating wall, which provides closer agreement with the model for the rotating wall compression mechanism in the single particle regime [Isaac *et al.*, 2011; Isaac,

2013]. Developments towards realising the resistive cooling of low-energy positron clouds are also reported.

This first chapter provided a brief overview of the history of positron physics and introduced the type of charged particle trap that will be discussed in the rest of this text. In the second chapter, the Swansea University positron beamline used for these studies is described, and practical details of the methodology are specified. Chapter three presents implementing a harmonic potential well and characterising a positron cloud, with a temperature measurement method for the single particle regime. Rotating wall electric fields are the subject of chapter four, with the novel implementation of a double rotating wall using a custom-built function generator. In chapter five, work towards resistive cooling of positrons clouds for the first time using a coupled electronic circuit is disclosed, whilst the last chapter closes with a summary and an outlook at future work.

Chapter 2

The Swansea University Positron Beamline

In this chapter, relevant details about the Swansea positron beamline will be outlined. The beamline aims to improve techniques for the moderation, trapping, accumulation and manipulation of low energy positrons, primarily for the excitation of positronium to Rydberg states [Baker *et al.*, 2018], but also in the interests of fundamental research.

The vacuum system of the beamline comprises of a series of five six-way DN160 conflat stainless steel crosses (X-1, X-2. . . X-5) connected by vacuum tubing, shown in figure 2.1. Further details about the Swansea beamline and its operation can be found in [Clarke *et al.*, 2006; Isaac, 2010; Deller, 2013].

2.1 Vacuum System

The system is kept at ultra-high vacuum in order to minimise positron scattering and annihilation against background gas, and thereby maximise the positron lifetime. Three types of vacuum pumps are used on this system, shown in figure 2.2, namely: scroll, turbomolecular, and cryogenic pumps. Turbo pumps produce medium to high vacuum of $P \sim 10^{-3}$–10^{-8} mbar but to avoid them stalling, a lower grade vacuum is required as backing. For this task, scroll pumps are chosen as they are mechanical, produce a low vacuum, and are generally quieter and more reliable than other types of pumps. The third type of pump used on the beamline is the cryopump, which can produce ultra-high vacuum of below $P \sim 10^{-9}$ mbar. Cryopumps trap gases by condensing them onto a cold surface which is cooled by

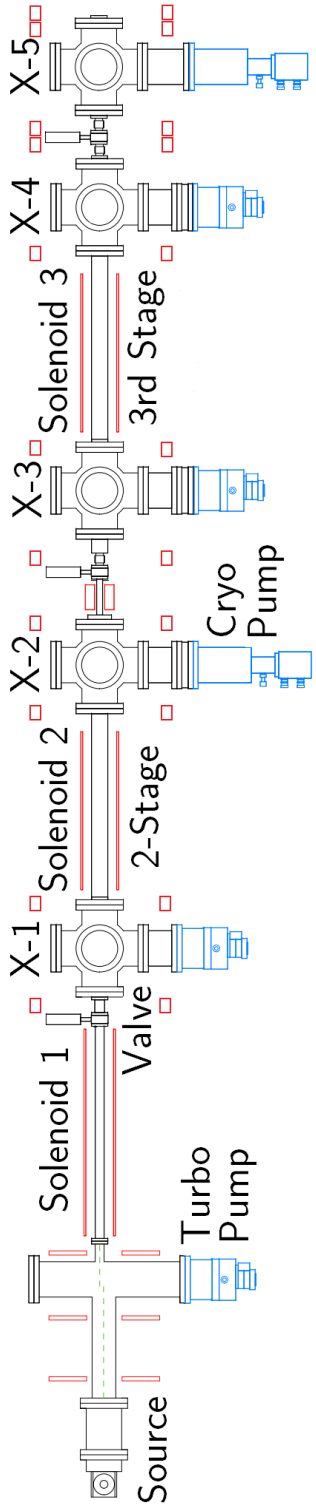

Figure 2.1: Schematic of Swansea University's positron beamline (side-on) showing the vacuum system (black) with the pumping crosses (X-1, X-2, ..., X-5), high-vacuum pumps (blue) and magnetic coils (red), modified from [Mortensen, 2013]. The total length of the beamline is approximately 7 m.

compressed helium. Eventually, the cold surface saturates and the pump speed tends to zero, as more gas cannot condense, but the trapped gas is held until regeneration has been performed. Regeneration is the process of warming to room temperature, which allows the trapped molecules to be pumped out and ejected from the system.

To measure the pressure in the vacuum system, various pressure gauges are used. The three types of pressure gauges used here are the Pirani, capacitance, and Penning cold cathode. A Pirani gauge measures the thermal conductivity through a wire to infer the pressure. Capacitance gauges rely on a mechanical deformation due to the pressure which changes the capacitance to infer the pressure for high vacuum, while Penning cold cathode gauges infer pressure by measuring the ionisablility of the surrounding gas. Penning gauges are gas dependent, therefore it is important to ensure that a conversion factor is taken into account when using different gases. So-called 'full range' gauges also exist in the system, but they are in fact multiple gauges displaying a single value, with a second gauge taking over once the pressure departs from the range of the first gauge. These gauges are located on the beamline as shown in figure 2.2.

2.2 Gas System

Three types of gas are used on the system, a moderator gas (Ne), buffer gas (N_2), and cooling gas (CF_4). The type of cooling gas was chosen due to its efficient positron cooling [Greaves and Surko, 2001], which is further detailed in chapter 4. Each of these are admitted into the system from a regulated gas bottle by a piezoelectric valve (PEV) that controls the flow. A proportional-integral-derivative (PID) controller then monitors the inlet pressure and opens or closes the valve as appropriate, to ensure that the system pressure remains stable. As the pump rate out of the system is constant, the pressure in the system reaches an equilibrium. Capacitance gauges measure the pressure of the buffer and cooling gases immediately after the PEVs before entering the system, whilst the moderator gas pressure is measured from the source chamber as only one gas is admitted there.

Nitrogen buffer gas flows in midway along the first stage of the 2-stage trap, as shown in figure 2.4, and the physical dimensions of the electrodes form a pressure gradient along its length. A narrow pumping restriction between the source

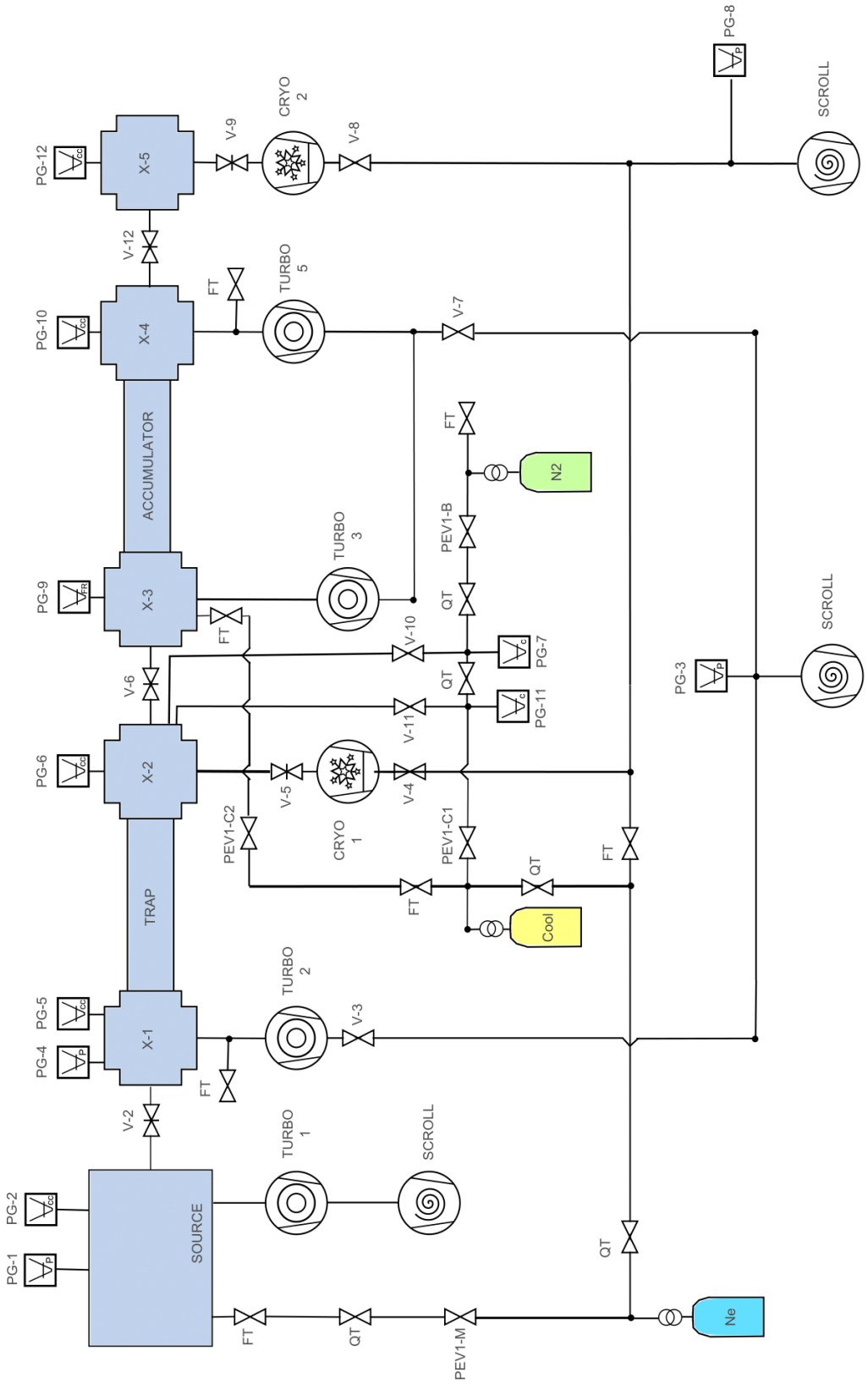

Figure 2.2: Pumping diagram schematic for the Swansea University positron beamline. Key: PEV, piezo-electric valve; PG, pressure gauge; C, capacitance gauge; CC, cold cathode gauge; P, Pirani gauge; FT, full turn valve; QT, quarter turn valve. Modified from [Mortensen, 2013]

chamber and X-1 reduces the amount of nitrogen from the trap that condenses onto the source. The cooling gas enters X-2 directly, and so sufficient cooling gas from the 2-stage also drifts along the next pumping restriction to the 3rd stage accumulator, such that no gas need be directly admitted here.

2.3 Growing a Moderator

The radioactive source of the Swansea positron beamline is attached to a cone which is mounted directly onto a Sumitomo RDK408 cold-head, at around 7 K during operation, so that a thin layer of 99.999% pure neon gas can condense to grow an RGS moderator for β^+ moderation. The first solid neon moderator was implemented by Mills and Gullikson in 1986 [Mills and Gullikson, 1986], where the moderated positron energies were around 0.6 eV, with an efficiency of 10^{-2}. A typical low energy e^+ beam efficiency from the Swansea beamline is $\sim 0.5\%$ of the source activity. As studies have shown that a conical source geometry provides the maximum positron output [Lynn *et al.*, 1989], it is the geometry employed here. The source capsule holder is mounted on an elkonite rod which is in thermal contact with the cold finger by use of a thin sapphire disc. This disc is also important as it provides electrical isolation for the source and the moderator, which means a bias voltage can be applied to the source to increase the yield and control the kinetic energy of the emitted positrons. Resultantly this produces a tuneable low energy positron beam, which also allows a wider tuning range for the trapping potentials than would otherwise be possible, and is utilised in section 3.3.

To grow an RGS positron moderator on the Swansea beamline, neon is admitted using a piezoelectric valve into the source chamber until the pressure is raised to 5×10^{-3} mbar. A feedback control circuit (as detailed in section 2.2) then keeps the pressure stable for around 20 minutes, whilst a layer of solid neon is grown onto the source cone. A typical moderator growth curve is shown in figure 2.3. To determine when the growth is complete, the annihilation count at a closed gate valve before X-2 is monitored until a plateau is seen, which indicates the moderated positron count has reached its maximum. Neon gas in the chamber causes positron scattering and annihilation, probably via Ps formation, so once the neon supply is closed and pumped out of the chamber, the detected slow positron count rate quickly increases to around 2×10^6 e^+/s.

Biasing the source with + 50 V accelerates the positrons towards a free-field

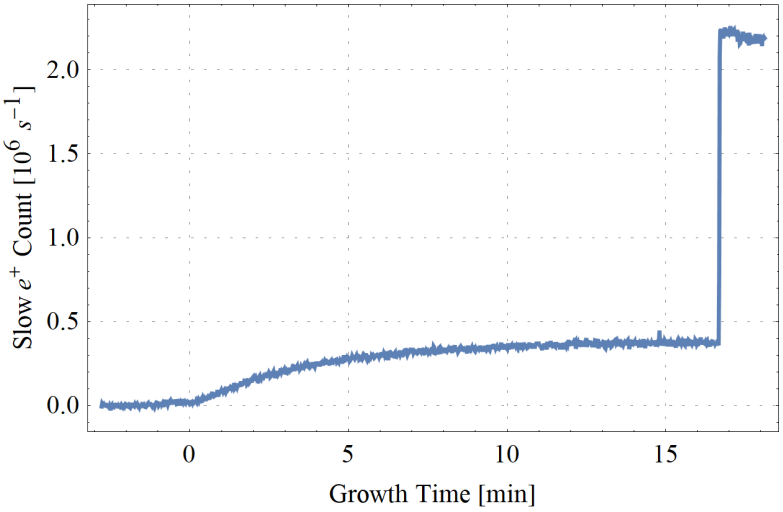

Figure 2.3: An example neon moderator growth curve. Neon gas was admitted into the source chamber and the pressure was kept at 5×10^{-3} mbar, until a plateau in the positron count was seen. The supply of gas was closed after $\sim$ 17 minutes and pumped out of the chamber, causing a sudden increase in detected number due to a decrease in positron loss. The count rate at this time is $\sim 2.2 \times 10^6$ e^+/s but this decreases by $\sim$ 10% over the first few hours as the moderator stabilises.

region before solenoid 1, shown in figure 2.1. An energy selection is performed as particles travel axially along the beamline, by the magnetic field of a 'pancake coil' (described in section 2.5.3) which steers positrons with lower kinetic energies past a step in the beamline, through solenoid 1, and into the buffer gas trap [Murphy and Surko, 1992] which is surrounded by solenoid 2. The buffer gas trap is a 2-stage trap, as shown in figure 2.4. Positrons with large kinetic energies cannot be guided past the step, and instead annihilate with the vacuum chamber. This bend in the path means that the source is not within direct line of sight with the rest of the beamline, such that the high energy beam does not form a part of the main positron beam.

Due to the random nature of radioactive decay, direct current (DC) source-based positron beams have sufficient intensity for some surface studies [Schultz and Lynn, 1988] but is too low for many other experiments. A pulsed slow positron beamline is a prerequisite for contemporary spectroscopic measurements of positronium. Therefore, by trapping and accumulating, spatial and temporal bunching methods allow intense pulses of positrons to be achieved with temporal widths of less than a nanosecond. This is useful for applications such as increasing

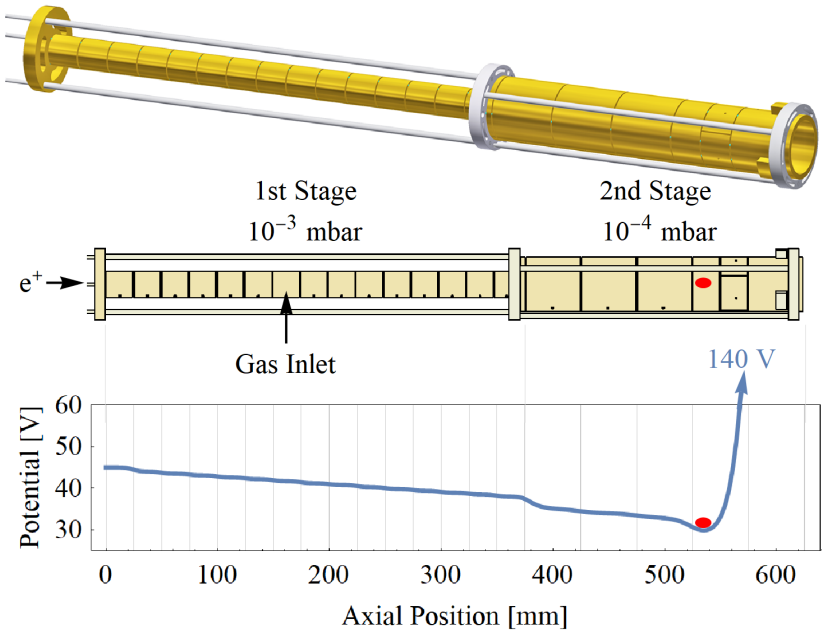

Figure 2.4: (Top) CAD drawing of the 2-stage trap which comprises of the gold cylindrical electrodes in their frame. (Middle) Trap cross-section with the location of the buffer gas inlet and the corresponding pressures in each stage. The location of a typical positron cloud is shown in red. (Bottom) The on-axis total electric potential in the 2-stage trap. The penultimate electrode has been cut in half axially and into quarter segments azimuthally for applying a rotating wall electric field. A cloud of positrons is shown in red at the potential minimum, and the 140 V applied to the final electrode is lowered to eject the positron cloud.

positronium yield, and improving the SSPALS technique [Cassidy *et al.*, 2006b].

2.4 Detection

For detecting positrons there are generally two measurable quantities: their charge, and the gamma rays due to their annihilation.

2.4.1 Charge

For a positron, its charge is given by $e = +1.6 \times 10^{-19}$ C. This can be measured directly by ejecting the positron cloud into a plate acting as a Faraday cup and measuring the charge using the relation $Q = CV$, where Q is the total charge, C is the capacitance, and V is the voltage. When a positron hits a conductive surface, it can cause a secondary electron to be emitted, which is detected as an extra net positive charge. To avoid this miscounting with Faraday cups, they are positively biased at a lower potential than the incoming positrons. This attracts back the emitted electrons, while allowing the incident positrons to strike the Faraday cup. Faraday cups are very accurate for matter particles, as the charge is directly related to the number of ions.

For more sensitive charge measurements, amplification by a single channel electron multiplier (CEM) such as a Channeltron is required. A Channeltron is a continuous dynode vacuum tube structure that multiplies incident charges, as a single electron bombards a secondary emissive material, inducing the emission of one to three electrons [Knoll, 2010]. This process repeats resulting in a large shower of electrons which are all collected by a metal anode, allowing single ions entering the Channeltron to be detected.

Micro-Channel Plate

For spatial resolution, a microchannel plate (MCP) detector is used, which is an array of CEMs. On the Swansea system it is a MCP and phosphor screen assembly from Lambert Instruments, as shown in figure 2.5, which is located on a vertical linear manipulator in X-4. The grid in front of the MCP shields the incident positrons from the high voltage required to bias the front, back and screen. Within the front and back plates are 10 μm diameter channels, which are not parallel with the z-axis to ensure incoming positrons impact the CEM wall.

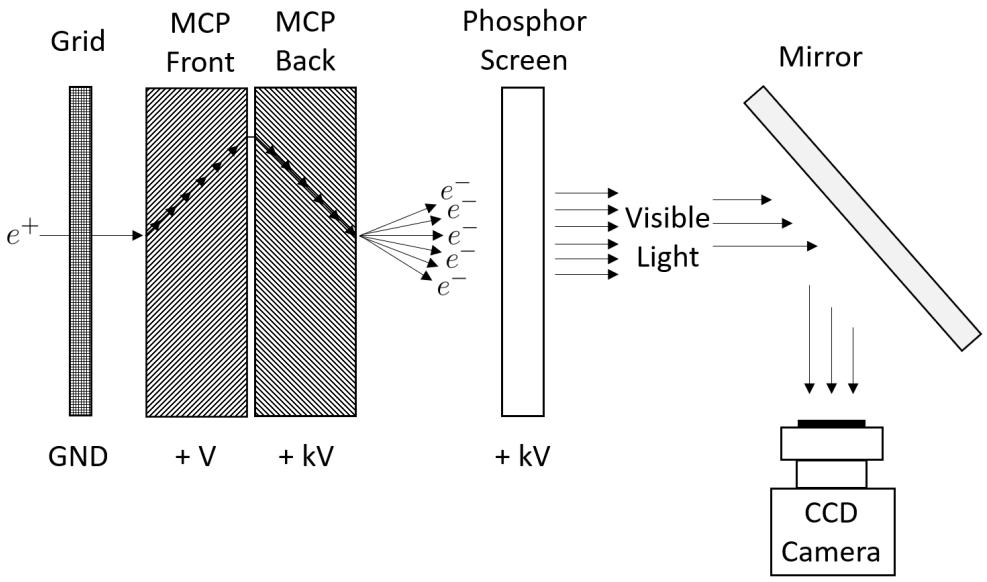

Figure 2.5: Schematic of the MCP set up for positron detection in X-4 (not to scale), showing the MCP plates as an array of single channel electron multipliers. The front and back plates are orientated to create a chevron, to increase number of particle collisions with the channel walls. Typically the biases follow the hierarchy $V_{\text{Screen}} > V_{\text{Back}} \gg V_{\text{Front}}$. The grounded grid in front of the MCP can be biased for parallel energy measurements, while the camera is located outside of the vacuum and images through a viewport.

The channels within the plates are angled with a 180° offset relative to the other plate which forms a chevron, and the centre-to-centre hole spacing is 12 μm. The continuous dynode amplifies on every collision, which can produce a very high gain. Therefore, the MCP can be used as a charge amplifier to perform charge measurements.

The MCP is fixed to a P43 phosphor screen which emits yellow-green visible light upon charged particle implantation. This produces a 2D optical image, which is then reflected by a 45° mirror and captured by a Hamamatsu Orca-R2 1.3 megapixel charge-coupled device (CCD) camera. The size of the CCD images can be scaled knowing the phosphor screen width of 50 mm, and the corresponding number of pixels in the image, giving a pixel width and height of (0.350 ± 0.005) mm.

In section 3.9.1, it is shown that a cloud of trapped charged particles in a Penning trap has a Gaussian distribution in the radial plane. This allows CCD images of the particle cloud to be fitted with a 2D Gaussian in Cartesian coordinates centred at (x_0, y_0), of the form

$$n(x,y) = \frac{N}{2\pi\sigma^2} \exp\left(-\frac{(x-x_0)^2 + (y-y_0)^2}{2\sigma^2}\right) + B, \tag{2.1}$$

where B is the background, and the standard deviation, σ, is related to the peak's full width at half maximum, FWHM $= 2\sigma\sqrt{2\ln(2)}$. This allows the width of the cloud to be quantified. An example fit is shown in figure 2.6. All function fitting in this thesis was performed using the 'NonlinearModelFit' function in Wolfram Mathematica Version 11.1.1.0.

2.4.2 Annihilation

The gamma rays produced by a positron-electron annihilation can be detected by many different types of detector [Knoll, 2010]. A germanium detector is sensitive to single photons and is used to measure their energy, whilst caesium iodide (CsI) and sodium iodide (NaI) are common examples of scintillators that convert gamma rays into visible light or UV, and are the types used in these studies. This light can then either be read out by a photodiode, or a photo-multiplier tube (PMT) optically coupled to a photocathode to produce electrons. A PMT absorbs the light emitted by a scintillator and re-emits it in the form of electrons via the

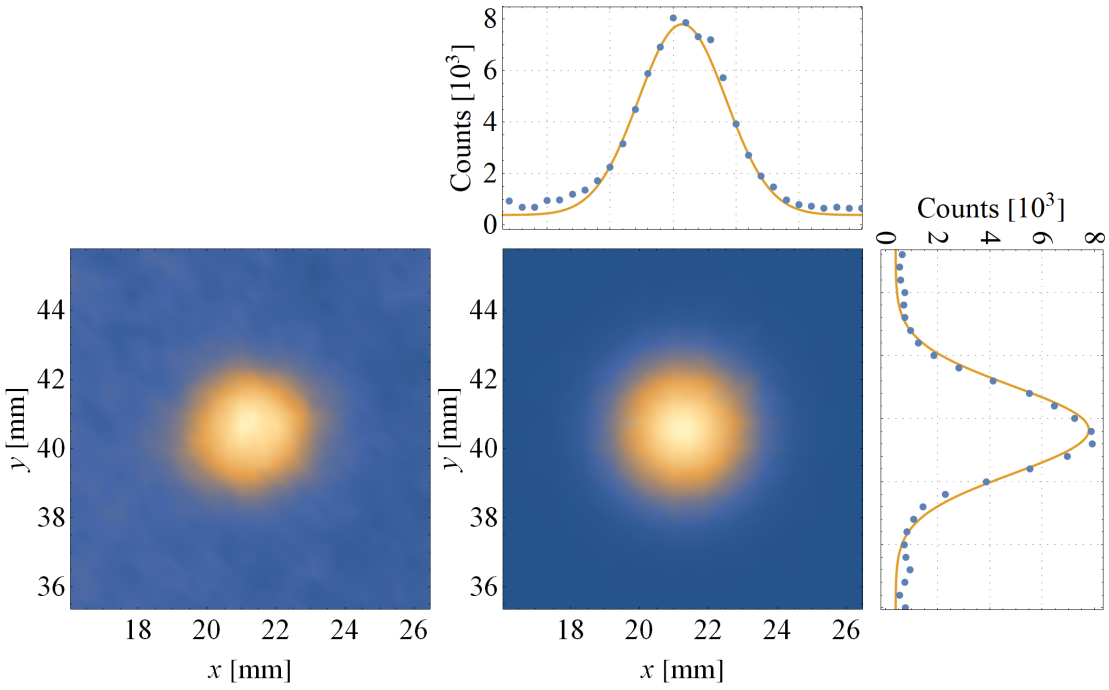

Figure 2.6: An example of the spatial distribution of the positron cloud, (left) a raw CCD image of a positron cloud, and (centre) equation 2.1 fitted to the raw data. The fit gives $\sigma = (1.216 \pm 0.004)$ mm, $N = (68,900 \pm 400)$ counts, and $B = (388 \pm 1)$ counts/mm^2. Cross sections through the fitted centre along x and y are shown above and to the right of the central image respectively, where the raw data are shown in blue and the fit is orange.

photoelectric effect. It has discrete dynodes, in contrast with a CEM. Coupling a PMT to a photocathode can provide sub-nanosecond timing information, which is suitable for these studies.

On this system, typically the annihilation gamma ray flash is registered by a CsI(Tl) crystal coupled to an avalanche photodiode, which is then recorded by a digitiser. The detector decay time of hundreds of nanoseconds is appropriate for this purpose and cross-calibration allows an approximate number of annihilated positrons to be deduced. The uncertainties of the calibration factors will not be included, as these studies are only interested in relative numbers. Common annihilation targets are closed gate valves, the metal plate in X-2, and the MCP in X-4. The digitiser which records each trace is a NI PCI-6713 card which has 12-bit resolution and a maximum sample rate of 1 MS/s per channel. Traces are typically processed offline using Wolfram Mathematica notebooks to determine peak height and perform statistical analyses.

2.5 Magnetic Fields

Radial confinement along the beamline is due to the uniform magnetic field along the axis. Using axial magnetic fields from a series of coils and a 50 mT transport solenoid, the positrons can be guided away from the source region and into the trap. The three types of magnets used on the beamline are steering coils, solenoids and 'pancake coils'. The steering coils are air-cooled, whilst the solenoids and pancake coils are water-cooled by a closed high pressure system at 5 bar.

2.5.1 Steering Coils

There are steering coils in an approximate Helmholtz configuration before and after each six-way pumping cross, to provide an uninterrupted field along the beamline and to adjust alignment. From Ampere's law, the magnetic field strength in the centre of the steering coils is given by

$$B = N\frac{\mu_0 I}{r_{\text{in}} + r_{\text{out}}}, \tag{2.2}$$

where N is the number of loops, I is the current, μ_0 is the vacuum permeability, r_{in} is the inner radius and r_{out} is the outer radius of the coil. They have 400 turns with an inner and outer radius of 258 mm and 300 mm respectively, giving a field

of 0.900 mT A^{-1}. They are usually set at a current of 6.6 A, which results in a field of 5.9 mT.

A second kind of steering coil is the transfer magnet which is located around the narrow pumping restriction between the 2-stage and the 3rd stage. It has 40 turns at an average radius of 35 mm, resulting in 0.718 mT A^{-1}. At a typical current of 100 A it produces a stronger field than the others, of 71.8 mT. As a result, it produces more heat and has a fan to aid its air cooling.

2.5.2 Solenoids

There are three longer solenoids on the system, one surrounds the long pumping restriction between the source chamber and the trap, the second surrounds the 2-stage trap electrodes, whilst an identical third surrounds the 3rd stage accumulator. These solenoids are wound around brass water jackets, with heat resistant tape between each layer, directly onto the vacuum tubes. For an infinite solenoid, the magnetic field due to current flowing through a conductor can be written as

$$B = N_L N \frac{\mu_0 I}{L}, \tag{2.3}$$

where N is the number of turns per layer, I is the current, and N_L is the number of layers of length L. For solenoid 1, $N_L = 4$, $N = 220$ and $L = 890$ mm, giving 1.24 mT A^{-1}. At the typical current of 25 A this results in a 31.0 mT field. Solenoid 2 and 3 are identical and have $N_L = 4$, $N = 170$ and $L = 680$ mm, to give 1.257 mT A^{-1} and a 37.7 mT field at their typical current of 30 A.

2.5.3 Pancake Coils

The three 'pancake coils' are located around the source chamber and differ from the other magnets, as they are short and have a large radius, so are not considered using an average radius. They have a flat profile when viewed from the side, with two narrow tight spirals of wire containing 80 turns each. These are water cooled by a copper pipe around the outside of the coil, with both parts fixed to a metal plate. Treating the spiral as a set of concentric loops simplifies the geometry, and from Ampere's law, the magnitude of the magnetic field at the centre is then

$$B = \frac{\mu_0 I}{2 r_L}, \tag{2.4}$$

where r_L is the radius of a single loop. The approximate total field is then a summation of all the loops

$$B = \mu_0 I \sum_{n=0}^{N} \frac{1}{2\,(r_0 + n\ \delta r)}, \tag{2.5}$$

where δr is the thickness of the wire, r_0 is the smallest loop radius and N is the number of layers in the stack. The values of $r_0 = 76$ mm, $\delta r = 2$ mm and $N = 80$ give 0.722 mT A^{-1}, therefore at the typical current of 15 A this gives a field strength of 10.8 mT. The third coil furthest downstream is the one slightly tilted to guide the positrons over the vertical step in the beamline for energy selection, as described previously.

2.6 Electric Fields

For axial confinement, voltages are applied to cylindrical electrodes to provide electrical trapping potentials. The DC trapping biases are set using the National Instruments (NI) graphical programming package LabVIEW™, which controls two NI-6713 PCI analog output devices capable of eight outputs each of ± 0–10 V, with a timing resolution of up to 1 MS/s. This sends the desired voltage divided by 14 to in-house custom-built 'Llachar' amplifiers, which have ×14 gain and are based upon a PA441 operational amplifier. These have typical 90–10% fall times of $\sim 10\ \mu s$ with an RMS noise of 10 mV. The amplifiers are connected to the trap electrodes which can then be biased with ± 0–140 V to trap charged particles.

2.7 The 2-Stage Trap

The 2-stage trap is a variety of the Penning-Malmberg trap, where the axial confinement is provided by the electrical potential formed when voltages are applied to a series of cylindrical electrodes, and the radial confinement is due to the presence of a uniform axial magnetic field. A 2-stage positron trap was developed [Clarke *et al.*, 2006; Cassidy *et al.*, 2006a; Sullivan *et al.*, 2008], which consists of two pressure stages instead of the previously standard three, and at Swansea University is capable of operating at 10 Hz. For trapping, nitrogen (N_2) buffer gas is let into the trap through a 2 mm diameter hole at the middle of the first stage (shown in figure 2.4), which is pumped at the source end by a 400 L/s turbo

pump and at the other end by an 800 L/s cryogenic storage pump (as shown in figure 2.2).

During inelastic collisions between positrons and nitrogen molecules, three processes compete [Murphy and Surko, 1992], alongside negligible direct annihilation which can still occur. Positrons with an energy < 8.8 eV are unable to lose sufficient energy by rotational and vibrational excitation of a nitrogen molecule during a collision, and so cannot be trapped. For energies > 8.8 eV, electronic excitation of a nitrogen molecule results in positron energy loss and therefore trapping. Due to the Ps formation threshold of 8.8 eV [Marler and Surko, 2005], it was found that for kinetic energies > 11 eV, the number of positrons lost to Ps formation is equal to those trapped due to electronic excitation. This results in a energy window of ~ 3 eV for efficient positron trapping with nitrogen buffer gas. Alternatively, trapping positrons using molecular vibrational transitions is also possible for a number of gases, but with a significantly lower efficiency than by electronic excitation [Baker *et al.*, 2020].

Incoming positrons to the 2-stage travel back and forth along the trap axis and lose ~ 8.8 eV each during a collision [Murphy and Surko, 1992], mainly due to electronic excitation of the nitrogen molecule. This means that after one collision, they will be unable to escape past the potential barrier at the entrance and after a few further collisions eventually collect in the potential well minimum at an axial position of ≈ 540 mm along the 2-stage, as was shown in figure 2.4. When the barrier voltage at an axial position of 600 mm is lowered from ~ 140 V to ground, the positron cloud is ejected and annihilates downstream causing a sharp burst of gamma rays which can be detected. This gamma ray signal can be used to obtain information about the number of positrons that were held in the trap, their lifetime, and the time width of the ejected pulse. Accumulating for 1 s at 1 Hz operation means that usually $\sim 10^5$ positrons are trapped, dependent upon the number of positrons in the DC beam and the gas pressure.

2.8 The 3rd Stage Accumulator

Once the particles are ejected from the 2-stage trap by lowering the exit electric potential barrier, they are magnetically guided downstream through a pumping restriction which is 38 mm in diameter and 320 mm long, where the larger magnetic field of ~ 72 mT minimises losses into the third trapping stage, which is surrounded

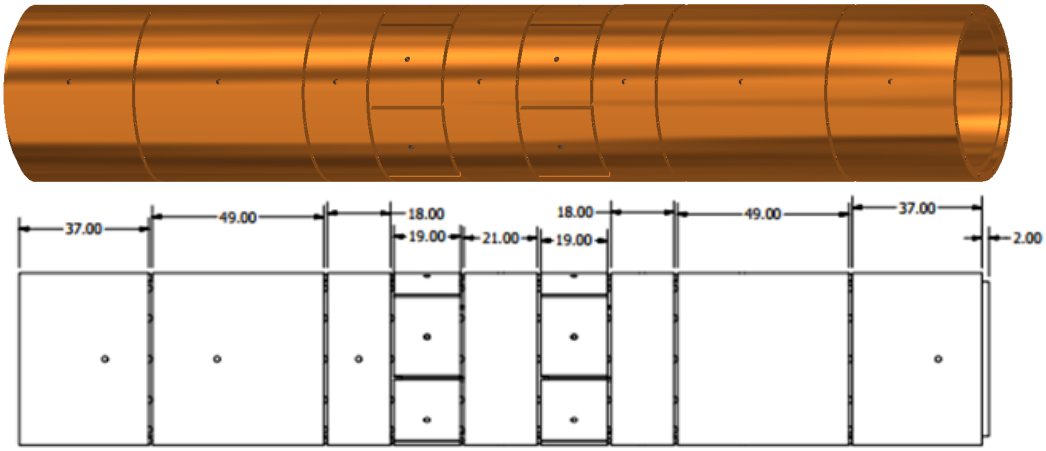

Figure 2.7: Drawing of the cylindrical gold plated aluminium electrodes in the 3rd stage (side-view), where measurements are given in millimetres. The sapphire spheres between each electrode for electrical isolation are shown, along with some of the threaded holes for the electrical connections. The internal diameter is 41 mm.

by solenoid 3.

The 3rd stage accumulator was installed to greatly increase the number of trapped charged particles by stacking multiple clouds from the 2-stage and to allow new rotating wall studies. For details of the installation of the 3rd stage, see [Evans, 2014]. The lower pressure in the 3rd stage allows an increase in trapped charged particle number for increased positronium formation per shot, and enables the study of particle clouds or non-neutral plasmas.

The cylindrical electrode stack confines the particles axially, with each of their lengths optimised for trapping potential harmonicity, and these are shown in figure 2.7. This harmonicity facilitates the study of novel rotating wall techniques as described in chapter 4. During typical operation, the pressure in X-2 (at the downstream end of the 2-stage trap) is $\sim 10^{-5}$ mbar and so in the molecular regime some cooling gas flows across into the 3rd stage, resulting in pressures of $\approx 7.0 \times 10^{-7}$ mbar in X-3 and $\approx 0.4 \times 10^{-7}$ mbar in X-4 (at the upstream and downstream ends of the 3rd stage accumulator, respectively). Prior to the studies described herein, the 3rd stage electrodes were primarily used for bunching positron clouds [Edwards, 2019], although this was not their designed purpose.

After ejection from the 3rd stage, if the MCP is raised, then particles can be passed through another valved pumping restriction (38 mm in diameter and

220 mm length) into the positronium production region. This region is a six-way DN160 vacuum cross for laser access, containing a silica sample mounted on a target, details of which are found in e.g. [Deller *et al.*, 2015; Baker *et al.*, 2018].

2.9 Trapped Charged Particle Motion

Penning traps use an electrostatic field and a uniform magnetic field to confine charged particles in all three spatial dimensions. The simplest quadrupole potential in Cartesian coordinates has the form $\phi \propto ax^2 + by^2 + cz^2$, where a, b, and c are constants. To satisfy the Laplace equation,

$$\nabla^2\phi = 0, \tag{2.6}$$

then requires that $a+b+c=0$, and so for a 3D quadrupole, $a=-1$, $b=-1$, and $c=2$ is the solution of interest. The ideal quadrupole electric field in a Penning trap therefore produces the potential

$$\phi(x,y,z) = \frac{U_0}{2d^2}\left(-\frac{1}{2}x^2 - \frac{1}{2}y^2 + z^2\right), \tag{2.7}$$

where U_0 is the endcap electrode voltage and d is a length parameter related to the trap geometry [Brown and Gabrielse, 1986], which traps the charged particles in a harmonic potential well along the z-axis. In an electromagnetic field, the motion of a charged particle with mass m and charge q is described by the Lorentz equation

$$m\ddot{\mathbf{x}} = q(\mathbf{E} + \dot{\mathbf{x}} \times \mathbf{B}), \tag{2.8}$$

where $\mathbf{E}$ and $\mathbf{B}$ are the electric and magnetic field respectively, at a point $\mathbf{x}$ in space. Substituting for the uniform magnetic field $\mathbf{B} = B\hat{z}$, which provides the radial confinement to allow 3D trapping, and the electric field $\mathbf{E} = -\nabla\phi$, where ϕ is from equation 2.7, gives

$$\ddot{x} = \frac{\omega_z^2}{2}x + \Omega_c\dot{y}, \tag{2.9a}$$

$$\ddot{y} = \frac{\omega_z^2}{2}y - \Omega_c\dot{x}, \tag{2.9b}$$

and

$$\ddot{z} = -\omega_z^2 z, \tag{2.9c}$$

where the free cyclotron frequency and axial bounce frequency are given by

$$\Omega_c = \frac{qB}{m} \tag{2.10a}$$

and

$$\omega_z = \sqrt{\frac{qU_0}{md^2}} \tag{2.10b}$$

respectively. Thus, the axial motion is simple harmonic with an angular frequency ω_z, decoupled from the transverse motion in the x–y plane. Introducing the complex variable $u(t) = x(t) + iy(t)$, equations 2.9a and 2.9b can be combined giving

$$\ddot{u} = \frac{\omega_z^2}{2} u - i\Omega_c \dot{u}, \tag{2.11}$$

describing the motion in the x–y plane. Solving using the ansatz $u(t) = u\,(0)\, e^{-i\omega t}$ gives the characteristic equation

$$\omega^2 - \Omega_c \omega + \frac{\omega_z^2}{2} = 0, \tag{2.12}$$

which has roots of

$$\omega_\pm = \frac{1}{2}\left(\Omega_c \pm \sqrt{\Omega_c^2 - 2\omega_z^2}\right). \tag{2.13}$$

The modified cyclotron frequency is the positive root, $\omega_+ \equiv \omega_c$, whilst the negative root is the magnetron frequency, $\omega_- \equiv \omega_m$. These roots show that $\Omega_c > \sqrt{2}\omega_z$ is a requirement for confinement in the trap.

So the solutions to the equations of motion 2.9a and 2.9b are

$$x = |A_+| \sin\left(\omega_c t + \phi_+\right) + |A_-| \sin\left(\omega_m t + \phi_-\right) \tag{2.14}$$

and

$$y = |A_+| \cos\left(\omega_c t + \phi_+\right) + |A_-| \cos\left(\omega_m t + \phi_-\right), \tag{2.15}$$

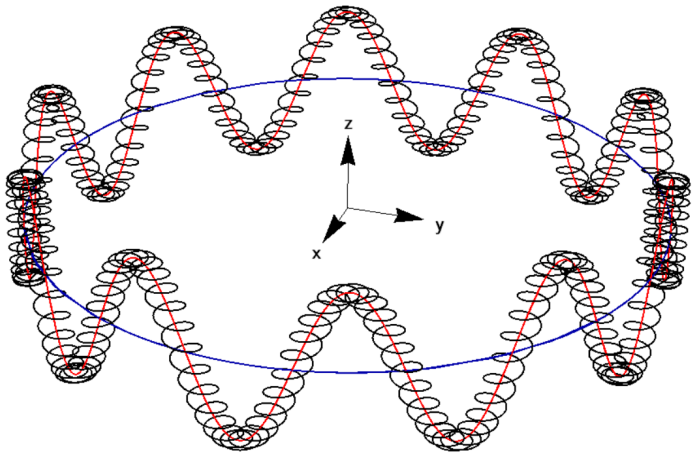

Figure 2.8: Motion of a charged particle in a Penning trap (black), magnetron motion (blue) and the 'guiding centre' combination of the axial bounce and magnetron motion (red). The total motion is obtained by addition of the guiding centre and the cyclotron motion.

whilst the trivial solution to equation 2.9c is

$$z = |A_z| \sin(\omega_z t + \phi_z). \tag{2.16}$$

$A_{\pm,z}$ and $\phi_{\pm,z}$ are the constants of integration, which depend upon the initial position and velocity of the charged particle.

Now the three frequencies that describe the motion of the charged particle are known: ω_z is the axial bounce frequency due to the electric field, ω_c is the modified cyclotron frequency due to the magnetic field, and ω_m is the magnetron frequency which is due to the crossed electric and magnetic fields in the trap. In the x–y plane the particle follows an epitrochoid (a particular form of roulette), which is the superposition of a fast (ω_c) circular motion on a slow (ω_m) circular motion, as shown in figure 2.8.

As the hierarchy $\omega_z \ll \Omega_c$ exists, then for the positive root in equation 2.13, the $2\omega_z^2$ term is negligible and so

$$\omega_c \approx \Omega_c, \tag{2.17}$$

while for the negative root, Taylor expansion gives

$$\omega_m = \frac{1}{2}\left(\Omega_c - \Omega_c\left(1 - \frac{\omega_z^2}{\Omega_c^2} + \dots\right)\right) \approx \frac{\omega_z^2}{2\Omega_c}. \tag{2.18}$$

Useful exact relationships between the defined frequencies can be derived as follows. Using equation 2.13 and summing the two roots gives

$$\omega_c + \omega_m = \Omega_c, \tag{2.19}$$

while their multiplication shows that

$$\omega_c \omega_m = \frac{\omega_z^2}{2}. \tag{2.20}$$

The 'invariance theorem' [Brown and Gabrielse, 1982] of the three observables

$$\omega_c^2 + \omega_z^2 + \omega_m^2 = \Omega_c^2. \tag{2.21}$$

is significant as it means that in physical traps, first-order frequency shifts due to trap nonidealities, such as machining imperfections, cancel.

2.10 Particle Trapping Model

To characterise the number of accumulated particles in a trap, a simple model with only a few variables can be used. The rate equation for trapping N particles in a trap, at a particle trapping rate R from a DC beam, is given by

$$\frac{dN}{dt} = R - \lambda N, \tag{2.22}$$

where λ is the loss rate due to scattering on gas, imperfections in the electric and magnetic trapping fields, and annihilation if they are antimatter particles. Equation 2.22 is a separable ordinary differential equation, and solving this for N by integration and assuming that no particles are initially trapped, $N(0) = 0$, gives

$$N(t) = \frac{R}{\lambda}(1 - e^{-\lambda t}), \tag{2.23}$$

for $t > 0$. In practice, the parameters R and λ can be extracted from a fit to trapped particle number as a function of accumulation time, as shown in figure 2.9.

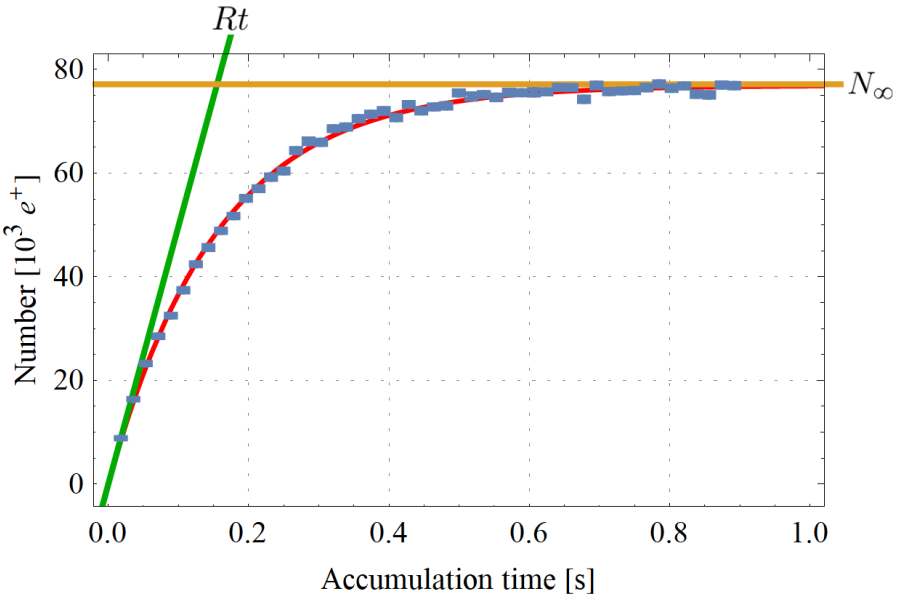

Figure 2.9: An example showing the number of positrons after accumulating in the 2-stage trap with an applied rotating wall. The red line is a fit to equation 2.23 giving $R = (498 \pm 4) \times 10^3$ e^+/s and $\tau = (0.155 \pm 0.001)$ s, which gives $N_\infty = (77.2 \pm 0.8) \times 10^3$ e^+, shown as the orange line. Each point is the mean of four repeats plotted with the standard error, where the CsI detector signal has been converted to positron number using a calibration factor.

The lifetime, $\tau = \lambda^{-1}$, is then the mean time a particle will remain trapped, which is finite due to particle loss. Looking at equation 2.23 considering long times ($t \to \infty$), the number of particles in the trap saturates at

$$N_\infty = \lim_{t\to\infty} N = \frac{R}{\lambda} = R\tau, \tag{2.24}$$

which occurs when the trapping and loss rates of equation 2.22 become equal ($dN/dt \to 0$) and is shown by the orange line in figure 2.9. While looking at short times (where $t \ll \tau$),

$$\lim_{t\ll\tau} N = \frac{R}{\lambda}\left(1 - (1 - \lambda t + \dots)\right) = Rt, \tag{2.25}$$

shown in figure 2.9 by the green line, which would describe the number of trapped particles if the lifetime was not finite.

If the accumulation is stopped ($R = 0$), the number of particles left in a trap

after holding for a time t, assuming a constant loss rate, is given by

$$N(t) = N_0 e^{-t/\tau}. \tag{2.26}$$

The constraint on the number of particles that can be trapped, N_∞, can be circumvented by stacking a number of trapped particle 'clouds' into a region where the gas pressure is much lower and hence the lifetime can be longer. If the number density increases sufficiently, then a non-neutral plasma may form. In the 'single particle' regime, the motion of the trapped particle cloud is dominated by the trapping potentials and the single particle equations of motion are valid. If the particle density is increased, then inter-particle forces can no longer be neglected and the cloud instead approaches the plasma regime. In the plasma regime there is a significant self-generated electric field and the density of charged particles causes Debye screening, where the external trapping fields are weakened within the plasma by the strong internal field and rearrangement of the charges.

A non-neutral particle ensemble with temperature T is considered to be in the plasma regime, where inter-particle dynamics are important, if three criteria are met [Chen, 2016]. To satisfy the first condition, the number density n_0 must result in the Debye length, defined as

$$\lambda_D = \sqrt{\left(\frac{\epsilon_0 k_\mathrm{B} T}{q^2 n_0}\right)}, \tag{2.27}$$

being much less than the length of the ensemble, L, where q is the charge of a particle, ϵ_0 is the permittivity of free space and k_B is the Boltzmann constant. The second condition is that the number of charged particles in a sphere of volume with radius equal to the Debye length is much much greater than one, $N_D \ggg 1$. This ensures there are enough charged particles to consider collective behaviour as a statistically valid concept. The final condition is that for a plasma oscillating at an angular frequency, ω_p, with a mean collision time with neutral atoms, τ_c, their product must be greater than one, i.e., $\omega\tau_c > 1$. This ensures the plasma is dominated by electrostatic interactions, as opposed to behaving like a neutral gas.

In these studies, the 2-stage trap was typically operated with a 1 s accumulation time, giving a positron cloud of 8×10^4 particles in the 3rd stage, occupying an ellipsoid of radius 2 mm and length 10 mm at temperature 0.2 eV. These values result in a Debye length of $\lambda_D \approx 3.4$ mm such that the particles are in the

single particle regime.

Chapter 3

The 3rd Stage Harmonic Potential Well

A 1D harmonic potential follows the form $\phi(z) \propto z^2$. In a harmonic potential well, the axial motion of trapped charged particles exhibit simple harmonic motion, and so in a Penning trap, the axial bounce frequency is independent of the parallel energy, $E_{\parallel}$, which is the energy of the motion along the z-axis. This is desirable, for example, when applying a rotating wall electric field for compression at a specific frequency, as is discussed in chapter 4. A larger harmonic region of a trapping potential also allows resistive cooling to occur at higher particle energies, as more particles can oscillate at resonance with the cooling circuit, which is detailed in chapter 5.

This chapter describes the implementation of a harmonic potential well in the 3rd stage accumulator. The positron cloud was characterised by measuring observables such as the number of accumulated particles, motional frequencies, lifetime, energy, and temperature. These quantities were important to perform and evaluate rotating wall compression in chapter 4, and cooling by an external resistive circuit in chapter 5.

3.1 Penning Trap Electrostatic Potential

Trapped charged particles are usually confined in a small volume at the centre of a trap. The electrostatic potential at the centre of a Penning trap [Brown and Gabrielse, 1986] can be written as a general solution to Laplace's equation (equation 2.6).

As the potential in a Penning trap has rotational symmetry about the z-axis, i.e. azimuthal symmetry in spherical polar coordinates (r, θ, φ), the potential $\Phi(r, \theta)$ is not a function of φ. To quantify the geometric imperfections in the potential, as azimuthal symmetry is maintained, it can be expanded in Legendre polynomials [Gabrielse *et al.*, 1989],

$$\Phi(r, \theta) = \sum_{n=0}^{\infty} A_n r^n P_n(\cos\theta), \tag{3.1}$$

where $P_n(\cos\theta)$ are Legendre polynomials of the n$^{\text{th}}$ degree. A_n are the geometry parameters given by

$$A_n = \frac{2}{(n+\frac{1}{2})\pi} \frac{\sin(k_n z_0)}{I_0(k_n r_0)}, \tag{3.2}$$

where I_0 is the modified Bessel function of the first kind, of order zero, and

$$k_n = \left(n + \frac{1}{2}\right) \frac{\pi}{L_z}, \tag{3.3}$$

with L_z as half the total axial length of the trap (as illustrated in figure 3.1). As the electrodes and potentials considered here will also have reflection symmetry at the centre of the trap (i.e. at $z = 0$), the potential Φ must be even in z, therefore for odd values[‡] of n, $A_n = 0$. Applying a voltage U_0 between the endcaps and the centre electrode, the total electrostatic potential inside the trap is

$$\phi(r, \theta) = U_0 \, \Phi(r, \theta) = U_0 \sum_{\substack{n=0 \\ \text{even}}}^{\infty} A_n r^n P_n(\cos\theta). \tag{3.4}$$

As particles are confined within a small volume at the centre of the trap, it is unnecessary to calculate the potential for a larger volume [Vogel, 2018].

The characteristic trap dimensions are defined by a quantity d, which comprises of the minimum axial and radial distances from the centre of the accumulator to the electrodes, z_0 and r_0 respectively [Brown and Gabrielse, 1986], by

$$d^2 = \frac{z_0^2}{2} + \frac{r_0^2}{4}. \tag{3.5}$$

Then for $r \ll d$, near the centre of the trap, the potential from equation 3.4 can

[‡]Imposing harmonicity is stricter as it also requires that for all $n > 2$, then $A_n = 0$.

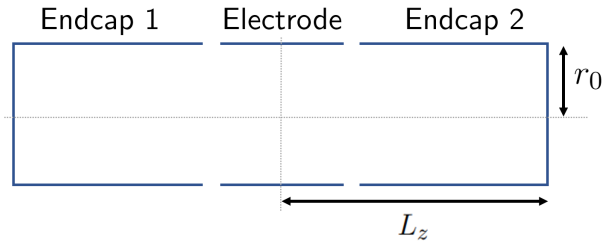

Figure 3.1: A schematic of a Penning trap with a single cylindrical electrode and two cylindrical endcaps, which is the geometry used to calculate the resultant electric potential from an electrode using equation 3.12.

be re-written as

$$\phi(r,\theta) = \frac{U_0}{2}\sum_{\substack{n=0\\ \text{even}}}^{\infty} C_n \left(\frac{r}{d}\right)^n P_n(\cos\theta), \tag{3.6}$$

where the conventional expansion coefficients $C_n = 2d^n A_n$ have been introduced. The expansion coefficients, C_n, can be calculated by solving the Laplace equation with appropriate boundary conditions, and then fitting the potential near the centre to the series [Brown and Gabrielse, 1986]. The lowest-order terms will dominate for particles close to the centre of the trap, and so expanding only the first three non-zero terms, expressed in cylindrical coordinates (r, φ, z), gives

$$\phi(r,z) \approx \frac{U_0 C_0}{2} + U_0 C_2 \left(\frac{z^2 - \frac{1}{2}r^2}{2d^2}\right) + U_0 C_4 \left(\frac{z^4 - \frac{6}{2}z^2 r^2 + \frac{3}{8}r^4}{2d^4}\right), \tag{3.7}$$

which when on-axis, reduces to

$$\phi(r=0,z) \approx \frac{U_0 C_0}{2} + \frac{U_0 C_2}{2d^2} z^2 + \frac{U_0 C_4}{2d^4} z^4. \tag{3.8}$$

The zeroth-order term, C_0, is an absolute potential offset and therefore irrelevant for particle motion, while the odd terms cancel due to the axial symmetry, as previously stated. The coefficient C_2 accounts for the cylindrical electrode geometry and is the desired quadrupole contribution for electrostatic confinement and hence the depth of the potential well. In an ideal trap, it is the only coefficient with a contribution to the potential and in cylindrical Penning traps, typically $C_2 \sim 0.5$ [Vogel, 2018]. C_4 is the octupole component of the electrostatic potential and the coefficient generally specifying the largest trap imperfection, which is undesirable and results in the oscillation frequencies being energy dependent. In cylindrical Penning traps, C_4 and C_6 are inherently non-zero due to their cylindri-

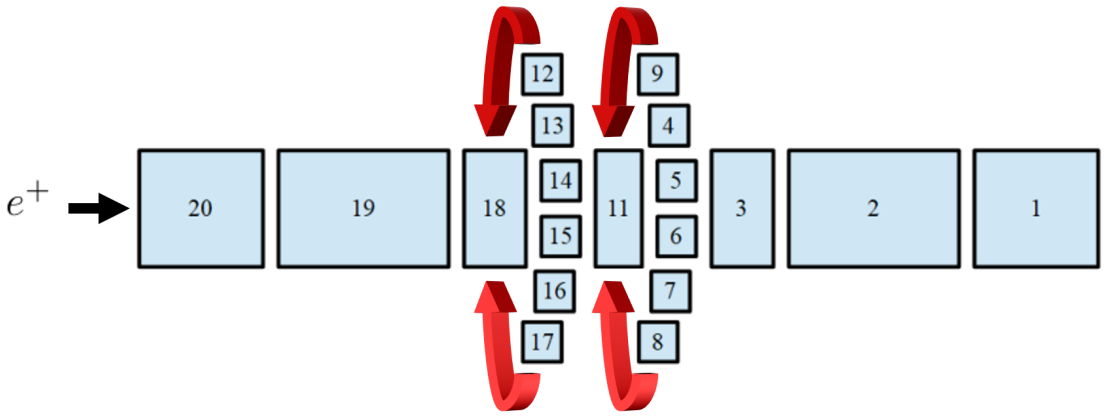

Figure 3.2: Schematic of the cylindrical electrodes in the 3rd stage accumulator, also shown as a CAD drawing in figure 2.7, with the corresponding numbering system. The numbers correspond to the electrical connections on a BNC breakout box, where the six-segment rotating wall electrodes upstream from the centre are E17–12, whilst downstream they are E9–4.[§] The red arrows illustrate that the segmented electrodes wrap around the axis forming two cylinders.

cal geometry but have additional contributions due to misalignment and machining imperfections which may also introduce odd C_n terms. During electrode design, C_4 can be made approximately zero using mechanical compensation by adjusting the inner radius to endcap distance ratio such that $r_0/z_0 = 1.203$ [Gabrielse and Mackintosh, 1984]. Choosing a long ring electrode near the centre of the trap can also be a beneficial design feature, as it enables a greater image signal pick-up, which is discussed in chapter 5. The length of the centre electrode in the 3rd stage was not designed to tune out C_2, but instead optimised for the linearity of the double rotating wall, as detailed in chapter 4.

Charged particles with less parallel kinetic energy than the height of the confining potential become trapped, and their axial oscillation frequency in an imperfect harmonic well is determined from the solution of the axial equation of motion, as was shown in section 2.9, but using the non-ideal potential in equation 3.8. To lowest order this gives

$$\omega_z^2 z = \frac{q}{m}\frac{\partial \phi}{\partial z}, \tag{3.9}$$

such that

$$\omega_z = \sqrt{\frac{qU_0}{md^2}C_2}, \tag{3.10}$$

[§]Note that no electrode named E10 exists, due to a historical fault during installation.

Table 3.1: The 3rd stage accumulator electrodes listed from upstream to downstream, with their lengths and applied biases for an electrostatic potential well which is approximately harmonic in z. The internal radius of each electrode is $r_0 = 20.5$ mm.

Electrode	E20	E19	E18	E17–12	E11	E9–4	E3	E2	E1
Voltage [V]	134.9	103.5	41.5	27.5	23.5	27.5	41.5	103.5	134.9
Length [mm]	37	49	18	19	21	19	18	49	37

which is a modification of the ideal equation 2.10b, that reduces to the ideal Penning trap case when $C_2 = 1$.

3.2 Superposition of the Laplace Equation Solution

The electric field for axial containment is found by solving Laplace's equation (equation 2.6). For a cylindrical Penning trap of inner radius r_0 and total length $2L_z$, with endcaps as shown in figure 3.1, the azimuthally symmetric solution [Gabrielse *et al.*, 1989] in cylindrical coordinates (r, φ, z) near the centre of the trap is

$$\phi(r, z) = U_0 \sum_{n=0}^{\infty} A_n I_0 \left(k_n r\right) \cos\left(k_n z\right), \tag{3.11}$$

substituting for A_n from equation 3.2, gives explicitly

$$\phi(r, z) = 2U_0 \sum_{n=0}^{\infty} \frac{I_0 \left(k_n r\right) \sin\left(k_n z_0\right) \cos\left(k_n z\right)}{(n + \frac{1}{2})\pi \; I_0 \left(k_n r_0\right)}, \tag{3.12}$$

which is the quantity calculated for each cylindrical electrode. A total axial potential was then obtained from the superposition of the electric potential from each of the electrodes in the 3rd stage accumulator. The on-axis distance a particle with a given parallel energy could travel was calculated, to give the axial bounce frequency as a function of parallel energy within the potential, $f_z(E_{\|})$.

3.3 Potential Well Computational Optimisation

To obtain a harmonic potential well in the 3rd stage, the electrode voltages were determined using a computational optimisation routine. Nine DC voltages are

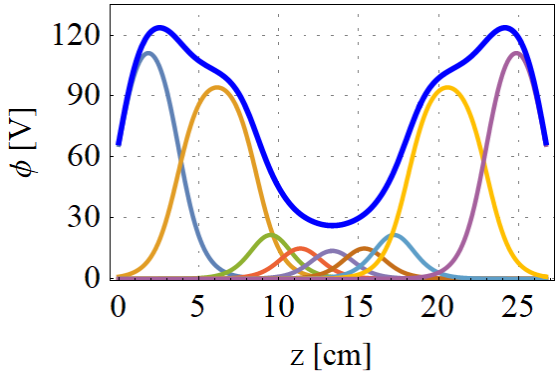

Figure 3.3: The on-axis electric potential produced by each electrode from table 3.1 is shown by the nine smaller peaks in various colours, while the sum of the potentials is shown as the thicker blue line. The distance, z, is relative to the entrance of the 3rd stage accumulator.

required to bias the electrodes in the 3rd stage accumulator, as illustrated by figure 3.2, but as the harmonic potential must be symmetric about the centre electrode, only five voltages needed to be determined. These were subject to the constraints that 140 V $\geq$ V_{E20} $\geq$ V_{E19} $\geq$ V_{E18} $\geq$ $V_{E17–12}$ $\geq$ V_{E11}, where the voltage applied to the entrance electrode is V_{E20}, and V_{E11} is the voltage applied to the centre electrode. The limit on the maximum applied voltage of 140 V is the maximum DC output voltage from the Llachar amplifiers, and the minimum of the potential well was required to equal the minimum parallel energy of the incoming positrons which was 26.2 eV, as determined experimentally in section 3.8.

In the computation, each electrode voltage was systematically increased in 50 mV steps over the entire the parameter space and the Laplace equation solved for each configuration, using the superposition theorem to calculate the total electric potential. The deviation of the resultant potential from the ideal fitted form of $\phi \propto z^2$ was calculated for the central 30 mm of the potential, which trapped particles would occupy presuming a maximum parallel energy spread of $\approx$ 3 eV, which was a cautious over estimate. This deviation was minimised to give the optimal potential well.

In table 3.1, the optimised set of electrode voltages are given along with the corresponding lengths, while a plot of the resultant total electric potential, obtained from the superposition of each electrode, is shown along with the individual electrode potentials in figure 3.3. The total potential is then compared with an ideal fitted harmonic potential in figure 3.4, showing good agreement with $< 4.5\%$ deviation from the quadratic form for the presumed maximum particle energy spread

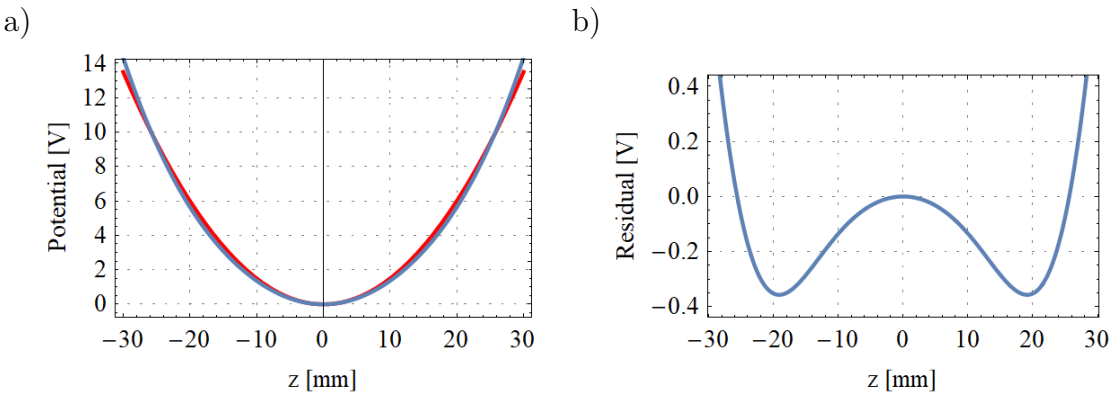

Figure 3.4: a) The calculated on-axis electric potential, $\phi(z)$ (blue), and the ideal harmonic form (red), which has been centred to the centre of the 3rd stage. Calculated data were fitted with the ideal harmonic form $\phi(z) = Az^2$, giving the constant $A = (1.500 \pm 0.003)$ V cm^{-2}. b) The difference between the calculated values and the ideal form for the potential is then plotted as a residual plot. Resultant shifts in axial bounce frequency, due to the deviation from the ideal form, are shown in figure 3.5.

of 3 eV.

3.4 Determining Motional Frequencies *A Priori*

The motional frequencies of a trapped charged particle in the harmonic potential well could be predicted using theory. From the superposition of the Laplace equation solution for each electrode (section 3.2), the axial bounce frequency for a single on-axis particle in this harmonic potential well was calculated to be $f_z \approx 11.04$ MHz, and the variation with energy due to the anharmonicity, $f_z(E_\parallel)$, is described using the axial period, $\mathcal{T}_z$, by

$$f_z(E_\parallel) = \frac{1}{\mathcal{T}_z} = \sqrt{\frac{e}{2m}} \left(\int_{z_1}^{z_2} \frac{dz}{\sqrt{E_\parallel - \phi(z)}} \right)^{-1}, \tag{3.13}$$

where $E_\parallel$ is in eV, and z_1 and z_2 are the solutions of $E_\parallel = \phi(z)$, i.e. the minimum and maximum axial position of a trapped charged particle of parallel energy $E_\parallel$. A plot of $f_z(E_\parallel)$ is shown in figure 3.5 where f_z on-axis is predicted to vary by < 300 kHz for a parallel energy spread of 3 eV, which represents a frequency width of $< 3\%$ in f_z. The particle axial bounce frequency width is important when estimating the quality factor of a resistive cooling circuit, as detailed in

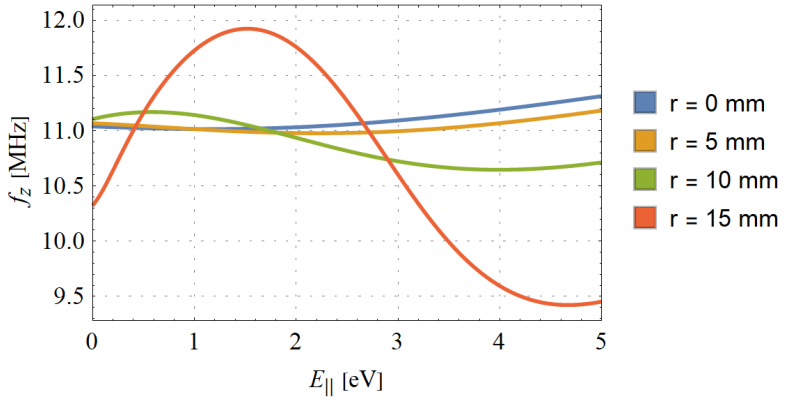

Figure 3.5: Calculated on-axis axial bounce frequency, f_z, in the 3rd stage optimised harmonic potential as a function of particle parallel energy, $E_{||}$, at various radial positions. The internal radius of the electrodes is $r_0 = 20.5$ mm. In this potential, the on-axis value of f_z varies by $< 3\%$ in the 0–3 eV energy range, corresponding to a total frequency width of ≈ 300 kHz.

chapter 5. Considering off-axis particles with $E_{||} \approx 0$ eV, then $r = 15$ mm gives $f_z \approx 10.3$ MHz. An empirical value of f_z between around 10.3 MHz and 11.1 MHz may therefore be accounted for by the radial position of the particles.

To further computationally characterise the stability of the bounce frequency, the potentials from each electrode were varied slightly about their desired values. This was to simulate the possible effects of uncalibrated applied biases or a build-up of space charge in the accumulator, which would change the trapping potential causing a change to the oscillation frequencies [Jeffries *et al.*, 1983]. The voltage on the second and penultimate electrodes (E19 and E2 respectively) were lowered by a worst-case estimate of 1 V, to 102.5 V, causing a calculated shift in f_z of -21 kHz, while lowering by 3 V to 100.5 V caused a -65 kHz shift. Increasing the centre electrode voltage by 1 V, to create a more flat-bottomed well also causes a shift of -21 kHz, while increasing by 0.5 V causes a -13 kHz shift. These frequency shifts are relatively small, but are large enough to observe when varying a sinusoidal driving frequency and measuring the number of trapped particles remaining. Uncalibrated biases would result in a constant offset observed from the calculated value of f_z, provided it would not drift significantly during experimentation. Such variations would also affect the harmonicity of the potential and undesirably result in a more energy dependent axial bounce frequency, which would also cause deviation from the calculated values of $f_z(E_{||})$.

The cyclotron frequency can be approximated using equation 2.10a, using

the calculated magnetic field strength in the 3rd stage of 37.7 mT, which gives $f_c \approx 1.06$ GHz. Using the calculated axial bounce frequency of $f_z = 11.04$ MHz, the magnetron frequency can then be computed from equation 2.18 and by substituting for the free cyclotron frequency from equation 2.10a gives

$$f_m \approx \frac{\pi m f_z^2}{eB}, \tag{3.14}$$

which using the calculated magnetic field strength in the 3rd stage again, provides $f_m \approx 58$ kHz. The magnetron and axial bounce motion are both able to be driven with available hardware, whilst the cyclotron motion is too fast.

3.5 Experimental Recapture and Ejection Optimisation

Tuning the static biases for the electric potential during catch, hold, and eject cycles was an essential part of minimising particle loss and disturbance of the energy distribution. To minimise changes to the harmonic potential well in the 3rd stage during the catch sequence, the centre electrode and subsequent electrodes downstream (E11, E10–4, E3, E2 and E1 respectively) were pre-set to the desired bias.

When transferring positrons from the 2-stage trap to the 3rd stage accumulator, timing is important for maximising the transfer efficiency. The delay time between ejection from the 2-stage and catching in the 3rd stage was varied whilst detecting the number of retrapped positrons, as shown in figure 3.6. A mean delay of (0.589 ± 0.001) μs was found before the positrons were first caught. This is the time of flight between the 2-stage and the 3rd stage. If the positrons are not caught, they are retarded back towards the raised exit potential of the 2-stage and can bounce between these two locations until being trapped later or lost. In figure 3.6 this is shown by the series of peaks which are a mean of (1.178 ± 0.002) μs apart, which is twice the time of flight between the 2-stage and 3rd stage, as expected due to each additional round trip. It is also seen that the time width of the peaks increases with delay time due to the parallel energy distribution of the cloud. Some positrons are lost during the transfer and a decrease in the number of retrapped positrons is seen with increasing delay time, thus the positrons should be retrapped at the first opportunity, as this gives the largest positron number

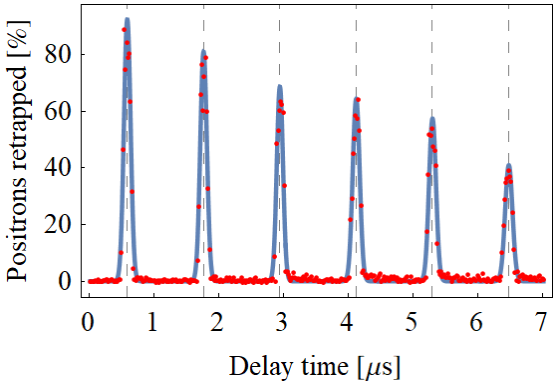

Figure 3.6: The number of retrapped positrons as a function of delay time between ejection from the 2-stage trap and raising the potential at the entrance of the 3rd stage accumulator for retrapping. Data (red) are fitted with a series of six unconstrained Gaussian peaks, shown as the blue line. The first peak is seen after (0.589 ± 0.001) μs with a time width of $\sigma = (51 \pm 2)$ ns, and the mean time between each peak is (1.178 ± 0.002) μs. Positrons are retarded when the potential at the entrance of the 3rd stage has not been lowered sufficiently, and bounce between the raised potential at the exit of the 2-stage and the entrance of the 3rd stage, such that retrapping can occur later.

and therefore maximum transfer efficiency.

The minimum of the trapping potential was set to match the minimum energy of the incoming parallel energy distribution of the particles, discussed further in section 3.8. As a result, the bias applied to the centre electrode was 23.5 V, and all but the first electrode on the entrance side of the centre (E19, E18 and E17–12) were kept at this value prior to catching. This led to an increase in the detected number when compared with grounded entrance electrodes, as the incoming parallel energy distribution is maximally slowed by the retarding potential, without blocking any particles and decreasing the trapped particle number.

Fast nanosecond high voltage pulse generators were trialled for both the particle catch and eject in both the 2-stage and 3rd stage, but their jitter and fast rise/fall on the gate electrodes was empirically found to retain less particles than a slower catch/eject. The catch was most effective using the Llachar DC amplifiers with their ~ 10 μs 10–90% rise time. Starting the entrance electrode of the 3rd stage (E20) at a negative potential then allowed finer temporal tuning than was otherwise possible. Once the entrance potential was sufficiently high to trap the particles, the remaining potentials (on E19, E18 and E17–12 respectively) were raised sequentially with the minimum time step of 3 μs between each, for the de-

sired harmonic well. Raising these remaining potentials simultaneously decreased the detected particle number, and the mean parallel energy and its spread were increased, thereby suggesting particles were being undesirably heated. As a result, the potentials were raised sequentially instead.

For ejection, the optimal sequence was found by sequentially lowering the barrier voltages from the exit inwards, i.e. E1, E2, E3, then E10–4 respectively, with appropriate time delays. Using the Llachar DC amplifier fall rate of ≈ 10 V/μs, the electrode biases were timed to reach ground concurrently. This was done by lowering the bias on E1 3 μs before lowering E2, and lowering E2 6 μs before E3, before finally lowering E3 and E10–4.

Further improvements in the detected number were found by lowering E10–4, on the exit side of the central electrode, to 12.3 V as opposed to ground during ejection. This value was derived using the computation which solved the Laplace equation, as it maintained the existing harmonic potential well shape fully to ground, instead of the previous potential minimum value. This meant the potential well remained harmonic during ejection and reduced anharmonicity on the exit side.

As a result of these optimisations, a transfer, catch, and eject efficiency of 85% was achieved from the 2-stage to the 3rd stage. Another consequence of the aforementioned improvements was an increase to the positron lifetime in the 3rd stage, as it was initially < 50 ms, whilst the largest measured lifetime as a result of this study was over 60 s, as shown in section 3.7. The lifetime was particularly dependent upon the alignment of the magnetic field axis with the electrode axis, and the background gas pressure, which were not necessarily constant during the entire period of these studies, e.g., following the system being at atmospheric pressure or significant equipment installation, which could affect vacuum quality. The transfer efficiency and lifetime were therefore routinely checked prior to experimentation, as a diagnostic to ensure that conditions were comparable over many weeks.

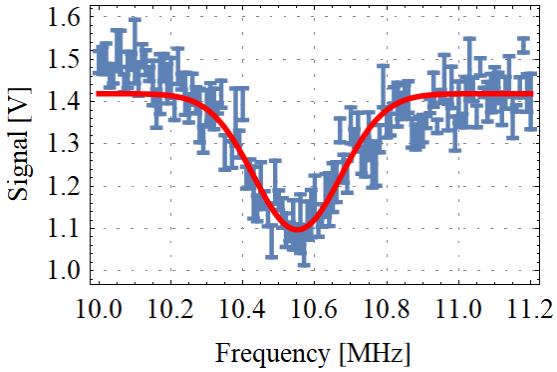

Figure 3.7: Positron number as a function of sinusoidal driving frequency, as measured by a CsI detector, with standard error on four repeats, fitted with equation 3.15 to give $f_0 = (10.551 \pm 0.007)$ MHz and $\sigma = (121 \pm 8)$ kHz. The frequency at which the most positrons have been driven out of the harmonic potential corresponds to a resonance near the axial bounce frequency of the cloud, thus $f_z \approx 10.55$ MHz.

3.6 Determining Motional Frequencies Experimentally

Destructive diagnostic methods were used to determine the motional frequencies of the positron cloud. As the driving frequency applied to an electrode by a sinusoidal function generator approaches a resonant frequency of the cloud motion, the radius of the particle motion increases which can cause annihilation against the surrounding electrodes. By iterating over a range of driving frequencies and detecting the remaining number of particles, the motional frequency is approximately given by the resonant frequency, f_0, at which the minimum number of remaining particles is observed. This is when the driving frequency is resonant with a motional frequency of the particles. To obtain an approximate value for f_0, a trough in the number of particles, N, provided it is symmetric, can be fitted by an arbitrary 1D Gaussian of the form

$$N(f) = B - A \exp\left(-\frac{1}{2}\left(\frac{f - f_0}{\sigma}\right)^2\right), \tag{3.15}$$

where A is the amplitude of the Gaussian and B is the particle number off-resonance.

The axial bounce motion was driven by applying a sinusoidally varying signal

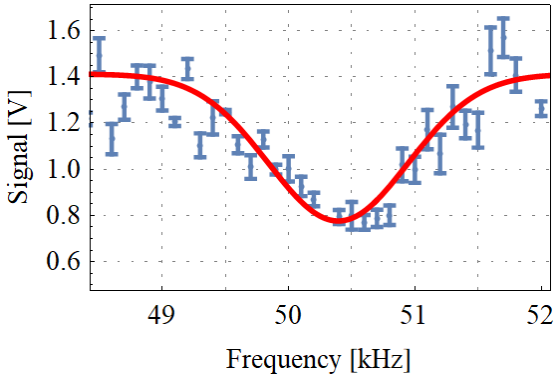

Figure 3.8: Positron number as a function of sinusoidal driving frequency, as measured by a CsI detector, with standard error of four repeats, fitted with equation 3.15 to obtain the resonant frequency at which most positrons have been driven out of the potential well, $f_0 = (50.4 \pm 0.1)$ kHz, with a width of $\sigma = (0.6 \pm 0.1)$ kHz. The resonant frequency corresponds to a resonance near the magnetron frequency of the cloud, giving $f_m \approx 50.4$ kHz.

of amplitude 2.5 V to the centre electrode in the 3rd stage (E11) for 0.1 s. This resonantly ejected positrons from the trap, and a minimum in the number of particles provided $f_z \approx 10.55$ MHz, as seen in figure 3.7. This agrees with the frequency expected from the electric potential (section 3.2) which was $f_z = 11.04$ MHz on-axis for $E_{\|} = 0$ eV, but dependent upon the radial position (illustrated by figure 3.5) may be between 10.3 MHz and 11.1 MHz, in agreement with the observed total frequency width. The empirical value of f_z is therefore explained by the radial position of the particles being between $r = 0$ mm and $r \approx 15$ mm. Some minor non-idealities may also be present due to driving the axial motion along the accumulator axis, with imperfect alignment to the magnetic field axis, causing a change to the radial position of the particles and shifting the resonant frequency from the ideal case.

Similarly, the magnetron motion of the cloud was driven for 0.5 s with a sinusoidal signal of 5 V amplitude, applied to a segmented electrode (E13) giving $f_m \approx 50.4$ kHz, as shown in figure 3.8. This estimate is broadly in agreement with the predicted value of $f_m \approx 58$ kHz from section 3.4, but instead using the empirical value of f_z in equation 3.14 predicts $f_m \approx 53$ kHz, providing better agreement with the observation. The deviation of 5% is most likely due to the predicted value relying upon a calculated value of the magnetic field strength, B, which is not empirically known. The radial motion of the cloud was also driven asymmetrically with a relatively large amplitude, using one segment of an off-centre six-segment

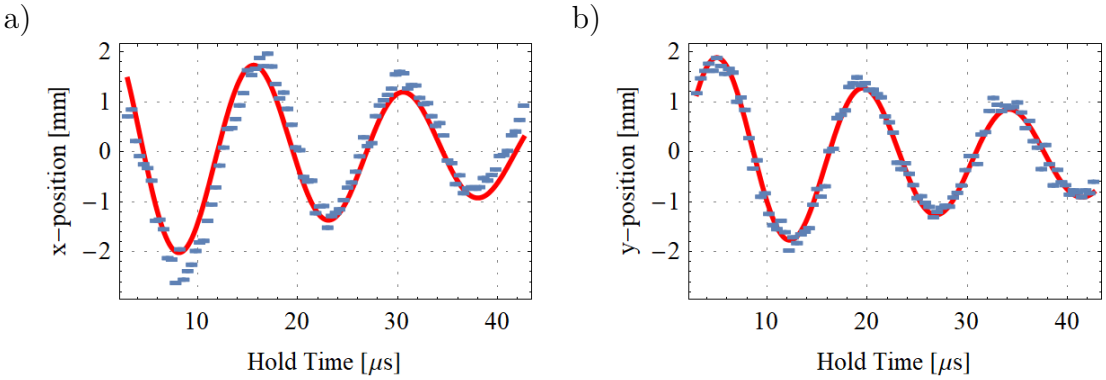

Figure 3.9: x–y plane positron cloud centre as a function of hold time, from MCP images fitted by a 2D Gaussian from equation 2.1. The data represent single measurements, where the error bars are the uncertainty in position from the 2D Gaussian fitting. a) x-position as a function of hold time, fitted with equation 3.16a in red and centred to give the magnetron frequency $f_{m,x} = (66.9 \pm 0.5)$ kHz. b) y-position as a function of hold time, fitted with equation 3.16b in red to give the magnetron frequency $f_{m,y} = (68.6 \pm 0.3)$ kHz.

electrode, which would in addition have driven the axial motion and coupled it with the radial motion, potentially causing a shift in the observed resonant frequency. For a more precise measurement of the magnetron frequency, a second method was used.

The magnetron frequency was independently verified by imaging the cloud position and intensity with time, using the MCP and camera, and fitting its 2D Gaussian centre (x_0, y_0) using equation 2.1, which gives a time varying sinusoidal signal. The sinusoidal waves have the form

$$x(t) = A_x(t)\sin(2\pi f_{m,x}t + \theta_x) + x_0, \tag{3.16a}$$

$$y(t) = A_y(t)\cos(2\pi f_{m,y}t + \theta_y) + y_0, \tag{3.16b}$$

where the oscillation amplitudes, $A_{x,y}(t) = A_{x,y}(0)\exp(-t/\tau_{x,y})$, and magnetron frequency, f_m, in x and y are distinct to allow for elliptical orbits. This gave $f_{m,x} = (66.9 \pm 0.5)$ kHz and $f_{m,y} = (68.6 \pm 0.3)$ kHz, as shown in figure 3.9, which is $\approx 18\%$ larger than the calculated value. The discrepancy is explained by the difference in magnetic field strength at the MCP detector, as $f_m \propto 1/B$ (from equation 3.14), where B is $\approx 15\%$ smaller than inside 3rd stage accumulator. Taking this into account implies $f_m \approx 58$ kHz within the B-field of the 3rd stage, which agrees with the original calculation. The central position of the magnetron

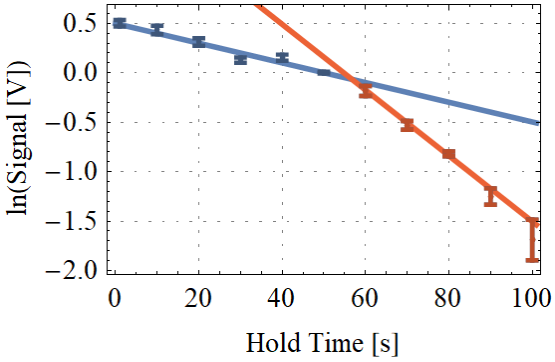

Figure 3.10: Natural logarithm of positron number as a function of hold time in the 3rd stage, as measured by a CsI detector, with a linear least squares fit to highlight the two component lifetime. Fitting equation 2.26 to the positron number gave a lifetime $\tau = (101.1 \pm 9.7)$ s in blue for the first 50 s and $\tau = (29.9 \pm 2.0)$ s shown in red afterwards. Radial expansion eventually causes the positrons to annihilate against the vacuum chamber after $\approx$ 55 s, causing additional loss and a decrease in the lifetime.

orbit radius is shown to slightly drift during this time window, which can be attributed to the cloud being loaded into the 3rd stage slightly off-axis, due to a magnetic field misalignment. In addition, the magnetron amplitude decreases which also suggests a transfer of energy to the radial motion.

The cyclotron frequency was too fast to be driven or imaged by available hardware, so substituting the empirically obtained values of f_m (from figure 3.8) and f_z into equation 2.20 gives $f_c \approx 1.09$ GHz which is only 3% higher than the calculated value. Measuring the motional frequencies was important, as it enabled the frequency tuning of cloud manipulations, such as rotating wall compression and resistive cooling, which needed to be near f_z.

3.7 Lifetime Measurements

For a stable positron number, at least on the timescale of experiments in the 3rd stage, a sufficiently long lifetime was required. This would give ample time to perform manipulations, such as rotating wall compression (see chapter 4) and cooling measurements (in chapter 5). Observing these effects would require trapping positrons for a few seconds, and thus a lifetime of $\gtrsim 5$ s was sought.

A lifetime measurement was performed by keeping the accumulation time in the 2-stage trap constant at 1 s, and varying the hold time in the harmonic potential

well in the 3rd stage and measuring the signal on a CsI detector after ejection. The mean trapping lifetime, τ, was obtained by fitting equation 2.26 to the data. An example of this is shown in figure 3.10.

Initially the positron lifetime was < 30 ms, partially due to misalignment between the magnetic field and the axis of the 3rd stage electodes which introduced non-idealities. Prior to these studies, this was often compensated for by using a 'magnetron kick' [Mortensen *et al.*, 2013] to radially offset the cloud during ejection from the 2-stage trap.

Improving the alignment of solenoid 3 allowed a lifetime of tens of seconds to be achieved in the harmonic potential, without the use of radial compression, as shown in figure 3.10. The lifetime shown has two components, as after ≈ 55 s radial expansion causes additional losses as positrons begin to annihilate against the electrodes. The use of rotating wall electric fields, described in chapter 4, can counteract radial expansion and allow a longer lifetime to be obtained but no rotating wall was wanted for initial resistive cooling measurements, as a driving force complicates the system, thus a long natural lifetime is important. Positron signal was still seen for hold times of 100 s, which was sufficient time for resistive cooling and temperature measurements to be performed, as required.

3.8 Parallel Energy Measurements

Applying a retarding potential U at some point along the axis allows measurement of the parallel kinetic energy distribution of the cloud. Only particles, n, with energy $E_{\parallel} > U$ can pass the potential barrier, so by scanning the voltage for successive measurements of accumulated clouds, the integrated parallel energy distribution can be determined [Eggleston *et al.*, 1992]. If the energy spread is assumed to be Gaussian, then the signal size against retarding potential is fitted by the complementary error function,

$$n(E) = \frac{N}{\sqrt{2\pi}\sigma} \int_{E}^{\infty} \exp\left(\frac{-\left(E' - E_0\right)^2}{2\sigma^2}\right) \mathrm{d}E' = \frac{N}{2}\mathrm{erfc}\left(\frac{E - E_0}{\sqrt{2}\sigma}\right), \tag{3.17}$$

thereby quantifying the parallel energy distribution.

A measurement of the parallel kinetic energy distribution for positrons ejected from the 2-stage trap and arriving at the 3rd stage was performed. A sequence of measurements, varying the retarding potential on the 3rd stage electrodes, obtains

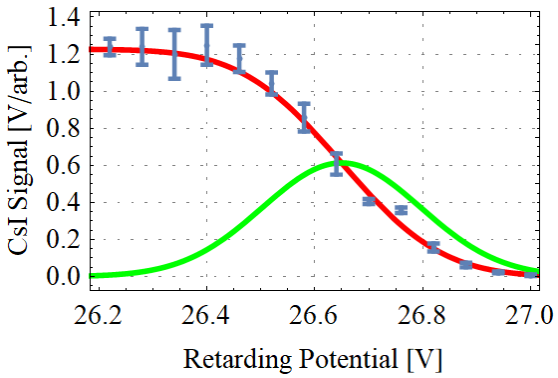

Figure 3.11: Measurement of the complementary cumulative distribution function for the positron parallel energies ejected from the 2-stage. The blocking voltage was applied to the 3rd stage electrodes, using the MCP as the annihilation target. The data are fitted in red by equation 3.17, where $E_0 = (26.650 \pm 0.008)$ eV, and $\sigma = (0.147 \pm 0.007)$ eV. The corresponding Gaussian probability density distribution is plotted in green. Each point is the mean and standard error of three CsI detector signals.

a cumulative distribution function, as shown in figure 3.11. These measurements allowed the minimum of the harmonic potential well to be set at 26.2 V to match the minimum parallel energy of the positron cloud. Applying the maximum retarding potential, without blocking, allows maximal slowing of the incoming particles. Doing so gives the maximal number of trapped particles. This was verified experimentally by varying a constant offset on all the electrode biases, which raised the potential whilst retaining its shape, and optimising for the largest detected number of particles.

A retarding potential measurement was also performed following a 5 s hold time in the 3rd stage harmonic potential well. The retarding voltage was applied to E3 (the third electrode from the exit) as the other exit electrode voltages were lowered during ejection. Fitting equation 3.17 to these data gives $E_0 = (18.449 \pm 0.003)$ eV and $\sigma = (0.107 \pm 0.003)$ eV, as shown in figure 3.12. Therefore, retrapping in the 3rd stage and holding in the harmonic well for 5 s reduced the energy width σ by ≈ 0.04 eV, which is $\approx 27\%$. As a result, a decrease in the total width of the parallel energy distribution of 99.7% of the positrons (corresponding to $\pm 3\sigma$ from the mean) from 0.88 eV to 0.64 eV was also observed, which is a $\approx 27\%$ reduction. E_0 of the positron cloud also decreased by ≈ 8.2 eV compared to when arriving at the 3rd stage, but this is predominantly attributed to the decreasing potential minimum in the 3rd stage during ejection.

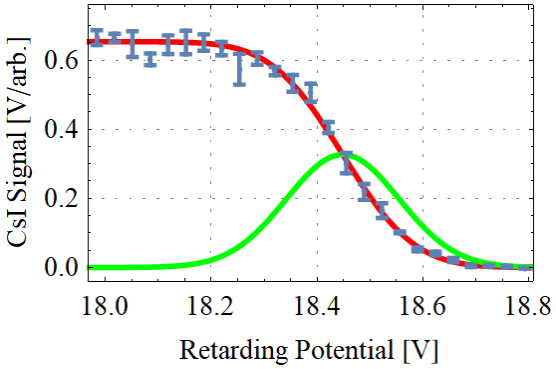

Figure 3.12: Measurement of the complementary cumulative distribution function for the positron parallel energies ejected from the 3rd stage after being trapped for 5 s in the harmonic potential. The retarding voltage was applied to E3 which has been scaled to on-axis potential, where the MCP was the annihilation target. The data are fitted in red by equation 3.17, where $E_0 = (18.449 \pm 0.003)$ eV and $\sigma = (0.107 \pm 0.003)$ eV. The corresponding Gaussian probability density distribution is plotted in green. Each point is the mean and standard error of four CsI detector signal heights.

Quantifying the positron parallel kinetic energy distribution aids optimisation of the trapping potentials, and provides an estimate for the range of axial bounce frequencies in the 3rd stage due to that energy distribution. This is important when understanding the interaction with a rotating wall and for designing a resistive cooling circuit, as will be shown in the subsequent chapters.

3.9 Single-shot Temperature Measurements

Positron temperatures are important as a diagnostic technique to quantify heating and cooling when manipulating a positron cloud. This is relevant to chapter 4 which discusses rotating wall compression and heating, and chapter 5 which details experiments to cool positron clouds using an external resistive circuit.

A single-shot 'high temperature' measurement method for electron plasmas was developed by [Beck, 1990] and published with detailed discussions in [Eggleston *et al.*, 1992] and [Beck *et al.*, 1996]. It is described as a single-shot measurement as it only requires one accumulated cloud or plasma, which is particularly advantageous if accumulation takes a relatively long time. The justification for using this technique in the single particle regime will be outlined in this section. The experimental method is the same, but it is presented with the rationale for non-

interacting charged particles. In general, the original arguments are simplified due to the absence of a plasma potential which complicates the model. It has been shown that a correction factor is needed to modify the temperature model in the plasma regime, but for a very low number of particles that this factor approaches 1 [Hart and Peterson, 2006]. This provides support for the validity of the temperature measurement in the single particle regime.

3.9.1 Assumptions

Listed below are the assumptions that are built into the temperature measurement model, and which conditions are required for these assumptions to be valid.

1. The parallel velocity distribution is Maxwellian.

2. All particles with a parallel velocity, $v_\parallel$, such that

$$\frac{mv_\parallel^2}{2} + e\phi > eV_b, \tag{3.18}$$

   escape past the potential energy barrier, eV_b, and are collected, in this case by an MCP which is used as a charge amplifier. The remaining parallel velocity distribution in the trap is then

$$f(v_\parallel) = \begin{cases} \text{const} \times \exp\left(-\frac{mv_\parallel^2}{2k_B T_\parallel}\right), & \text{if } v_\parallel < \sqrt{2e(V_b - \phi)/m}; \\ 0, & \text{otherwise,} \end{cases} \tag{3.19}$$

   where ϕ is the electrostatic potential.

3. $T_\parallel$ is independent of r, and V_b can be considered independent of r.

4. $\phi(r)$ is independent of V_b.

5. Only particles near the axis escape over the potential barrier.

These five assumptions and their importance will be described in further detail below.

1. Maxwellian parallel velocity distribution

The temperature of the cloud is measured assuming that $v_\parallel$ is Maxwellian, allowing $T_\parallel$ to be measured. For the temperature measurement, the exit potential barrier,

V_b, on one side of the well is slowly lowered to ground which causes the cloud to expand axially. For the cloud to remain Maxwellian during this expansion, the axial bounce period of a particle must be much faster than the rate at which V_b changes. This condition can be written given the axial bounce time of a thermal particle, $2l_c/v_T$, where v_T is the thermal velocity and l_c is the axial length of the cloud, as

$$\left| e\frac{dV_b}{dt} \right| \ll k_B T \frac{v_T}{l_c}. \tag{3.20}$$

This ensures that a particle escapes with an axial energy much smaller than the thermal energy, $k_B T$, so that all particles at the same radius and axial energy escape at approximately the same V_b. Notwithstanding this condition, the lowering of the potential barrier must remain faster than the collision and radial transport time [Beck *et al.*, 1996]. This ensures that the loss of energetic particles during measurement, which is a forced evaporative cooling process, does not affect the measured temperature. The subsequent energy redistribution at later times could also cause a deviation from the expected Maxwellian distribution, prior to rethermalisation. When the number of particles that have escaped is small, then the evaporative cooling effect on the remaining distribution will be small and so the assumption holds.

2. All particles with sufficient parallel velocity escape past the confining barrier

The condition for a particle to escape past a potential barrier V_b is given by equation 3.18. If V_b is a function of time, then ϕ can be further complicated as it may also depend on t and z. To a good approximation, the t and z dependence of ϕ can be ignored if equation 3.20 is satisfied, which ensures that $f(v_\parallel) = 0$ for $v_\parallel > \sqrt{2e(V_b - \phi)/m}$. The condition states that the confining barrier potential, V_b, must be lowered slowly compared to the axial bounce period, to allow the particles with sufficient energy (according to equation 3.18) travelling towards, and away from the barrier, to escape. Therefore, particles with sufficient energy but travelling in the opposite direction to the exit, can take a time of up to $2l_c/v_\parallel$ to escape, which ensures the assumption is met.

3. $T_{\parallel}$ is independent of r, and V_b can be considered independent of r

For long cylindrical barrier electrodes, the confinement potential ϕ does not vary significantly with radius, so to a good approximation $\phi_b \approx V_b$. For shorter electrode rings with a smaller aspect ratio, the confinement potential may vary with radius, i.e. $\phi(r)$, but it will be smallest on-axis. This coincides with the most energetic particles which are also on-axis. Due to these two factors, the on-axis particles will be first to escape. This means that the barrier potential on-axis is the important physical quantity and its radial dependence can be ignored. Thus, the barrier potential V_b and $T_{\parallel}$ can both be considered as independent of radius for the temperature measurement method.

4. $\phi(r)$ is independent of V_b

In the plasma regime, lowering the barrier potential and allowing particles to escape changes the plasma potential, ϕ_p, which alters the confining potential. Therefore, only the energetic tail of the Maxwellian distribution can be used, before the change in ϕ_p significantly affects the measurement. The mapping of $V_b \rightarrow \phi(r)$ is also complicated by the changing plasma potential and deducing it requires additional measurements with varying radius.

In the single particle regime, as there is no plasma potential, the loss of particles does not change the trapping potential, ϕ. This means a map of $V_b \rightarrow \phi(r)$ is more straightforward, as it only depends on the aspect ratio of the barrier electrode, which is constant. Due to the absence of a plasma potential, a larger portion of the Maxwellian distribution can be used to obtain the cloud temperature, subject to the timing constraints given in the first assumption. As a result, this may provide an aid to indicate whether trapped charged particles are in the single particle regime, or should be considered as a non-neutral plasma. If significantly less of the parallel velocity distribution is Maxwellian during the measurement, then it may indicate the presence of plasma effects.

5. Only particles near the axis escape over the potential barrier

Due to the cylindrical geometry of the trapping electrodes, as discussed in assumption 3, the confining potential is smallest on-axis. This is shown in figure 3.13, thus the $v_{\parallel}$ required to escape is smallest on-axis. The difference in axial potential on-axis and off-axis is shown in figure 3.14, which shows that the potential well is

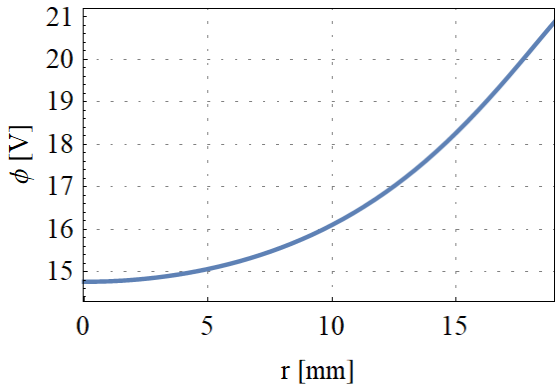

Figure 3.13: The calculated total radial electric potential in the 3rd stage, $\phi(r)$, at the centre of electrode E3 which applies the barrier voltage during the temperature measurement, obtained from the superposition of the Laplace equation solution for each electrode (section 3.2). When the axially confining potential on the exit is lowered, the first particles to escape will be the most energetic particles on-axis near $r = 0$. A confining barrier voltage of $V_b = 22$ V was chosen here which corresponds to when positrons begin to escape, and the internal radius of the cylindrical electrodes is $r_0 = 20.5$ mm.

deeper off-axis.

The perpendicular kinetic energy distribution of a charged particle cloud in the single particle regime will now be reviewed. Using the guiding centre approximation, the radial motion of a charged particle in a Penning trap comprises of a magnetron motion, which can be pictured as a rotation about a potential hill. If a particle at the centre of the potential well loses energy, then the amplitude of the magnetron motion, A_m, increases. The kinetic energy of the magnetron motion can be given by

$$E_m = \frac{1}{2} m \omega_m^2 A_m^2. \tag{3.21}$$

Rearrangement gives the amplitude of the magnetron motion in terms its kinetic energy,

$$A_m = \sqrt{\frac{2E_m}{m\omega_m^2}}. \tag{3.22}$$

When more than one charged particle is trapped, the statistics of the particle energy and the rate of thermalisation are affected by collisions between particles, and interactions with the background cooling gas. These interactions establish a thermal equilibrium between particles and can be considered as small perturbations to the average particle motion, given that the average energy of a particle is large compared with the time average of the Coulomb interaction potential. The

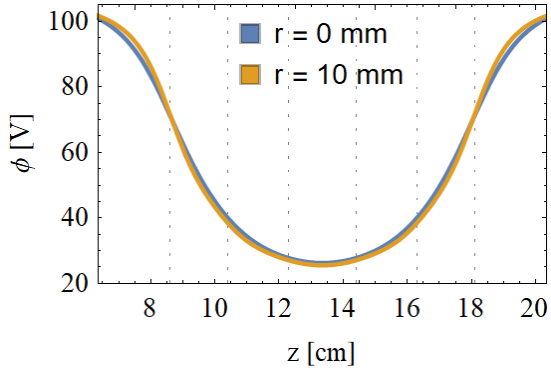

Figure 3.14: The calculated total electric potential in the 3rd stage harmonic well, for $r = 0$ mm (blue) on-axis and at $r = 10$ mm (orange). The axial position, z, is relative to the entrance of the 3rd stage accumulator, where the centre is at $z = 13.35$ cm, and the gridlines denote the edges of each electrode. The potential well is shown to be deeper off-axis and shallowest on-axis.

particle cloud can then be described as an ideal gas of non-interacting particles in thermal equilibrium [Major *et al.*, 2005]. Assuming an ensemble of non-interacting particles at radius r, then the Boltzmann thermal distribution is

$$N_r(E_m) \propto \exp\left(-\frac{E_m}{k_B T}\right). \tag{3.23}$$

Substituting for E_m in terms of the magnetron motion amplitude, from equation 3.21, gives

$$N_r(A_m) \propto \exp\left(-\frac{m\omega_m^2 A_m^2}{2k_B T}\right), \tag{3.24}$$

and so in the single particle regime, a thermal ensemble has a Gaussian distribution in the radial plane [Isaac, 2010]. This has been experimentally verified by an MCP image of the cloud, and is significant as the most radially energetic particles will be nearest the axis.

As the radial distribution of the cloud is well-described by a Gaussian, this supports that the velocity distribution is indeed Maxwellian and thus a temperature can be attributed to the ion cloud [Major *et al.*, 2005]. At the 'high temperatures' typically probed, temperature equilibration, where $T_\parallel \equiv T_\perp \equiv T$, is expected from conventional scattering theory [Hyatt *et al.*, 1987]. As clouds are usually held in the potential prior to measurement for a long time (~ 0.5 s) compared to the collision time, equilibration is expected. The equilibrium temperature for a given confining potential is then determined by the net effect of the heating from sources

such as electrical noise and rotating wall electric fields, and cooling mechanisms such as collisions with background gas.

3.9.2 Temperature Measurement Application

Using the assumptions from the previous section, the model for the temperature measurement will now be derived. The parallel velocity at equilibrium is described by a Maxwell distribution, given by

$$f(v_\parallel) \propto \exp\left(-\frac{mv_\parallel^2}{2k_B T_\parallel}\right). \tag{3.25}$$

At the point of escape from the trap, from equation 3.19, $v_\parallel = \sqrt{2e(V_b - \phi)/m}$, and the number of particles that escape as a function of barrier potential is

$$N_e(V_b) \propto \exp\left(-\frac{e(V_b - \phi)}{k_B T_\parallel}\right). \tag{3.26}$$

Therefore, using assumption 4, that $d\phi/dV_b = 0$, the gradient from a linear least squares fit of a plot of the natural logarithm of the number of escaped particles against barrier potential, i.e.

$$\frac{d\ln(N_e)}{dV_b} = -\frac{e}{k_B T_\parallel}, \tag{3.27}$$

can be used to extract the temperature. To measure $T_\parallel$, the linear least squares fit is used over the most energetic tail of the Maxwell-Boltzmann distribution. This process is repeated for each individual single-shot temperature measurement and a weighted mean and standard error calculated. Using this method, small random fluctuations which deviate from a Maxwellian parallel velocity distribution are averaged to approximately zero. This is the temperature measurement method which is already well-established for non-neutral plasmas [Eggleston *et al.*, 1992].

As the gradient of the detected charge plotted against potential is used to determine the temperature of the cloud, the exit voltage is not converted to on-axis potential. This is valid provided the voltage decrease during ejection is linear, as is shown in figure 3.15, as the applied voltage is directly proportional to the potential. In this experiment, the detected charge from the MCP and the exit voltage are measured simultaneously and can be plotted as in figure 3.16. As the

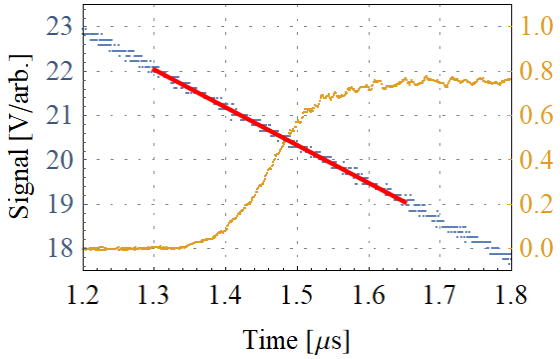

Figure 3.15: An example of the raw signals from a single-shot temperature measurement. The monitored exit voltage is plotted in blue, and fitted with a linear least squares in red, to give a exit voltage fall rate of $dV_b/dt = (-8.524 \pm 0.036)$ V/μs in the region of interest. The amplified charge from the MCP as a function of time, after a 0.1 s hold in the 3rd stage, is plotted in yellow. As the exit voltage is decreased, positrons begin to escape and the detected charge signal increases until a maximum, at which time all the positrons have been ejected from the well. The charge signal (yellow) is then plotted against exit voltage (blue) to obtain the temperature, as shown in figure 3.16.

MCP back plate is biased by using a high pass filter, the charge is detected as an integrated signal due to the relatively long time constant. A linear least squares fitting algorithm then takes the largest value from the noise floor and begins the fit once three sequential values for the detected charge exceed this value. The fit region is terminated when a fixed amount of charge has been measured, this was empirically set to an arbitrary level at $\sim 40\%$ of the maximum charge signal. The measured temperature as a function of time is then shown in figure 3.17, where it appears stable, such that the mean temperature is $T_{\parallel} = (0.321 \pm 0.001)$ eV, which corresponds to (3730 ± 10) K.

Positron temperatures will be presented in the following two chapters as a diagnostic technique to quantify heating due to rotating wall compression in chapter 4, and cooling by an external resistive circuit in chapter 5.

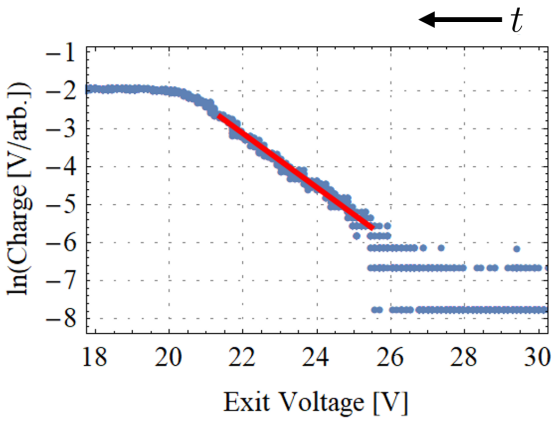

Figure 3.16: An example of the analysed signal from a single-shot temperature measurement. The natural logarithm of detected charge from the MCP is plotted as a function of exit voltage. As the exit voltage is decreased with time, positrons begin to escape and the charge signal increases until all the positrons have been ejected. From equation 3.27, a linear least squares fit over the region of interest, shown in red, allows the temperature to be obtained.

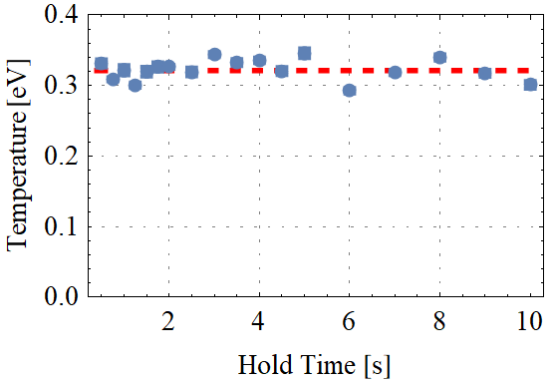

Figure 3.17: The temperature in the 3rd stage harmonic potential as a function of hold time, the temperature is not shown before 0.5 s to ensure the positron cloud has equilibrated. Each datum is the weighted mean and standard error of seven repeats. As the temperature appears to be at equilibrium, the weighted mean and standard error is $T_{\parallel} = (0.321 \pm 0.001)$ eV, plotted as a dashed red line.

Chapter 4

Rotating Wall Electric Fields

As energy is extracted from the magnetron motion of a charged particle in a Penning trap, the amplitude of the magnetron orbit due to the $E \times B$ rotation increases. This is illustrated by figure 4.1, and eventually the charged particle will be lost against the surrounding electrodes.

Ideally, the applied static fields for confinement are cylindrically symmetric, but in reality have small asymmetries due to, for example, imperfect construction [Notte and Fajans, 1994]. In principle, physically rotating the trap about its axis would ensure the asymmetries averaged to zero, but this is a highly impractical solution. Instead, the electric field can be rotated in the same direction as the particle radial motion by applying a time-varying sinusoidal voltage to split ring electrodes (see e.g. figure 2.7). This is the 'rotating wall' (RW) electric field [Huang *et al.*, 1997; Greaves and Surko, 2000] used for non-neutral plasmas, which can also control the central density of a cloud of non-interacting charged particles [Cassidy *et al.*, 2006a; Greaves and Moxom, 2008; Isaac *et al.*, 2011].

By varying the amplitude and frequency of the applied rotating electric field, charged particle clouds can be compressed, expanded, and manipulated. If the RW rotates with the direction of the radial motion of the cloud then radial compression can be observed, whilst if it counter-rotates then expansion is seen [Greaves and Surko, 2001]. Inducing inward radial transport diminishes radial loss from the trap, which is an important use for this technique as it increases the particle lifetime. Positron c1oud compression also has other advantages, such as allowing increased overlap with the laser system for Ps spectroscopy and excitation on the Swansea beamline.

Undesirably, RW compression induces heating of the cloud, and the thermal

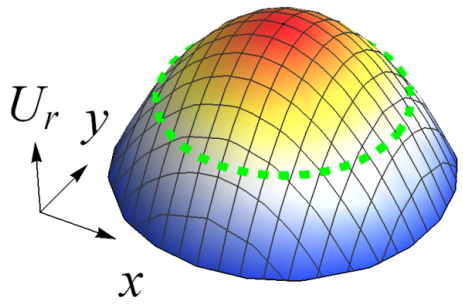

Figure 4.1: The magnetron motion of a charged particle in a Penning trap can be considered as a rotation about the top of a potential hill, shown by the dashed green line. When energy is lost, the particle orbits around the hill with a lower energy at a larger radius.

pressure then counteracts compression until equilibrium is reached. Equation 3.24 shows that the amplitude of the magnetron motion of trapped charged particles increases with temperature. If the positron temperature increases such that the energy exceeds the Ps formation threshold, Ps is formed which then annihilates. Inducing cooling mechanisms or reducing this heating therefore allows for greater positron retention, which was an aim of this study.

In a high magnetic field, which is larger than a few Tesla, the emission of cyclotron radiation may provide significant cooling. This is called radiative cooling and usually requires superconducting magnets, as the energy damping time constant [Knoop *et al.*, 2016] for the cyclotron motion is

$$\tau_r = \frac{3\pi\epsilon_0 m^3 c^3}{q^4 B^2}, \tag{4.1}$$

which is approximately $2.6/B^2$ seconds for the electron charge and mass, if B is in Tesla. The energy damping time constant is much longer for heavier charged particles such as a proton, where $\tau_r \approx 1.6 \times 10^{10}/B^2$ seconds. As a result, radiative cooling is only efficient for cyclotron motion damping of positrons or electrons in a Penning trap [Knoop *et al.*, 2016]. Such a strong field is often impractical due to cost or the necessity of a field free region, so cooling can be provided via collisions with a gas. For an effective cooling gas, the molecule-positron annihilation and elastic collision cross sections must be small to avoid loss and radial transport respectively, whilst the inelastic collision cross section, for processes such as vibrational and rotational excitation, must be large [Greaves and Surko, 2000]. In

Table 4.1: Parameters for various cooling gases at a pressure of 2×10^{-8} torr ($\approx 2.7 \times 10^{-8}$ mbar): annihilation time, τ_a; measured cooling time, τ_c; and vibrational quanta, E_ν. Data from [Greaves and Surko, 2001].

Gas	τ_a [s]	τ_c [s]	E_ν [eV]
SF_6	2190	0.36	0.076, 0.188
CF_4	3500	1.2	0.157
CO_2	3500	1.3	0.291, 0.083
CO	2400	2.1	0.266
N_2	6300	115	0.292

general, the cooling gases used on the Swansea beamline are CF_4, SF_6, or CO_2 as they have short cooling times as shown in table 4.1. For these studies, CF_4 was the cooling gas that was used. Inelastic scattering from a cooling gas is the most common cooling mechanism currently employed on low energy positron accumulators, but chapter 5 details the development of resistive cooling as an alternative.

An unresolved challenge to further develop the RW technique is to overcome the current experimental maximum particle density limit [Danielson *et al.*, 2015]. The implementation of a double RW endeavours to achieve this.

4.1 Single Rotating Wall in the 2-Stage Trap

The RW technique creates a rotating dipole around the trap axis, which is parallel to the axis of the magnetic field. Azimuthally split electrodes allow the application of a time varying sinusoidal potential to each of the four RW electrode segments in the 2-stage trap (recall the geometry from figure 2.4), with a phase shift of 90° between each successive segment. A maximum of two signals with a phase difference of 90° can be generated by a NF Corporation Wavefactory multifunction synthesiser (WF146B), which are then split and inverted using passive 180° phase splitters for the four necessary sinusoidal signals. To superimpose the AC signals for the RW onto the DC trapping biases, passive high pass filters are used. Further details of the four segment single RW in the 2-stage trap can be found in [Isaac, 2010], where using the RW during positron trapping increased the maximum number of trapped particles by a factor of 7.

4.2 Double Rotating Wall in the 3rd Stage Accumulator

The electrodes in the 3rd stage accumulator were designed to increase the linear z term in the expansion of the RW electric potential and reduce the next significant term, as suggested by [Isaac, 2010; Deller, 2013], as described further in section 4.3.2. This linearity is assumed in the compression model [Isaac *et al.*, 2011; Isaac, 2013], but the single RW potential only provides an approximate match. The single RW potential also contains a non-zero constant offset in $\phi(z)$, shown in section 4.3.2, which may introduce unnecessary heating of a particle cloud. Previous studies at Swansea have investigated the loss of positrons due to single RW heating [Deller, 2013], so quantifying and reducing the aforementioned heating was the motivation for this study.

Two sets of RW electrodes were installed as part of the 3rd stage accumulator (recall the geometry from figure 2.7). These are separated by a central compensation electrode of optimised length and operated with a 180° phase offset between the sinusoidal signals applied to each set, which generates a 'double' rotating wall. This produces an antisymmetric RW electric potential along the z–axis.

Each RW electrode in the 3rd stage accumulator is azimuthally split into six equal segments, as opposed to the more conventional four segments in the 2-stage trap. For a rotating dipole at the centre of the 3rd stage accumulator, six sinusoidal signals must be applied with a phase shift of 60° between each neighbouring segment. No cooling gas was admitted directly into the this accumulator, as it diffused across from the 2-stage trap along a pumping restriction, resulting in $\sim 10^{-6}$ mbar of pressure in the X-3 (the pumping cross immediately upstream from the 3rd stage). More details of the practical implementation of a double RW are given in section 4.8.

4.3 Penning Trap Potential in Cylindrical Coordinates

When describing the electric potential in a Penning trap, it can be advantageous to change from expressing the equations of motion in Cartesian coordinates, as was shown in section 2.9, to cylindrical coordinates, due to the cylindrical symmetry

of the system. The ideal Penning trap electric potential is quadratic along the trap axis. Subject to Laplace's equation, the electric potential of equation 2.7 can be rewritten in cylindrical coordinates, by defining $r^2 = x^2 + y^2$ and substituting ω_z from equation 2.10b, as

$$\phi(r, z) = \frac{\omega_z^2 m}{2q}\left(z^2 - \frac{r^2}{2}\right). \tag{4.2}$$

The motion of a charged particle in the non-relativistic limit is described by the Lorentz force equation, which is equation 2.8. Inserting the electric and magnetic fields, the radial equation of motion is

$$\ddot{\boldsymbol{r}} + \Omega_c \hat{\boldsymbol{z}} \times \dot{\boldsymbol{r}} - \frac{\omega_z^2}{2}\boldsymbol{r} = 0 \tag{4.3}$$

whilst the axial equation of motion, equation 2.9c, is unchanged.

4.3.1 Solution in $\mathbf{V}^{\pm}$ Coordinates

Decoupling of the magnetron and cyclotron motions of a particle in a Penning trap can be performed by a further change of coordinate system. The magnetron and cyclotron motions are separated by the use of two vectors $\mathbf{V}^{\pm}$ defined as

$$\mathbf{V}^{\pm} = \dot{\boldsymbol{r}} - \omega_{\mp} \hat{\boldsymbol{z}} \times \boldsymbol{r}, \tag{4.4}$$

where $\omega_{\pm}$ was defined in equation 2.13. In the literature [Brown and Gabrielse, 1986], the magnetic field lies antiparallel to the trap axis, but the parallel definition is instead chosen here. Calculating the derivative with respect to time gives

$$\dot{\mathbf{V}}^{\pm} = \ddot{\boldsymbol{r}} - \omega_{\mp} \hat{\boldsymbol{z}} \times \dot{\boldsymbol{r}}, \tag{4.5}$$

which allows substitution for $\ddot{\boldsymbol{r}}$ from equation 4.3 giving

$$\dot{\mathbf{V}}^{\pm} = -\left(\Omega_c - \omega_{\mp}\right) \hat{\boldsymbol{z}} \times \dot{\boldsymbol{r}} + \frac{\omega_z^2}{2}\boldsymbol{r}. \tag{4.6}$$

Substituting for $\dot{\boldsymbol{r}}$ from equation 4.4 and using that $\Omega_c - \omega_{\mp} \equiv \omega_{\pm}$ gives

$$\dot{\mathbf{V}}^{\pm} = -\omega_{\pm} \hat{\boldsymbol{z}} \times \left(\mathbf{V}^{\pm} - \omega_{\mp} \hat{\boldsymbol{z}} \times \boldsymbol{r}\right) + \frac{\omega_z^2}{2}\boldsymbol{r}, \tag{4.7}$$

and expanding this gives

$$\dot{\mathbf{V}}^{\pm} = -\omega_{\pm}\hat{\boldsymbol{z}} \times \mathbf{V}^{\pm} + \omega_{\pm}\omega_{\mp}\hat{\boldsymbol{z}} \times (\hat{\boldsymbol{z}} \times \boldsymbol{r}) + \frac{\omega_z^2}{2}\boldsymbol{r}. \tag{4.8}$$

Next, using the vector triple product to expand,

$$\dot{\mathbf{V}}^{\pm} = -\omega_{\pm}\hat{\boldsymbol{z}} \times \mathbf{V}^{\pm} + \omega_{\pm}\omega_{\mp}\left((\hat{\boldsymbol{z}} \cdot \boldsymbol{r})\,\hat{\boldsymbol{z}} - (\hat{\boldsymbol{z}} \cdot \hat{\boldsymbol{z}})\,\boldsymbol{r}\right) + \frac{\omega_z^2}{2}\boldsymbol{r}, \tag{4.9}$$

but $\hat{\boldsymbol{z}}$ and $\mathbf{r}$ are perpendicular, so $\hat{\boldsymbol{z}} \cdot \boldsymbol{r} = 0$ and $\hat{\boldsymbol{z}} \cdot \hat{\boldsymbol{z}} = 1$, making

$$\dot{\mathbf{V}}^{\pm} = -\omega_{\pm}\hat{\boldsymbol{z}} \times \mathbf{V}^{\pm} - \omega_{\pm}\omega_{\mp}\boldsymbol{r} + \frac{\omega_z^2}{2}\boldsymbol{r}. \tag{4.10}$$

From equation 2.13, $\omega_{\pm}\omega_{\mp} \equiv \omega_z^2/2$, and so the last two terms cancel, leaving

$$\dot{\mathbf{V}}^{\pm} = -\omega_{\pm}\hat{\boldsymbol{z}} \times \mathbf{V}^{\pm}. \tag{4.11}$$

This has solutions

$$\mathbf{V}^{\pm} = A^{\pm}\begin{pmatrix} \sin(\omega_{\pm}t - \phi_{\pm}) \\ \cos(\omega_{\pm}t - \phi_{\pm}) \end{pmatrix}, \tag{4.12}$$

where $A^{\pm}$ and $\phi_{\pm}$ are amplitudes and phases, dependent on the initial conditions. Taking the difference of the vectors $\mathbf{V}^{+} - \mathbf{V}^{-}$, and their cross product with $\hat{\boldsymbol{z}}$ gives

$$\boldsymbol{r} = \begin{pmatrix} x \\ y \end{pmatrix} = \frac{\hat{\boldsymbol{z}} \times (\mathbf{V}^{+} - \mathbf{V}^{-})}{\omega_{+} - \omega_{-}}. \tag{4.13}$$

Thus, as was shown in section 2.9 in Cartesian coordinates, the radial motion of a particle is given by a superposition of two rotations about a circle, with angular frequencies: ω_{+} which is the modified cyclotron frequency (ω_c), and ω_{-} which is the magnetron frequency (ω_m).

4.3.2 Single vs Double Rotating Wall Electric Field Potential

The radial and axial motions in an ideal trap are decoupled, but can be coupled by applying a rotating dipole electric field. From equation 4.12, $\mathbf{V}^{\pm}$ resonates at $\omega_{\pm}$, so near ω_z only the magnetron ($\mathbf{V}^{-}$) motion has a significant contribution. Therefore the cyclotron motion can be neglected ($\mathbf{V}^{+} = 0$), which is the so-

called 'guiding centre approximation' [Northrop, 1961], and so one can set $\mathbf{V}^- = (V_x, V_y)$.

The electric potential of an axially asymmetric rotating dipole with frequency ω_r, as produced a single set of RW electrodes (where their centre is not at the centre of the potential well), after introducing an effective distance z_0, is given in Cartesian coordinates by approximately

$$\phi_{r,1} = a\frac{m}{q}(z - z_0)\left(x\cos\left(\omega_r t\right) - y\sin\left(\omega_r t\right)\right), \tag{4.14}$$

near the centre of the trap, where a is the amplitude of the rotating field. Contrastingly, the electric potential due to a double RW, as produced by two sets of RW electrodes offset in phase from each other by 180°, can be written as approximately

$$\phi_{r,2} = a\frac{m}{q}z\left(x\cos\left(\omega_r t\right) - y\sin\left(\omega_r t\right)\right), \tag{4.15}$$

near the centre of the trap. The on-axis single and double RW potentials as a function of z are shown in figure 4.2. The key advantage of the double RW potential, is the region which is linear as a function of z. Previously published work elucidated the mechanism for independent charged particle compression [Isaac *et al.*, 2011; Isaac, 2013], but a rotating dipole from a single RW does not fully match the model parameters. The double RW uses a rotating dipole potential which is antisymmetric about $z = 0$, which in this study is the centre of the 3rd stage accumulator. This is unlike the single RW, in which there is an axial offset of z_0, as the single RW acts only to one side of the trapping potential minimum, causing an asymmetry about $z = 0$. This offset implies that the heating introduced by a RW should be reduced when using the double RW, as the zero value of the rotating potential is also at the minimum of the trapping potential.

The superposition of this double RW potential onto the ideal Penning trap modifies the equations of motion in $\mathbf{V}^{\pm}$ coordinates to

$$\ddot{z} + \omega_z^2 z = -a\left(x\cos\left(\omega_r t\right) - y\sin\left(\omega_r t\right)\right), \tag{4.16}$$

$$\dot{V_x} = \omega_- V_y - az\cos\left(\omega_r t\right), \tag{4.17}$$

and

$$\dot{V_y} = -\omega_- V_x + az\sin\left(\omega_r t\right). \tag{4.18}$$

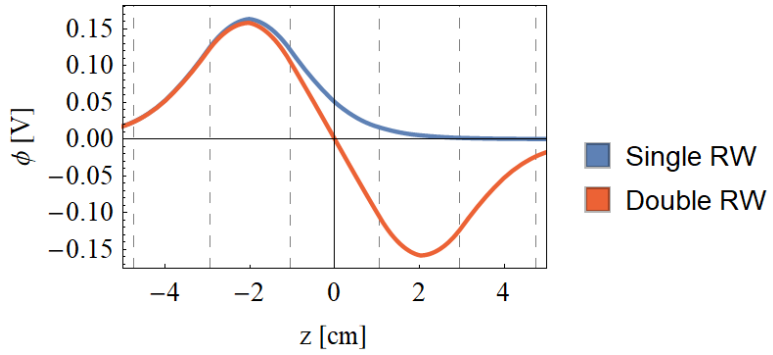

Figure 4.2: Numerical simulation of the on-axis RW potential in the 3rd stage, as a function of axial position, z, where the RW amplitude is set at an arbitrary 0.33 V, which corresponds to the maximum from the function generator. The dashed gridlines denote the edges of the cylindrical electrodes. Blue: $\phi_{r,1}(z)$ for a single RW, where the potential is non-zero at $z = 0$. Red: $\phi_{r,2}(z)$ for a double RW, where the potential is zero at $z = 0$ and there is a longer linear region with a larger effective amplitude, a_{eff}.

4.4 Effective Amplitude Scaling Factor

To compare single and double RW amplitudes, an 'effective amplitude' was introduced, defined as

$$a_{\text{eff}} = \left.\frac{\partial \phi_r}{\partial z}\right|_{z=0}, \tag{4.19}$$

which is the axial gradient of the RW potential at the centre of the accumulator. It has already been shown that the total double RW electric potential is the linear combination of two antisymmetric single RW potentials, $\phi_{r,1a}(z) = \phi_{r,1}(z - z_0)$ and $\phi_{r,1b}(z) = -\phi_{r,1}(z + z_0)$, which produce the double RW potential, $\phi_{r,2}(z) = \phi_{r,1}(z - z_0) - \phi_{r,1}(z + z_0)$, which is an odd function in z, as shown in figure 4.2.

In general, defining two functions $f_1(z) = g(z - z_0)$ and $f_2(z) = -g(z + z_0)$, where $g(z)$ is even and z_0 is a constant, then their linear combination is $f_c = f_1 + f_2 = g(z - z_0) - g(z + z_0)$. Evaluating the derivative with respect to z of f_1 and f_2 at $z = 0$ gives

$$a_{\text{eff1}} = \left.\frac{df_1}{dz}\right|_{z=0} = g'(-z_0) \tag{4.20}$$

and

$$a_{\text{eff2}} = \left.\frac{df_2}{dz}\right|_{z=0} = -g'(z_0). \tag{4.21}$$

Thus, the linear combination of the derivatives is $f_c'(z = 0) = g'(-z_0) - g'(z_0)$.

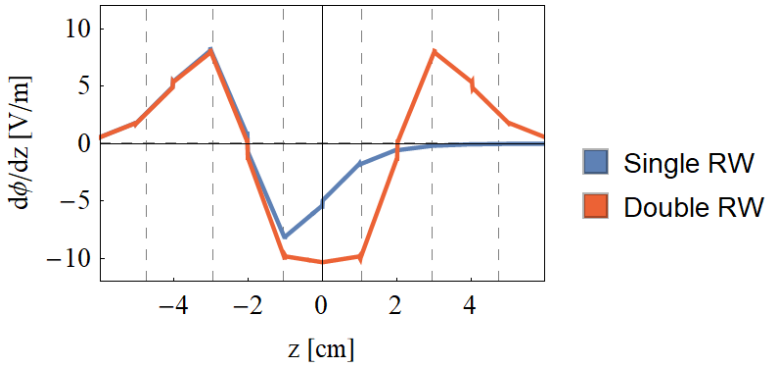

Figure 4.3: Gradient with respect to z of the simulated on-axis potential (from figure 4.2) of the single and double RW at $V_r = 0.33$ V amplitude. (Blue) $\phi'_{r,1}$ for the single RW where $a_{\text{eff1}} = -5$ V/m at $z = 0$. (Red) $\phi'_{r,2}$ for the double RW where $a_{\text{eff2}} = -10$ V/m at $z = 0$, which is double that of the single RW. The longer central potential region of the double RW is displayed, which has a constant gradient. Dashed gridlines denote the edges of the three central cylindrical electrodes in the 3rd stage and discontinuities in the data at the electrode boundaries are only an artefact of the computation.

As $g(z)$ is even, then $g'(z)$ must be odd, making $-g'(z_0) \equiv g'(-z_0)$. This results in the combination, which is the effective amplitude, being

$$a_{\text{effc}} = f'_c(z = 0) = 2g'(-z_0) = 2a_{\text{eff1}} \equiv 2a_{\text{eff2}}. \tag{4.22}$$

So the effective amplitude of the double RW is double the amplitude of a single RW at $z = 0$, and this is independent of radius.

This relation was verified numerically using an arbitrary RW amplitude to calculate the single and double RW potential, $\phi_{r,1}$ and $\phi_{r,2}$ respectively. Then computing $d\phi_r/dz$ specifically for the geometry of the 3rd stage accumulator gives figure 4.3. $\phi'_{r,1}$ for the single RW gives $a_{\text{eff1}} = -5$ V/m and $\phi'_{r,2}$ for the double RW gives $a_{\text{eff2}} = -10$ V/m, which is double the effective amplitude of the single RW, confirming the prediction of equation 4.22. The longer linear central RW potential region (i.e. with constant gradient) is also evident in this plot, which is one of the key differences of the double RW.

4.5 Double Rotating Wall in Cartesian Coordinates

To investigate the behaviour of the double RW when applied near the magnetron frequency, ω_-, consider the equations of motion from equation 2.8 in Cartesian coordinates. After inserting the double RW electric field, the equations of motion are

$$\ddot{x} = \frac{\omega_z^2}{2}x - az\cos(\omega_r t) + \Omega_c \dot{y}, \tag{4.23a}$$

$$\ddot{y} = \frac{\omega_z^2}{2}y + az\sin(\omega_r t) - \Omega_c \dot{x}, \tag{4.23b}$$

$$\ddot{z} = -\omega_z^2 z - a\left(x\cos(\omega_r t) - y\sin(\omega_r t)\right). \tag{4.23c}$$

Transforming into a coordinate system co-rotating with the electric field, where

$$x = \tilde{\xi}\cos\left(\omega_r t\right) + \tilde{\psi}\sin\left(\omega_r t\right), \tag{4.24a}$$

$$y = \tilde{\psi}\cos\left(\omega_r t\right) - \tilde{\xi}\sin\left(\omega_r t\right), \tag{4.24b}$$

then the equations of motion can then be expressed as a set of coupled linear differential equations

$$\ddot{\tilde{\xi}} = \frac{1}{2}\left(2\omega_r^2 - 2\Omega_c\omega_r + \omega_z^2\right)\tilde{\xi} + \left(\Omega_c - 2\omega_r\right)\dot{\tilde{\psi}} - az, \tag{4.25a}$$

$$\ddot{\tilde{\psi}} = \frac{1}{2}\left(2\omega_r^2 - 2\Omega_c\omega_r + \omega_z^2\right)\tilde{\psi} - \left(\Omega_c - 2\omega_r\right)\dot{\tilde{\xi}}, \tag{4.25b}$$

$$\ddot{z} = -a\tilde{\xi} - \omega_z^2 z. \tag{4.25c}$$

Defining

$$b = \frac{1}{2}\left(2\omega_r^2 - 2\Omega_c\omega_r + \omega_z^2\right) \approx -\Omega_c\left(\omega_r - \frac{\omega_r^2}{\Omega_c} - \omega_m\right), \tag{4.26a}$$

$$d = \Omega_c - 2\omega_r, \tag{4.26b}$$

where ω_m is introduced from equation 2.18, allow the differential equations to be recast and denoted in matrix form, $\dot{\mathbf{x}} = \mathcal{M} \cdot \mathbf{x}$, as

$$\begin{bmatrix} \dot{\tilde{\xi}} \\ \dot{\tilde{\psi}} \\ \dot{z} \\ \ddot{\xi} \\ \ddot{\psi} \\ \ddot{z} \end{bmatrix} = \begin{bmatrix} 0 & 0 & 0 & 1 & 0 & 0 \\ 0 & 0 & 0 & 0 & 1 & 0 \\ 0 & 0 & 0 & 0 & 0 & 1 \\ b & 0 & -a & 0 & d & 0 \\ 0 & b & 0 & -d & 0 & 0 \\ -a & 0 & -\omega_z^2 & 0 & 0 & 0 \end{bmatrix} \cdot \begin{bmatrix} \tilde{\xi} \\ \tilde{\psi} \\ z \\ \dot{\tilde{\xi}} \\ \dot{\tilde{\psi}} \\ \dot{z} \end{bmatrix}. \tag{4.27}$$

The matrix $\mathcal{M}$ has eigenvalues given by the characteristic equation

$$a^2\left(b - \lambda^2\right) + \left(\lambda^2 + \omega_z^2\right)\left(b^2 - 2b\lambda^2 + \lambda^2(d^2 + \lambda^2)\right) = 0. \tag{4.28}$$

This characteristic equation is a hexic (sixth order) polynomial in λ. Given that the coefficients of the polynomial are all real, the roots must appear in complex conjugate pairs. These can be expressed in a closed analytic form but in this instance contain an inordinate number of terms. To obtain a simpler approximate solution, a new definition is introduced, $\nu = \lambda^2$, such that

$$a^2(b - \nu) + (b^2 + (d^2 - 2b)\nu + \nu^2)(\nu + \omega_z^2) = 0, \tag{4.29}$$

which has one real root and two non-real complex conjugate roots. As typically $\Omega_c \gg \omega_z \gg \omega_m$, considering roots near ω_m means $\nu \ll \omega_z$ and thus $(\nu + \omega_z^2) \approx \omega_z^2$. As defined in equation 4.26b, $d = \Omega_c - 2\omega_r$, and the RW frequency, ω_r, is on the order of ω_m in the region of interest, thus using the frequency hierarchy, $\omega_r \ll \Omega_c$, then $d \approx \Omega_c$. Substituting for these leaves

$$a^2(b - \nu) + (b^2 + (\Omega_c^2 - 2b)\nu + \nu^2)\omega_z^2 = 0. \tag{4.30}$$

Now introducing a definition $g = a^2/\omega_z^2$, then rearranging gives

$$gb + b^2 + (\Omega_c^2 - 2b - g)\nu + \nu^2 = 0. \tag{4.31}$$

Typically, $a \sim 10^{14}$ s^{-2} [Isaac, 2010] and $\omega_z \sim 10^7$ s^{-1}, so $g \sim 10^{14}$ s^{-2} and $b \sim 10^{14}$ s^{-2}, whilst $\Omega_c^2 \sim 10^{18}$ s^{-1}. Therefore, as $\Omega_c^2 \gg g$ and $2b$, the Ω_c^2 term

dominates the linear term in ν, and

$$gb + b^2 + \Omega_c^2\nu + \nu^2 \approx 0. \tag{4.32}$$

The solutions to the quadratic equation in ν are then

$$\nu_\pm = \frac{-\Omega_c^2 \pm \sqrt{\Omega_c^4 - 4\left(gb + b^2\right)}}{2}. \tag{4.33}$$

Factorising in order to perform an expansion gives

$$\nu_\pm = -\frac{\Omega_c^2}{2}\left(1 \pm \sqrt{1 - \frac{4\left(gb + b^2\right)}{\Omega_c^4}}\right), \tag{4.34}$$

and a Taylor expansion of this expression (using $\sqrt{1-x} \approx 1 - x/2$) gives

$$\nu_\pm \approx -\frac{\Omega_c^2}{2}\left(1 \pm \left(1 - \frac{2\left(gb + b^2\right)}{\Omega_c^4}\right)\right). \tag{4.35}$$

Looking at the definition of b from equation 4.26a for $\omega_r \sim \omega_m$, the second term in b is negligible due to the frequency hierarchy $\Omega_c \gg \omega_m^2$, thus $b \approx -\Omega_c(\omega_r - \omega_m) = -\Omega_c\Delta$, where Δ is introduced as the detuning between the RW frequency and the magnetron frequency. Looking at ν_- by substituting for b and g then gives

$$\nu_- = -\frac{\Omega_c^2\Delta^2 - \Omega_c\Delta a^2/\omega_z^2}{\Omega_c^2}, \tag{4.36}$$

which can be written as

$$\nu_- = \frac{\Delta(-\omega_z^2\Omega_c\Delta + a^2)}{\omega_z^2\Omega_c}. \tag{4.37}$$

As the denominator is real and positive, consider when the numerator is zero, which is when $\Delta = 0$, or

$$\Delta = \frac{a^2}{\omega_z^2\Omega_c}. \tag{4.38}$$

These values correspond to an observed peak in the particle expansion rate when ω_r is between ω_m and $\omega_m + \Delta$, and the full frequency width of the peak is approximately given by Δ. Simulations using the equations of motion show this behaviour in section 4.7.2, which is seen to apply to both the single and double RW, in good

agreement with the approximate expression for Δ derived here. Using this novel expression and measuring Δ experimentally, as a and ω_z are commonly known, also provides a different method to determine Ω_c.

Predicting the RW frequencies at which the magnetron orbit of a trapped particle increases would be useful to avoid ejecting particles when applying a RW, e.g. in a multi-species trap to selectively separate and eject a species, or conversely to avoid ejecting a species while manipulating another.

4.6 Double Rotating Wall General Laplace Solution

By applying appropriate time-varying voltages, a segmented electrode can form a rotating wall electric field to compress clouds of non-neutral particles. A general solution to the Laplace equation for the novel double rotating wall can be derived, as follows.

The electric potential, ϕ, due to two sets of segmented electrodes between two endcap electrodes, as shown in figure 4.4, can be derived by solving Laplace's equation (equation 2.6). In cylindrical coordinates (r,θ,z), the Laplace equation is expressed as

$$\nabla^2\phi = \frac{1}{r}\frac{\partial}{\partial r}\left(r\frac{\partial\phi}{\partial r}\right) + \frac{1}{r^2}\frac{\partial^2\phi}{\partial\theta^2} + \frac{\partial^2\phi}{\partial z^2} = 0. \tag{4.39}$$

This equation can be separated into the product of three ordinary differential equations with respect to each of the three independent variables, r, θ, and z, alone. Using the method of separation of variables, then the solution is $\phi(r,\theta,z) = R(r)\Theta(\theta)Z(z)$. Substituting for ϕ in equation 4.39 and dividing by $R\Theta Z$, yields

$$\frac{1}{R}\frac{1}{r}\frac{d}{dr}\left(r\frac{dR}{dr}\right) + \frac{1}{\Theta}\frac{1}{r^2}\frac{d^2\Theta}{d\theta^2} + \frac{1}{Z}\frac{d^2Z}{dz^2} = 0, \tag{4.40}$$

which are all now ordinary derivatives. As each term is a function of one of the independent variables alone, each term is a constant and their sum must be zero.

As a result of the grounded endcaps shown in figure 4.4, the potential, ϕ, should tend to zero within a finite domain, so we choose a negative real constant

$$\frac{1}{Z}\frac{d^2Z}{dz^2} = -k^2, \tag{4.41}$$

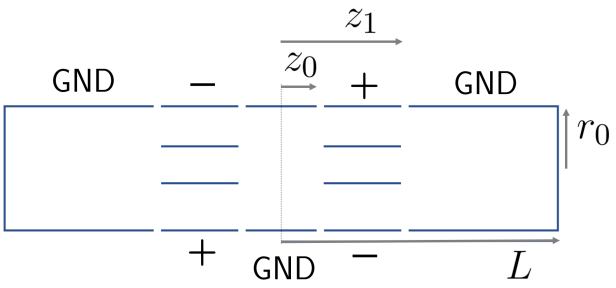

Figure 4.4: Cross section of the central three electrodes along the z-axis with end-caps, not to scale, showing the polarity of the double RW applied biases and defining lengths: z_0, which is half of the centre electrode; and z_1, which is z_0 plus the length of one set of six-segment electrodes. The dotted vertical line denotes where $z = 0$, which is the centre of the electrode stack of length $2L$.

as for the undesirable positive real solution, $+k^2 \to 0$ as $z \to \infty$. The solution for $Z(z)$ is then

$$Z(z) = \begin{cases} \sin(kz) \\ \cos(kz) \end{cases}. \tag{4.42}$$

Replacing the last term in equation 4.40 with $-k^2$ leaves

$$\frac{1}{R}\frac{1}{r}\frac{d}{dr}\left(r\frac{dR}{dr}\right) + \frac{1}{\Theta}\frac{1}{r^2}\frac{d^2\Theta}{d\theta^2} - k^2 = 0. \tag{4.43}$$

We can once again separate this by multiplying by r^2, giving

$$\frac{r}{R}\frac{d}{dr}\left(r\frac{dR}{dr}\right) + \frac{1}{\Theta}\frac{d^2\Theta}{d\theta^2} - k^2r^2 = 0. \tag{4.44}$$

The separated Θ term gives

$$\frac{1}{\Theta}\frac{d^2\Theta}{d\theta^2} = -m^2, \tag{4.45}$$

where the choice of an integer $-m^2$ ensures a periodic solution in θ, where $\Theta(\theta)$ has the solution

$$\Theta(\theta) = \begin{cases} \sin(m\theta) \\ \cos(m\theta) \end{cases}. \tag{4.46}$$

Finally, after substituting $-m^2$ for the second term in equation 2.24, the equation for $R(r)$ which remains is

$$\frac{r}{R}\frac{d}{dr}\left(r\frac{dR}{dr}\right) - \left(m^2 + k^2r^2\right) = 0, \tag{4.47}$$

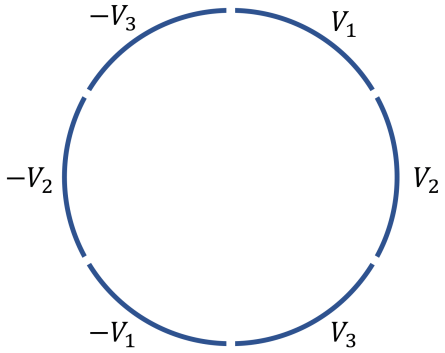

Figure 4.5: Radial cross section of one set of six-segment electrodes, with the applied biases as shown on each segment. There is a phase shift of 60° between each subsequent voltage V_1, V_2 and V_3.

the solution of which are the modified Bessel functions of the first kind of order m, such that

$$R(r) = I_m(kr). \tag{4.48}$$

As the Laplace equation is linear, any linear combination of the solutions is also a solution. The general solution is then

$$\begin{aligned}\phi(r,\theta,z) = \sum_{m=1}^{\infty}\sum_{n=0}^{\infty} I_m(k_n r)\Big(A_{mn}\cos(k_n z) + B_{mn}\sin(k_n z)\Big) \\ \times \Big(a_{mn}\cos(m\theta) + b_{mn}\sin(m\theta)\Big).\end{aligned} \tag{4.49}$$

4.6.1 Boundary Conditions

The general solution in equation 4.49 can be simplified, knowing that the electrodes for which we want to solve the potential have a cross section as shown in figure 4.4. The electrode bounded between z_0 and z_1 has been azimuthally segmented and has voltages applied as shown in figure 4.5, whilst the segmented electrode between $-z_0$ and $-z_1$ has a 180° relative phase offset for the double RW. Due to the symmetry of the system, this makes the potential antisymmetric about $z = 0$, as was shown in figure 4.2. This changes the problem into one where we need only solve for a region bounded by $z = 0$ and $z = L$, both of which are grounded planes, and the potential is defined on the surface of a cylinder $\phi_d(r_0, \theta, z)$, where r_0 is the inner radius of the cylindrical electrodes. We can therefore set $A_{mn} = 0$,

as the potential along z is antisymmetric, and write the solution as

$$\phi(r,\theta,z) = \sum_{m=1}^{\infty}\sum_{n=0}^{\infty} I_m(k_n r) B_{mn} \sin(k_n z)\Big(a_{mn}\cos(m\theta) + b_{mn}\sin(m\theta)\Big), \quad (4.50)$$

with

$$k_n = \frac{n\pi}{L}. \quad (4.51)$$

The boundary conditions on the surface of the cylinder of radius $r = r_0$ can then be defined as the product of only two functions, $f(z)$ and $t(\theta)$, which are defined as follows.

The piecewise function of the applied double RW voltages, $f(z)$, is antisymmetric in z, where

$$f(z) = \begin{cases} -1 & \text{if } -z_1 < z \leq -z_0, \\ 1 & \text{if } \quad z_0 < z \leq z_1, \\ 0 & \text{otherwise.} \end{cases} \quad (4.52)$$

We can determine the Fourier sinusoidal series of the piecewise function $f(z)$, as shown in figure 4.6a, giving

$$f(z) = \sum_{n=0}^{\infty} \beta_n \sin\left(k_n z\right), \quad (4.53)$$

where

$$\begin{aligned} \beta_n =& \frac{1}{L}\int_{-L}^{L} f(z)\sin\left(k_n z\right) \\ =& \frac{2}{k_n L}\left(\cos\left(k_n z_0\right) - \cos\left(k_n z_1\right)\right). \end{aligned} \quad (4.54)$$

This yields

$$f(z) = \sum_{n=0}^{\infty} \frac{2}{k_n L}\left(\cos\left(k_n z_0\right) - \cos\left(k_n z_1\right)\right)\sin\left(k_n z\right), \quad (4.55)$$

and so equating coefficients of $\sin(k_n z)$ with equation 4.49 gives

$$B_{mn} = \frac{2}{k_n L}\frac{\left(\cos\left(k_n z_0\right) - \cos\left(k_n z_1\right)\right)}{I_m(k_n r_0)}. \quad (4.56)$$

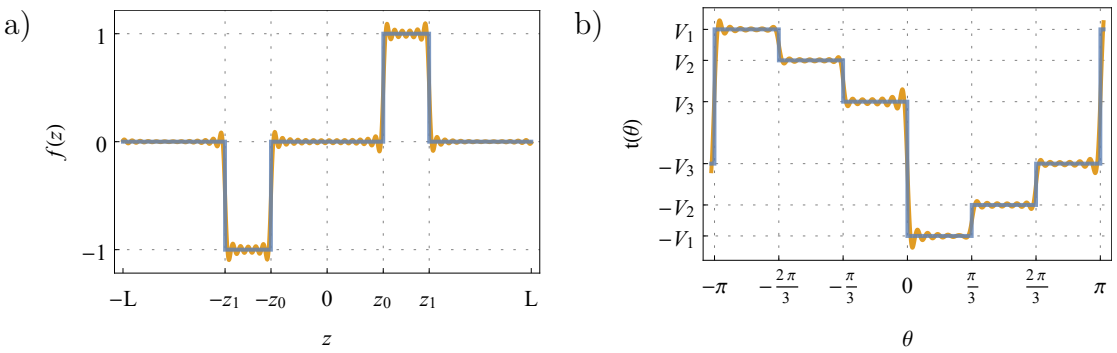

Figure 4.6: Graphical representation of the boundary conditions a) $f(z)$ for the segmented electrode of length $z_1 - z_0$ (blue), with Fourier series truncated at 40 terms (orange). b) $t(\theta)$ for the segmented electrode between $-\pi$ and π (blue), with Fourier series truncated at 40 terms (orange).

Defining the angular boundary conditions for the six-segment electrodes as illustrated in figure 4.5 and 4.6b, then

$$t(\theta) = \begin{cases} V_1 & \text{if} \quad -\pi < \theta \leq -\frac{2\pi}{3}, \\ V_2 & \text{if} \quad -\frac{2\pi}{3} < \theta \leq -\frac{\pi}{3}, \\ V_3 & \text{if} \quad -\frac{\pi}{3} < \theta \leq 0, \\ -V_1 & \text{if} \quad 0 < \theta \leq \frac{\pi}{3}, \\ -V_2 & \text{if} \quad \frac{\pi}{3} < \theta \leq \frac{2\pi}{3}, \\ -V_3 & \text{if} \quad \frac{2\pi}{3} < \theta \leq \pi. \end{cases} \tag{4.57}$$

The Fourier expansion of these piecewise angular boundary conditions is

$$t(\theta) = \sum_{m=1}^{\infty} \left(a_m \cos(m\theta) + b_m \sin(m\theta) \right), \tag{4.58}$$

but the analysis in the radial plane can be completed using the full boundary condition as shown in figure 4.5, which results in

$$a_m = -\frac{1}{m\pi} \left(\sin\left(\frac{m\pi}{3}\right) + \sin\left(\frac{2m\pi}{3}\right) \right) (V_1 - V_3) \tag{4.59}$$

and

$$b_m = -\frac{1}{m\pi} 4 \sin^2\left(\frac{m\pi}{6}\right) \left(2\cos\left(\frac{m\pi}{3}\right) + 1 \right) \left(\cos\left(\frac{m\pi}{3}\right) (V_1 + V_3) + V_2 \right). \tag{4.60}$$

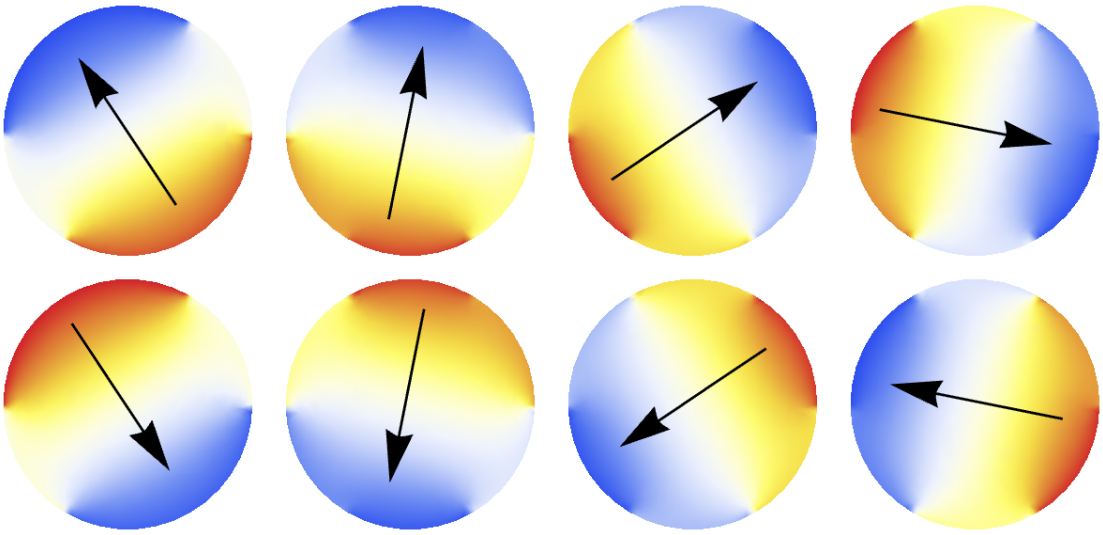

Figure 4.7: (Left to right) The time evolution of the radial cross section of the rotating dipole electric field due to a six-segment electrode, shown using eight images. This shows the potential in the x-y plane where blue represents a lower potential, whilst red represents a higher potential, such that a net zero potential is white. The black arrows show the direction of the electric field. The initial phase is arbitrary and the time step size between each image is $t = 1/(8\omega_r)$.

A simulation of the rotating dipole electric field in the radial plane, as produced by a six-segment RW, is shown in figure 4.7.

4.7 Equations of Motion with Damping

RW studies at Swansea have elucidated the compression mechanism for the single particle regime [Isaac, 2010; Isaac *et al.*, 2011; van der Werf *et al.*, 2012; Isaac, 2013], but this model contains a Stokes' drag term of the form

$$\ddot{\mathbf{s}} = -\frac{q}{mK}\dot{\mathbf{s}} \equiv -\kappa\dot{\mathbf{s}}, \tag{4.61}$$

where K is the particle mobility in the gas at a certain pressure and temperature while $\dot{\mathbf{s}}$ is the particle velocity, as an attempt to account for the rotational and vibrational excitation of the cooling gas. Positron cooling by a gas was modelled as above, but it was shown empirically that the damping parameter, κ, varies with RW amplitude [Isaac, 2010], so this form cannot fully encapsulate the physics of positron-molecule collisions. Therefore, an alternative cooling method following a Stokes' form was sought. Resistive cooling in a harmonic potential well is one

mechanism that provides this desired Stokes' friction term and resultantly offers a more suitable test of the compression model [Isaac, 2013], as is discussed in chapter 5.

The Stokes' term from equation 4.61 applies to each Cartesian direction and so alters the equations of motion from equations 2.9 to

$$\ddot{x} = \frac{\omega_z^2}{2}x + \Omega_c\dot{y} - \kappa\dot{x} \tag{4.62a}$$

$$\ddot{y} = \frac{\omega_z^2}{2}y - \Omega_c\dot{x} - \kappa\dot{y} \tag{4.62b}$$

$$\ddot{z} = -\omega_z^2 z - \kappa\dot{z}. \tag{4.62c}$$

Solving these requires defining $u(t) = x(t) + iy(t)$, which allows the combination of equations 4.62a and 4.62b to give

$$\ddot{u} = \frac{\omega_z^2}{2}u - (\kappa + i\Omega_c)\,\dot{u}. \tag{4.63}$$

The ansatz $u(t) = u\,(0)\,e^{-i\omega t}$ then yields a characteristic equation with roots of

$$\omega_\pm = \frac{1}{2}\Big(\Omega_c \pm F_+ - i\,(\kappa \pm F_-)\,\Big), \tag{4.64}$$

where

$$F_\pm = \frac{1}{\sqrt{2}}\left(\sqrt{\left(\Omega_c^2 - 2\omega_z^2 - \kappa^2\right)^2 + 4\Omega_c^2\kappa^2} \pm \left(\Omega_c^2 - 2\omega_z^2 - \kappa^2\right)\right)^{\frac{1}{2}}. \tag{4.65}$$

By assuming that $\omega_z, \Omega_c \gg \kappa$, the terms with κ^2 are negligible and so $F_+ \approx \sqrt{\Omega_c^2 - 2\omega_z^2}$ and $F_- \approx 0$, thus equation 4.64 simplifies to

$$\omega_\pm \approx \frac{\Omega_c \pm \sqrt{\Omega_c^2 - 2\omega_z^2}}{2}\left(1 - i\frac{\kappa}{\sqrt{\Omega_c^2 - 2\omega_z^2}}\right). \tag{4.66}$$

The full solution is then

$$x = |A_+|\,e^{-\alpha_+}\cos\left(\tilde{\omega}_+ t + \phi_+\right) + |A_-|\,e^{\alpha_-}\cos\left(\tilde{\omega}_- t + \phi_-\right) \tag{4.67a}$$

$$y = |A_+|\,e^{-\alpha_+}\sin\left(\tilde{\omega}_+ t + \phi_+\right) + |A_-|\,e^{\alpha_-}\sin\left(\tilde{\omega}_- t + \phi_-\right), \tag{4.67b}$$

where

$$\alpha_{\pm} = \frac{1}{2}\left(F_{-} \pm \kappa\right) \tag{4.68a}$$

$$\tilde{\omega}_{\pm} = \frac{1}{2}\left(\Omega_c \pm F_{+}\right). \tag{4.68b}$$

The amplitude of the cyclotron motion decays with a time constant α_+, but the loss of energy from the magnetron motion causes an increase in the amplitude with a time constant α_-. Nevertheless, the magnetron motion is usually considered as quasi-stable due to $\alpha_+ \gg \alpha_-$.

The axial part from equation 4.62c has the trivial solution

$$z = A_z e^{-\kappa t}\cos\left(\omega_z t + \phi_z\right), \tag{4.69}$$

which means the damped axial motion is described by a damped harmonic oscillator, as expected.

4.7.1 Compression Model

From an analytic solution to the equations of motion in $\mathbf{V}^{\pm}$ coordinates, i.e. equations 4.16, 4.17 and 4.18, the rate at which particles move to the axis, Γ, due to an applied RW near ω_z in the single particle regime [Isaac *et al.*, 2011; Isaac, 2013] with a Stokes' friction coefficient, κ, is parametrised by

$$\Gamma = \frac{\kappa}{4}\left(1 - \sqrt{\frac{\tilde{\omega}^2}{1+\tilde{\omega}^2}}\right), \tag{4.70}$$

which is a cusp function, with the two definitions

$$\tilde{\omega} = \frac{\omega_r - (\omega_z + \omega_m)}{\delta}, \tag{4.71}$$

and

$$\delta = \frac{a}{\sqrt{(\omega_c - \omega_m)\omega_z}}, \tag{4.72}$$

where a is proportional to the amplitude of the RW as defined in equations 4.14 and 4.15, and δ is a measure of the frequency width. Thus, the compression rate, Γ, is maximal when $\tilde{\omega} = 0$, which is when the RW frequency $\omega_r = \omega_0 = \omega_z + \omega_m$.

By including a constant expansion term, γ, along with the compression rate,

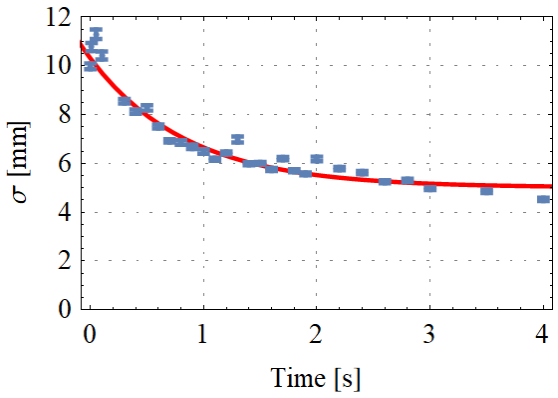

Figure 4.8: Fitted Gaussian width of the cloud, as described in section 2.4.1, plotted against applied double RW time, $\sigma(t)$. The cloud was held in the well for 0.1 s to thermalise prior to application of the RW with $V_r = 20$ mV and $f_r = 10.475$ MHz. The mean and standard error of five repeats is plotted and the red curve is a fit to equation 4.74, giving $\sigma_0 = (10.31 \pm 0.31)$ mm, $\gamma = (5.87 \pm 0.86)$ mm/s and $\Gamma = (1.17 \pm 0.14)$ s^{-1}.

then the temporal change of the radial width of the Gaussian cloud, $\sigma(t)$, is parametrised by

$$\dot{\sigma} = -\Gamma\sigma + \gamma, \tag{4.73}$$

which is a differential equation with the solution

$$\sigma(t) = \left(\sigma_0 - \frac{\gamma}{\Gamma}\right) \exp\left(-\Gamma t\right) + \frac{\gamma}{\Gamma}, \tag{4.74}$$

where σ_0 is the initial width of the cloud.

To measure the compression rate experimentally, the RW is applied for a time t with a frequency f_r and amplitude V_r. When the cloud is ejected, its Gaussian width in the radial plane, σ, is measured by fitting a 2D optical image of the MCP signal. Equation 4.74 can then be fitted to a 'compression curve', which is a plot of measured $\sigma(t)$, an example of which is shown in figure 4.8. These measurements can be repeated for many RW frequencies around $f_z + f_m$, which would allow a plot of $\Gamma(f_r)$ to be fitted with equation 4.70 to obtain quantitative values of κ, f_0 and δ. These measurements are discussed further in section 4.9.2.

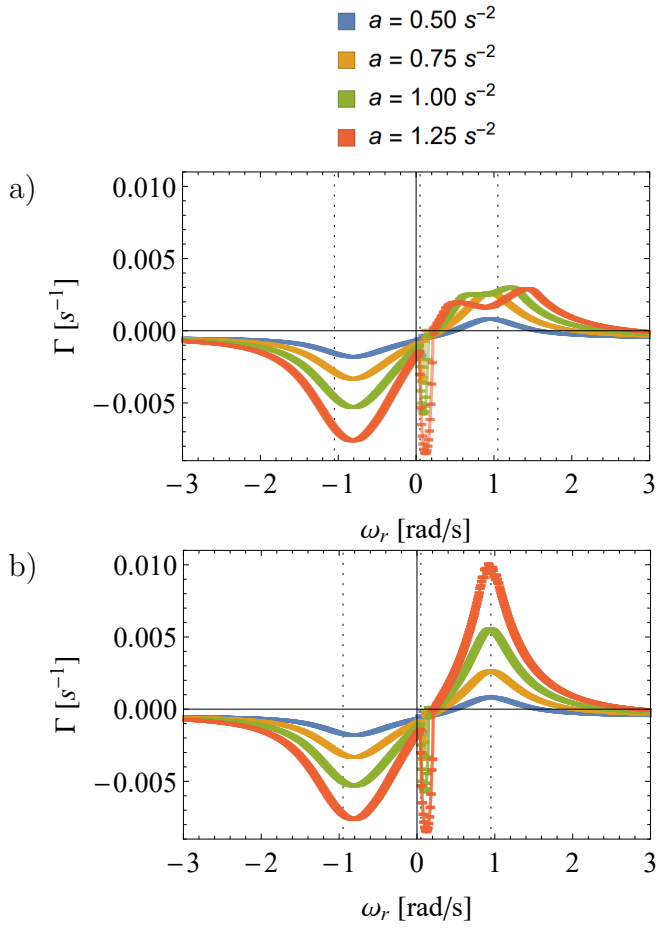

Figure 4.9: a) Numerical simulation of the particle compression rate as a function of single RW frequency. b) Numerical simulation of the particle compression rate as a function of double RW frequency. Data are plotted with fitting uncertainty and joined to guide the eye, with gridlines at $-(\omega_z + \omega_m)$, ω_m and $\omega_z + \omega_m$. The resonant expansion near ω_m (≈ 0.05 rad/s) is shown in more detail in figure 4.11.

4.7.2 Single Particle Motion With Scaled Parameters

Using the equations of motion for a single charged particle including a Stokes' friction term (equations 4.62a, b, and c) along with a single or double RW as described in equation 4.14 or 4.15 respectively, the exponential decrease in particle radius as a function of time quantifies the axialisation rate, Γ, which is the rate at which particles move to the axis. Parameters near unity were chosen to reduce the computational time and investigate differences in general form between the single and double RW, which were not specific to the electrode geometry and potential. Varying a parameter and recognising the qualitative response provided insights for the interpretation of experimental data, as follows.

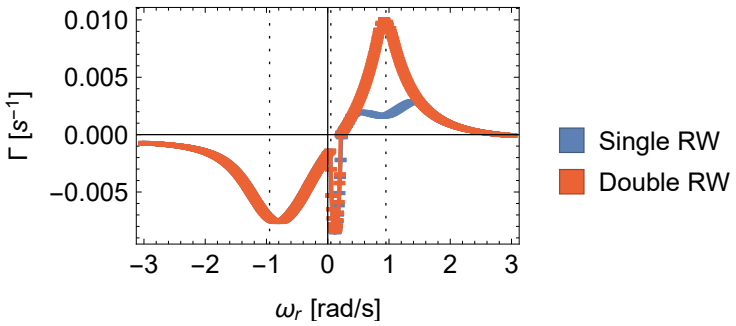

Figure 4.10: Comparison of the numerical simulation of the particle compression rate as a function of single RW frequency (blue) and double RW frequency (red) from figure 4.9 for $\omega_z = 1$ rad/s, $\Omega_c = 10$ rad/s, $\kappa = 1$ s^{-1} and $a = 1.25$ s^{-2} only. The data are plotted with a fitting uncertainty and joined to guide the eye. Gridlines are drawn at $-(\omega_z + \omega_m)$, ω_m and $\omega_z + \omega_m$.

The initial conditions for position and velocity were arbitrarily set to $\mathbf{s} = 1$ m and $\dot{\mathbf{s}} = 1$ ms^{-1} respectively, where times of up to $t = 200$ s were considered, and the input parameters were set as $\omega_z = 1$ rad/s and $\Omega_c = 10$ rad/s, which allowed $\omega_m \approx 0.05$ rad/s to be calculated using equation 2.13. This maintained the physical hierarchy in the motional frequencies. Recall that the key difference in the single RW potential, as compared with the double RW, is the existence of the arbitrary axial offset term, which was set to be $z_0 = 10$ mm.

Plotting $\Gamma(\omega_r)$ for positive and negative values of RW frequency, where by convention the latter corresponds to a RW counter-rotating with the radial particle motion, enables a comparison between single and double RW compression rates. The asymmetry in the simulated single RW resonant compression rate peak at $\omega_r = \omega_z + \omega_m \approx 1$ rad/s in figure 4.9 with $\kappa = 1$ s^{-1} and $a \geq 1$ s^{-2} are a result of the z_0 offset inherent in the single RW. If z_0 is shorter, then the local maxima at $\omega_r \approx 0.5$ rad/s and $\omega_r \approx 1.25$ rad/s both shift closer, towards $\omega_r \approx 1$ rad/s, providing better agreement with the double RW. The double RW potential of equation 4.15 is the limit of $z_0 \to 0$ in the single RW potential of equation 4.14, which was shown algebraically but is also displayed by the simulation. Setting $a = 0.5$ s^{-2} or 1 s^{-2} results in agreement between the compression rates for single and double RW, thus for small amplitudes experimentally, exact agreement may be seen between a single and double RW. Differences become visible as the RW amplitude is increased.

Directly comparing the single and double RW for a single amplitude a, there is only a significant difference near $\omega_r = \omega_z + \omega_m \approx 1$ rad/s, with good agreement

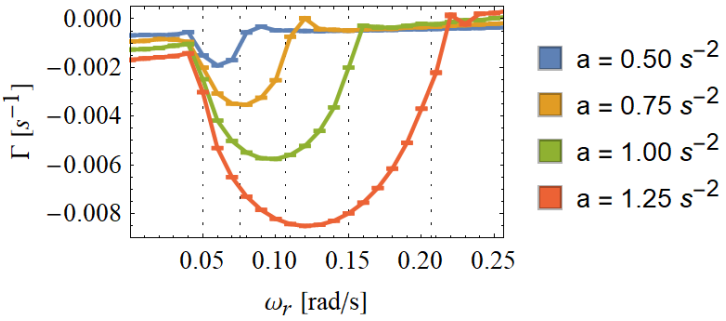

Figure 4.11: Numerical simulation of the particle compression rate as a function of single RW frequency near the magnetron frequency for various amplitudes. The data are plotted with a fitting uncertainty and joined to guide the eye. Gridlines are drawn at ω_m (≈ 0.05 rad/s) and $\omega_m + \Delta(a)$ for each of the four RW amplitudes. This illustrates that the approximations to obtain the expression for $\Delta(a)$ in equation 4.38 are reasonable and predict the frequency range at which a resonant increase in expansion is seen near ω_m. Equivalent results for the double RW are indistinguishable.

seen for all other frequencies. This is illustrated clearly in figure 4.10 where one configuration with $a = 1.25$ s^{-2} has been chosen from the single and double RW from figure 4.9. At this comparatively large amplitude, the maximal compression of the single RW is lower by a factor of ≈ 4 compared with the double RW, and two separate asymmetric peaks are observed.

Looking instead at the resonant expansion near the magnetron frequency, $\omega_r = \omega_m \approx 0.05$ rad/s, which is enlarged in figure 4.11, it can be seen that the frequency at which the particle radius begins to expand is constant at ω_m, and the width of the trough is amplitude dependent and confirms the relationship derived for $\Delta(a)$ in equation 4.38. This allows a prediction for the frequencies near ω_m at which a resonant increase in expansion is seen.

Experimental data obtained from a single RW co-rotating with the radial motion of the particles near ω_m is given in figure 4.12, where a decrease in the number of particles was seen, obtaining $\Delta \approx 40$ kHz. Counter-rotating with the radial particle motion near f_m exhibited slight expansion, as observed by MCP signal images, but no particles were lost (data not shown), thereby supporting the prediction that the expansion rate is much larger when the RW is co-rotating with the particles near f_m. The significant asymmetry in the observed form is not predicted, but investigating the cause would require further experimentation by varying the RW amplitude. Driving the cloud with the comparatively large am-

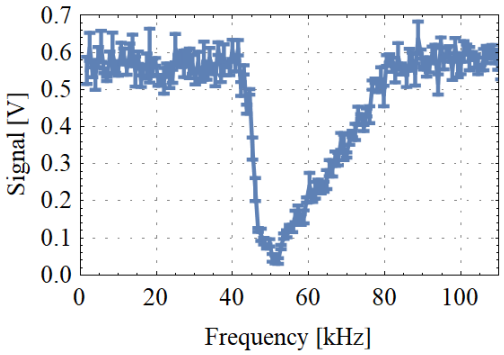

Figure 4.12: Positron number as measured by a CsI detector as a function of single RW frequency (co-rotating with the particles), at $V_r = 3$ V after a 1 s hold in the 3rd stage. Data are plotted with the standard error of four repeats and joined to guide the eye. The positrons were driven at resonance out of the potential well for frequencies near the magnetron frequency of the cloud, giving $\Delta \approx 40$ kHz.

plitude of 3 V may have caused some particles to travel far from the centre of the accumulator leading to a significant deviation in the motional frequencies. This experiment should be repeated with the double RW in order to establish whether the result would be indistinguishable, as predicted by the simulation.

To examine the dependence on the damping constant, κ, the amplitude was fixed at $a = 0.75$ s^{-2}, where agreement was seen between the single and double RW. The simulated results for varying κ are seen in figure 4.13. Agreement is again seen between the single and double RW, except for $\kappa = 0.25$ s^{-1} and 0.50 s^{-1}, where a superimposed trough is again seen on the compression peak at $\omega_r \approx 1$ rad/s. Due to this, the maximal compression is around a factor of 2 smaller for $\kappa = 0.25$ s^{-1}, and a factor of 3 smaller for $\kappa = 0.50$ s^{-1}. Another feature observed here is that by decreasing κ, the resonant frequency of the compression maxima increases and shifts closer to $\omega_z + \omega_m$, and for counter-rotation the frequency of the minimum decreases towards $-(\omega_z + \omega_m)$. Resultantly, $\Gamma_{\max}$ from experiment will occur at $\omega_r \leq \omega_z + \omega_m$, with the magnitude of the frequency shift dependent on the damping constant. This may account for any discrepancy between $f_z + f_r$ and the observed resonant frequency f_0.

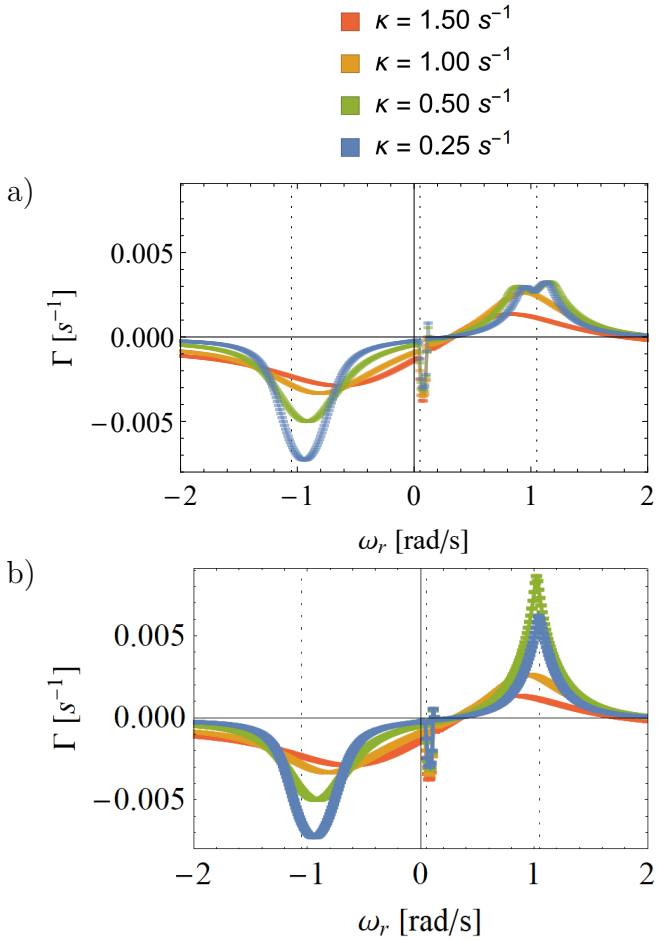

Figure 4.13: a) Numerical simulation of the particle expansion rate as a function of single RW frequency with $a = 0.75$ s^{-2}. b) Numerical simulation of the particle expansion rate as a function of double RW frequency with $a = 0.75$ s^{-2}. Data are plotted with fitting uncertainty and joined to guide the eye, with gridlines at $-(\omega_z + \omega_m)$, ω_m and $\omega_z + \omega_m$. The maximal compression expected at $\omega_r = \omega_z + \omega_m \approx 1$ rad/s for the single RW shows two peaks and is around a factor of 2 smaller for $\kappa = 0.25$ s^{-1}, and a factor of 3 smaller for $\kappa = 0.50$ s^{-1}.

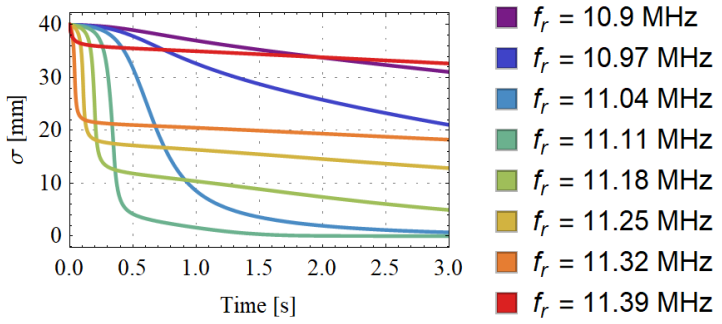

Figure 4.14: Simulated width of the charged particle cloud as a function of time, $\sigma(t)$, when the double RW is applied with amplitude $a = 0.01$ s^{-2} at various frequencies, f_r, around the resonant frequency $f_z + f_m$. The frequencies chosen illustrate the temporal behaviour over the whole frequency range and allows a compression rate, Γ, to be obtained from fitting equation 4.74. A realistic initial cloud width of $\sigma_0 = 40$ mm was chosen.

4.7.3 Simulated Double Rotating Wall Compression Model in a Non-ideal Potential Well

A simulation with realistic input parameters was created for the double RW, using the compression model described in section 4.7.1. From the superposition of the Laplace equation solution for each electrode (chapter 3.2), $f_z(E_\parallel)$ can be computed, and to simulate the time dependence of f_z, an exponential cooling term is introduced to decrease the energy with time,

$$E_\parallel(t) = E_0 \exp\left(-\frac{t}{\tau_c}\right), \tag{4.75}$$

which has a cooling time constant, τ_c. To model the double RW compression, $\dot{\sigma} = -\Gamma\sigma$ was solved, which is a simplification of equation 4.73, when the constant expansion term is negligible ($\gamma \approx 0$ mm/s). This is justified in detail at the end of this section and illustrated by figure 4.17.

Values of a and κ were estimated from previous results of the single RW in the 2-stage trap [Isaac, 2010]. There, the RW amplitude of $V_r = 2$ V resulted in $a \approx 1\ e/m = 1.8 \times 10^{11}$ s^{-2}, thus, as V_r is around 0.02 V here, then $a \approx 0.01\ e/m = 1.8 \times 10^{9}$ s^{-2}. The damping constant, was predicted to be $\kappa \approx 10,000$ s^{-1} in the 2-stage trap, at a gas pressure a factor of 100 larger than the 3rd stage accumulator, so $\kappa \approx 100$ s^{-1} is estimated for the 3rd stage. The free cyclotron frequency is calculated using the calculated magnetic field strength in the

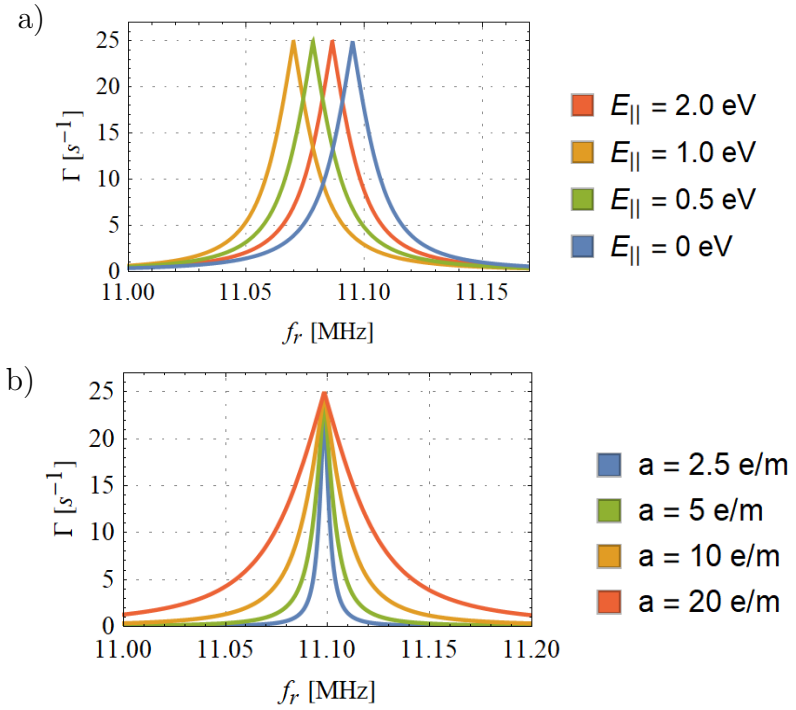

Figure 4.15: Simulated double RW compression rate, as a function of double RW frequency, $\Gamma(f_r)$ with $a = 10\ e/m$. a) Varying particle energy to show the effects of cooling on the frequency of $\Gamma_{\max}$, as $f_z(E_{\|})$. b) Varying RW amplitude with $E_{\|} = 0$, to show its effect on the width of the cusp function.

3rd stage of 37.7 mT, giving $\Omega_c \approx 2\pi \times 2.12$ GHz, and the magnetron frequency is calculated from equation 3.14.

Setting arbitrary values of $E_0 = 5$ eV, $\sigma_0 = 40$ mm, and $\tau_c = 0.5$ s, then plotting the temporal change of the cloud width, $\sigma(t)$, for a range of frequencies around the resonant frequency, $f_0 = f_z + f_m \approx 11.10$ MHz, allows the compression rate, Γ, to be calculated. Simulated examples are given in figure 4.14. The form of $\sigma(t)$ changes as the frequency is increased above resonance. For lower frequencies of $f_r < f_0$, the compression at short times of $t \leq 0.5$ s, is minimal, but then gradually compresses over a timescale of a few seconds. For higher frequencies of $f_r > f_0$, the compression is initially very large but then σ only gradually decreases over the following seconds, forming a near right angle. The changing form of $\sigma(t)$ is a result of $f_z(E_{\|})$, where $E_{\|}$ is a function of time, and the resultant coupling between the RW at f_r and f_0 of the cloud motion near $f_z + f_m$.

Fitting $\sigma(t)$ with equation 4.74 for various RW frequencies, then $\Gamma(f_r)$ can be plotted which gives the cusp function of equation 4.70. This is plotted in figure 4.15a. As the energy decreases, it alters the bounce frequency according to

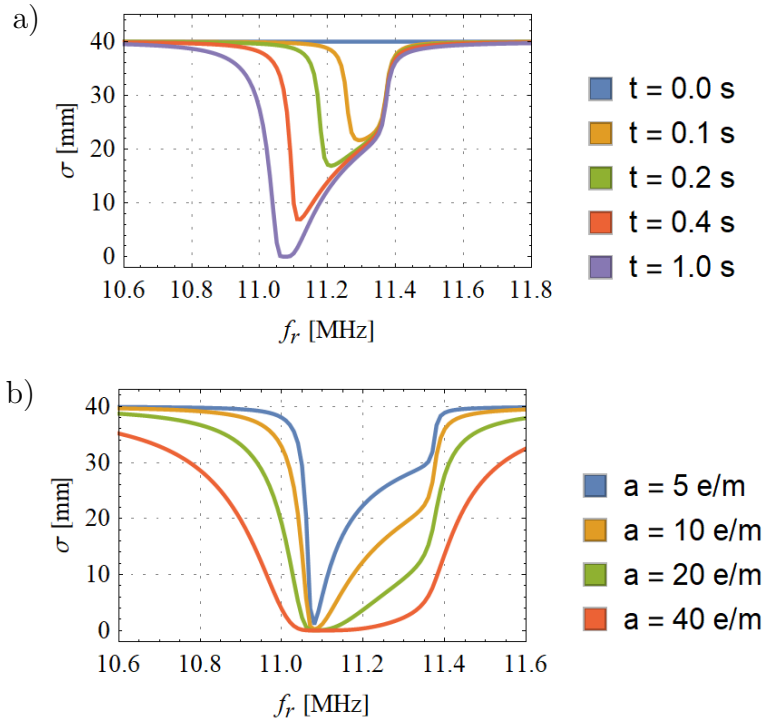

Figure 4.16: Simulated width of the charged particle cloud as a function of double RW frequency, $\sigma(f_r)$. A realistic initial width of $\sigma_0 = 40$ mm was chosen. a) RW applied for various times with $a = 10\ e/m$. b) RW applied at various amplitudes a, with $t = 0.7$ s, showing that the amplitude affects the form of the observed $\sigma(f_r)$.

$f_z(E_\parallel)$, which also causes the resonant frequency to shift. Here, only $E_\parallel$ on-axis is considered, resulting in a form in agreement with anharmonic axial resonances from the literature [Brown and Gabrielse, 1986]. In figure 4.15b, increasing the RW amplitude whilst keeping the energy fixed, results in a wider cusp function, which is as expected from equation 4.70.

Plotting $\sigma(f_r)$ for increasing time gives the form shown in figure 4.16a. The asymmetry stems from the form of $f_z(E_\parallel)$ (recall figure 3.5), as if there was no energy dependence and the potential well was an ideal harmonic, there would be no asymmetry as the frequency of $\Gamma_{\max}$ would not shift with time. For short hold times $t \leq 0.1$ s, $f_z(E_\parallel)$ is linear and so the cooling particle results in a symmetric trough, whereas for $t \geq 0.2$ s, it cools to $E_\parallel \leq 3.5$ eV and an asymmetry begins to be observed.

Increasing the amplitude changes the form of $\sigma(f_r)$, seen in figure 4.16b, causing the trough to appear more symmetric and increasing its frequency width, as

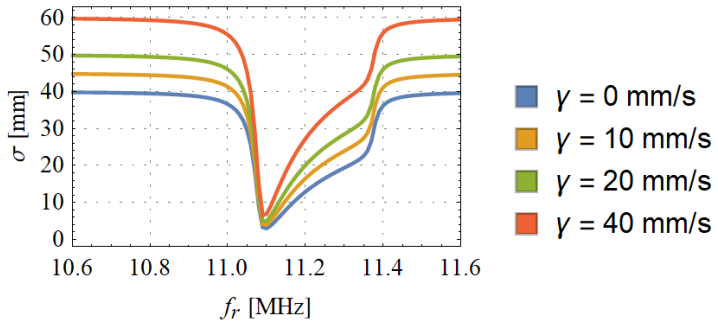

Figure 4.17: Simulated width of the charged particle cloud as a function of double RW frequency, $\sigma(f_r)$, varying the constant expansion term γ. The RW effect was computed using an amplitude $a = 10\ e/m$ for $t = 0.5$ s. A realistic initial width of $\sigma_0 = 40$ mm was chosen.

expected from figure 4.15b. It shows the frequency corresponding to $\sigma_{\min}$ remains constant with increasing amplitude, but that the wings exhibit more compression. One would therefore expect to see a more symmetrical trough in $\sigma(f_r)$ as the RW amplitude is increased.

The value of the expansion term γ should be approximately constant during these studies, as it is primarily dependent upon gas pressure and trap field asymmetries, which both cause expansion in the plasma regime at least [Malmberg and Driscoll, 1980; Notte and Fajans, 1994]. A previously measured experimental value from the 2-stage is $\gamma = (118 \pm 19)$ mm/s [Isaac, 2010], and so scaling according to the gas pressure difference predicted $\gamma \approx 10$ mm/s in the 3rd stage. This was confirmed by the empirical value from figure 4.8, which was $\gamma = (5.87 \pm 0.86)$ mm/s. The effect of γ on the simulated $\sigma(f_r)$ is shown in figure 4.17. The effect of γ on the overall form of $\sigma(f_r)$ is insignificant, as it primarily represents a positive offset in σ. Therefore, an arbitrary choice of $\gamma = 0$ mm/s in the simulated model is justified. It was seen that increasing γ causes a relatively small increase in $\sigma_{\min}$, but a larger offset in the value of σ away from resonance, as in this region there is no compression to counter the expansion term.

4.8 Custom-Built Function Generator

To implement the double RW in the 3rd stage accumulator, a suitable commercial off-the-shelf function generator could not be found. This task required the generation of more than two independent, phase-locked sinusoidal signals at $f > 1$ MHz,

which could be gated. Therefore, a 500 M samples per second direct digital synthesis (DDS) function generator was assembled in-house to implement six-segment rotating wall electric fields on the positron beamline at Swansea University. It uses an AD9959 evaluation board from Analog Devices and the full details of its design and operation are given in appendix A. The rudimentary firmware provided with the AD9959 did not allow modification nor integration with the LabVIEW control system for the beamline, which required a significant undertaking.

The function generator produces up to four phase-locked sinusoidal waves that can be gated by a digital pulse. It was used in this study to implement a six-segment double RW electric field in the 3rd stage accumulator. Three of the function generator outputs were set with a 60° phase difference between each, then 180° passive phase splitters were used to generate the six phase-locked sinusoidal waves with phases of 0°, 60°, 120°, 180°, 240°, and 300° required for each set of RW electrodes. The wiring diagram to appropriately bias the two sets of electrodes is shown in figure 4.18.

High-pass Filters

Two high-pass filter boxes were built for applying the six AC RW signals and the DC trapping voltages. 1 kΩ resistors and 10 nF capacitors gave a comparable time constant to the amplifiers used for the DC voltages, of 10 μs, which resulted in a filter cut-off frequency of $(2\pi RC)^{-1} = 15$ kHz. There were six filters per box with six AC inputs for the RW signals, sharing a common DC for axial trapping. Two filter boxes were built to allow independent control of the DC applied to the upstream and downstream set of RW electrodes, for trapping and ejecting particles.

4.9 Rotating Wall Experimental Data

Experimental results were compared with the numerical simulations in order to gain insights into the RW compression mechanism. In an ideal harmonic potential, the bounce frequency is independent of particle energy. In reality, particles with sufficient energy are able to travel to off-axis anharmonic regions of the accumulator potential, which means these particles will have a different axial bounce frequency, as $f_z(r, E_\parallel)$.

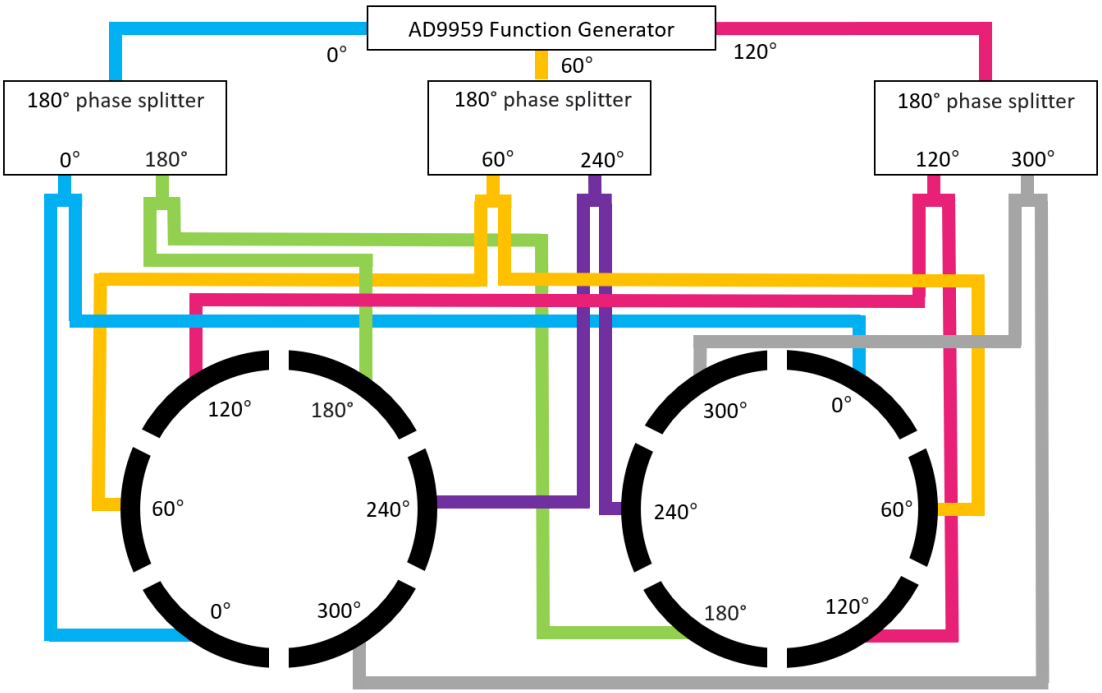

Figure 4.18: Schematic wiring diagram of the set-up to control the two sets of six-segment electrodes for the double RW in the 3rd stage accumulator (shown in black). The phases between the signals applied to equivalent electrodes on each set are 180° out of phase from the other. To assist with clarity, the high-pass filters which apply the RW AC signals to the DC trapping biases for each set of segmented electrodes are not shown, but are located between the phase splitters and the electrode segments.

It was shown that at large RW amplitudes, positrons are lost from trap [Watkeys, 2008], which was attributed to inducing excessive heating. This heating allows energetic particles to travel into less harmonic regions of the potential, causing non-ideal behaviour. It also leads to increased broadening of the frequency response width and an asymmetric form for σ as a function of RW frequency, in agreement with the simulated results of figure 4.16b, due to the energy dependence of the axial bounce frequency. The RW will not couple to energetic particles until they have cooled sufficiently and $f_z + f_m \approx f_r$, as discussed in [Deller *et al.*, 2014].

4.9.1 Rotating Wall Amplitude and Frequency Dependence

To determine the maximum applied RW amplitude in the 3rd stage harmonic potential, frequency scans were performed at various amplitudes, V_r, for both single and double RW.

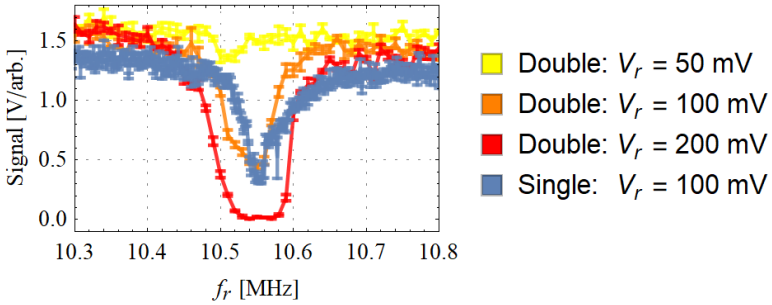

Figure 4.19: Positron number as measured by CsI signal, as a function of RW frequency, for the double and single RW at various applied amplitudes, V_r. The positron cloud was held with an applied RW for 3 s. It can be seen that to avoid losing particles from the 3rd stage, the applied amplitude must be < 50 mV. Differences in signal far from resonance are accounted for by moderator decay between the collection of each dataset, which decreases the number of initially accumulated positrons. The mean and standard error of four repeats are plotted with points joined to guide the eye.

Figure 4.19 shows that for $V_r < 50$ mV (yellow), almost no signal was lost near resonance, therefore this value was identified as the maximum applied RW amplitude. Good agreement was also seen between the frequency at which most particles are ejected for both single and double RW, but the frequency width of the response is more symmetric for the double RW and increases with RW amplitude, as expected. Agreement is also seen for the minimum signal between both single and double RW at $V_r = 100$ mV (blue and orange respectively) of ≈ 0.3 V, although the effective amplitude of the double RW potential is twice as large as the single RW (recall section 4.4). These data suggest that the double RW can be applied with a larger amplitude, a_{eff}, before an equivalent number of particles is lost from the well. Enabling a reduction in the applied double RW amplitude results in increased particle retention, whilst conceivably achieving comparable compression, which is the next topic of investigation.

The resonant frequency, f_0, is predicted from equation 4.70 in the compression model to be independent of RW amplitude, a. This is confirmed by figure 4.20, as the frequency of the local minimum cloud width at $f_r \approx 10.49$ MHz is consistent, within uncertainties, for all amplitudes of both single and double RW. The calculated value of f_0 from the on-axis potential and the B-field (section 3.4) was $f_0 = 11.1$ MHz, but the main cause of the 4.5% discrepancy between the predicted and measured f_0 was discussed in section 3.6, where the radial position of the particles could result in an f_0 between 10.3 MHz and 11.1 MHz. The observed

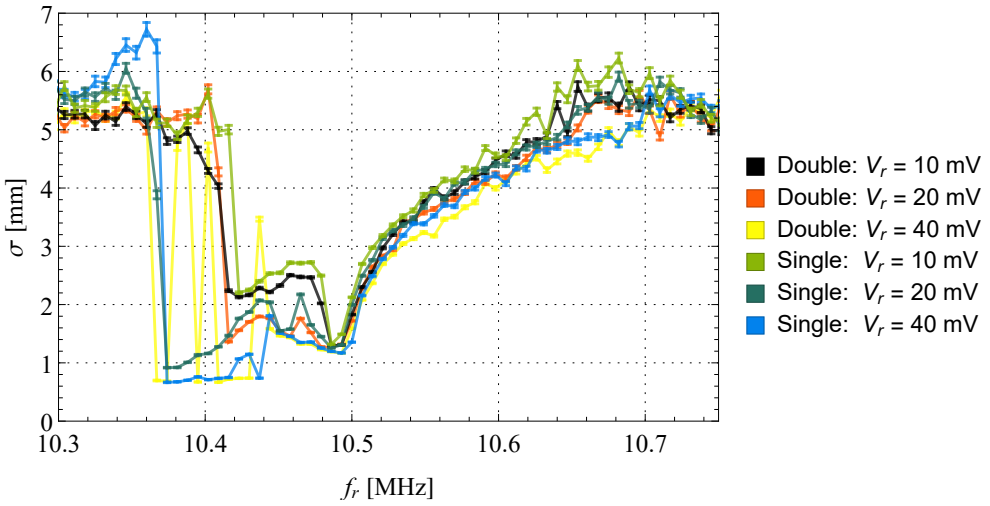

Figure 4.20: Experimental data for fitted Gaussian width of the cloud as a function of RW frequency, $\sigma(f_r)$, for single and double RW at various amplitudes in the 3rd stage. The positron cloud was held for 100 ms prior to applying the RW for 3 s, to ensure equilibration in the harmonic potential. The mean and standard error of five repeats are plotted, where points are joined to guide the eye.

value is therefore in agreement with the theoretical calculations.

Meanwhile, using the empirical values of f_z and f_m from section 3.6 gives $f_0 \approx 10.6$ MHz, and the difference of 110 kHz between it and the measured value of f_0 may also be due to the magnitude of the damping coefficient κ, as discussed in section 4.7.2, where an increasing value for κ decreases the observed resonant frequency from $f_z + f_m$.

The general form of $\sigma(f_r)$ is similar to the equivalent plot from the simulation, which is figure 4.16b. There is a similar asymmetry, where for $f_r > f_0$ a relatively gradual increase in width is seen as frequency increments away from f_0 over an ≈ 200 kHz range. For $f_r < f_0$, the increase in width is larger with decrements in frequency, and at ≈ 150 kHz below f_0, the width has returned to its equilibrium value. The simulation reproduces many of the qualitative features seen in the experimental results, although the relative increase in radius at $f_r \approx 10.46$ MHz may only be expected for a single RW and not a double RW. Figure 4.13 from the simulation for the scaled parameters near unity showed that only one minimum in σ is observed for a simulated double RW, whilst certain configurations of a and κ may cause a double minimum in σ for the single RW. This feature is therefore unexplained for the double RW and a subject of future work, but non-idealities in the 3rd stage which are not considered by the modelling, such as a magnetic field

axis misalignment causing additional harmonics and resonances, may result in the similar features for both RW configurations.

Looking at the smallest amplitudes of $V_r = 10$ mV (green and black), close agreement is seen between single and double RW. When the applied amplitude is increased to $V_r = 20$ mV (dark green and orange), a significant difference is seen between the single and double RW for f_r of 10.34 MHz to 10.42 MHz. $\sigma_{\min}$ for the single RW is seen at 10.37 MHz, as opposed to at $f_r = f_0$ as predicted. The value of $\sigma_{\min}$ is also near the size of two pixels of the CCD detector image, which is 0.7 mm, thus future experiments may benefit from a camera with higher resolution. The largest amplitude of $V_r = 40$ mV causes significant fluctuations in σ for the double RW (yellow), which is not seen for the single RW, but is most likely an effect of the greater difference in effective amplitude.

The population of particles which show compression below $f_r = f_z + f_m$ at larger RW amplitudes can be explained by the form of $f_z(E_\parallel)$ off-axis, from figure 3.5, which predicted that f_0 for each particle may be between 10.3 MHz and 11.1 MHz, dependent upon radial position. Increasing the RW amplitude allows interaction with more of these off-axis particles at larger radial positions, which deviate from the simulated model behaviour of section 4.7.3 and occupy less harmonic regions of the electric potential. A larger V_r also induces additional heating of the particles [Deller *et al.*, 2014], which changes $E_\parallel$ and resultantly f_z, causing an added complication. Further investigation of this feature is the subject of future work.

4.9.2 Rotating Wall Applied Time and Frequency Dependence

Fitting $\sigma(t)$ with equation 4.74 allows compression rates to be obtained. Some examples are given in figure 4.21, showing similar behaviour to the simulated values in figure 4.14. It was seen that for RW frequencies below the resonant frequency of the cloud, $f_r < f_0$, that the compression rate is smaller, whilst near resonance at $f_r = 10.5$ MHz, maximal compression is observed. When the frequency is increased higher, $f_r > f_0$, then there is less compression seen at later times and the compression curve resembles a right angle, akin to the simulation as was discussed in section 4.7.1. The form of the simulated compression curves provide qualitative agreement with the experiment.

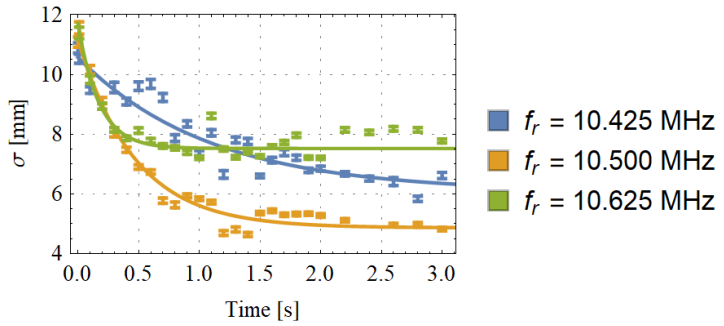

Figure 4.21: Experimental data for fitted Gaussian width of the cloud as a function of double RW time, $\sigma(t)$, in the 3rd stage with $V_r = 20$ mV and three example frequencies. The blue, orange and green data correspond to $f_r < f_0$, $f_r \approx f_0$ and $f_r > f_0$ respectively. The positron cloud was held for 100 ms prior to applying the RW. Plotted are the mean and standard error of five repeats which are fitted with equation 4.74 as a solid line.

Obtaining sufficient data for a reliable fit of $\Gamma(f_r)$ from equation 4.70 was attempted many times, for various single and double RW amplitudes, but were all hampered due to repeated hardware problems. The data acquisition time required around 24 hours worth of data to be collected in one attempt, without a PC or power failure. Successfully performing this experiment would enable a quantitative comparison for values of Γ, alongside enabling κ and δ to be measured. Those values could then be used in the simulation, to better understand the parameters of the compression mechanism.

4.9.3 Rotating Wall Heating

From the single and double RW potentials, it was predicted that the non-zero potential at $z = 0$ for the single RW causes more heating of the charged particles than for an equivalent amplitude with the double RW, whose potential offset is zero. The difference between single and double RW heating of a positron cloud was therefore investigated, where the temperature was measured as described in section 3.9.

For short hold times of $t < 0.5$ s, in the harmonic well, it was seen that the cloud was not yet equilibrated and showed a rapid decrease in $E_{||}$ during this time. This is shown in figure 4.22, where the maximum measured $E_{||}$ of the cloud was used as an example. It was therefore difficult to deconvolve the effect of equilibration, cooling in the well due to background gas, and RW heating during these short

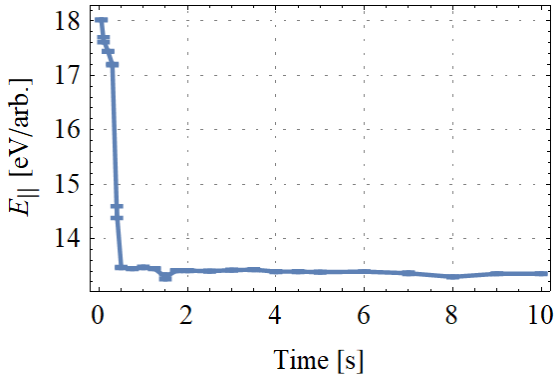

Figure 4.22: Largest parallel energy of the positron cloud against hold time in the harmonic potential in the 3rd stage accumulator, with no RW applied. The mean and standard error of eight repeats are plotted, which are joined to guide the eye. After $t \approx 0.5$ s, the cloud has equilibrated.

times. To overcome this, a 0.5 s hold was introduced prior to applying the RW. This allowed heating from an equilibrium to be observed and comparisons to be drawn between the different RW amplitudes and configurations.

Figure 4.23a shows heating effects due to single and double RW at amplitudes of $V_r = 10$ mV, 20 mV, and 40 mV. Increasing the RW amplitude, V_r, clearly shows an increase in heating for both single and double RW, as expected. After around 5 s, it is notable that the temperature appears to have stabilised at around the same value for each configuration and amplitude, although the corresponding radial width, σ, can be a factor of ≈ 3 smaller. Comparing both $V_r = 40$ mV configurations (green and dark blue), after 5 s the double RW achieved a radial width, σ, which was around half that of the single RW but at the same temperature. The double RW therefore allowed a reduction in the radial width of the positron cloud, without causing a difference in temperature. Relatively good agreement is seen between both configurations for equivalent V_r, but this does not take into account the effective amplitude, a_{eff}. Thus, a_{eff} of the double RW is in fact twice as large as the single RW for the same V_r, but it induces no significant additional heat in the positron cloud. It is therefore more appropriate to compare data at V_r of the double RW with $2V_r$ for the single RW.

A minimum width of $\sigma_{\text{min}} = 0.8$ mm was obtained by the double RW at 40 mV, which is the lowest at the chosen RW frequency, also exhibiting the largest rate of change in σ, which decreased by ≈ 3 mm in 100 ms (between 0.9 s and 1.0 s). The same experimental procedure was performed for frequencies away from $f_z + f_r$,

but the absence of compression resulted in no observed difference in temperatures.

In summary, the novel implementation of a double RW electric field has successfully compressed positron clouds. The data are in broad agreement with the single RW, supporting that double RW mechanism also follows the previously published compression model described in section 4.7.1, as anticipated. It has been shown that a double RW with the same applied amplitude as a single RW induces less heating of a positron cloud, although there was no clear improvement in the absolute minimum radial width attainable at any frequency, at least when applied to present experiments on the Swansea beamline. Work towards further reducing the positron temperature using an external resistive cooling circuit is detailed in the next chapter.

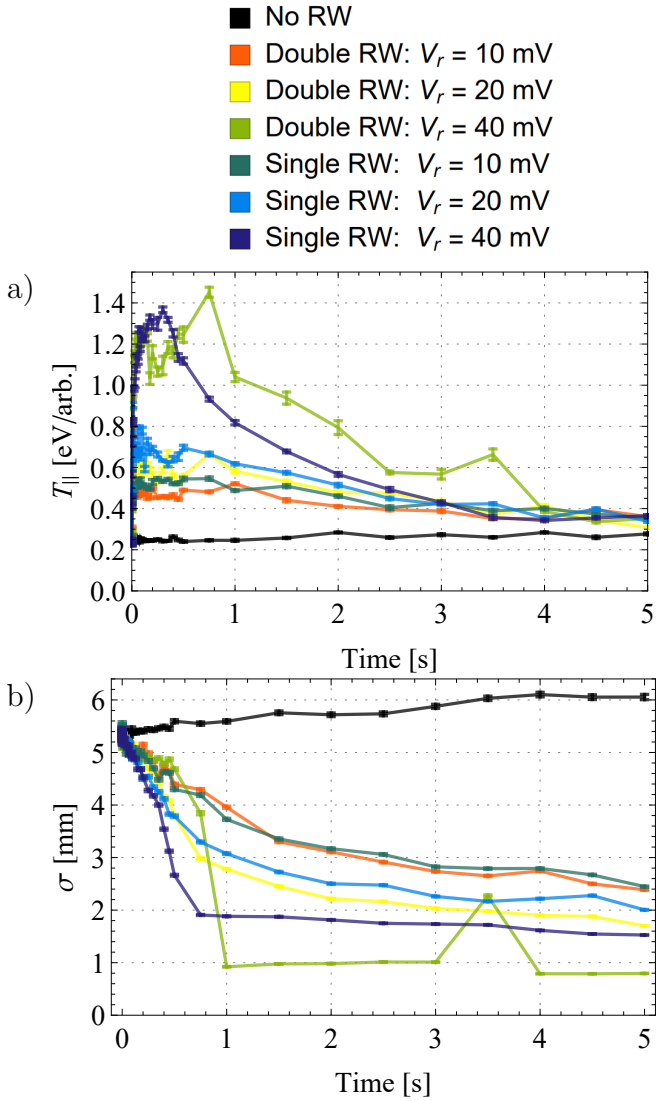

Figure 4.23: a) Temperature as a function of RW time and b) cloud width σ as a function of RW time, for the double and single RW with $f_r = 10.4$ MHz, at amplitudes of 10 mV, 20 mV, and 40 mV, with one dataset which had no RW applied (black). The positron cloud was held for 0.5 s prior to applying the RW, ensuring thermalisation in the harmonic potential. The mean and standard error of eight repeats are plotted, which are joined to guide the eye.

Chapter 5

Towards Resistive Cooling of Positron Clouds

The use of the term 'cooling' in this context corresponds to reducing the kinetic energy of a particle, and an overview of different charged particle cooling techniques is given in many texts, e.g. [Itano *et al.*, 1995]. One technique is resistive cooling, and it occurs when charged particles oscillate near an electrode coupled to an electrical resistance. The particle oscillation induces a varying image charge and as current flows, the ohmic resistance of the circuit dissipates energy and damps the amplitude of the particle motion.

Image currents were studied by Shockley in 1938 and led to the Shockley-Ramo theorem [Shockley, 1938; Ramo, 1939] which allows a calculation of the induced current in a nearby electrode. Resistive cooling has been used for electrons in e.g. [Wineland and Dehmelt, 1975], heavy ions e.g. [Vogel *et al.*, 2014; Ebrahimi *et al.*, 2018], protons e.g. [Ulmer *et al.*, 2013], antiprotons e.g. [Smorra *et al.*, 2017], and single positrons in a hyperbolic Penning trap e.g. [Schwinberg *et al.*, 1981; Haarsma *et al.*, 1995], but not utilised for positron clouds in cylindrical Penning traps. As a result, resistive cooling was not included in a comprehensive review article discussing positron cooling techniques [Danielson *et al.*, 2015].

There is a need to improve antiparticle cooling techniques, as an increase in cooling efficiency would advance many manipulations and their applications [Danielson *et al.*, 2015]. Developing more efficient cooling mechanisms for antiparticles would allow the creation of beams with lower energy and greater energy resolution, and improve the efficiency of the RW technique. Alternate cooling mechanisms could permit reducing the cooling gas pressure, which decreases the antiparticle

annihilation rate and could lead to studying denser non-neutral plasmas. This would also improve the signal-to-noise ratio of the Ps spectroscopy experiments on the Swansea beamline [Deller, 2013]. Therefore, the viability of resistive cooling for positron clouds was investigated.

5.1 Theory

5.1.1 Oscillations Between Parallel Plates

A Single Charged Particle

In the simplest case, one can consider a charged particle of mass m and charge q oscillating at ω_z between two infinite parallel plates, which are separated by a distance of $2z_0$, and connected to a resistor R, as illustrated by figure 5.1. When the particle is at a distance z from the centre, it induces an image charge q', where

$$q' = \frac{(z_0 \pm z)q}{2z_0}, \tag{5.1}$$

then the current flowing through the resistor R, from the Shockley-Ramo theorem is

$$I(t) = \frac{dq'}{dt} = \frac{dq'}{dz}\frac{dz}{dt} = \frac{q}{2z_0}\dot{z}, \tag{5.2}$$

where $\dot{z}$ is the particle velocity. The resistor dissipates a power of $P = I^2R$ through Joule heating and therefore, from $P = dE/dt$, damps the motion by

$$-\frac{dE}{dt} = \langle I^2R \rangle = \frac{q^2\langle \dot{z}^2 \rangle R}{4z_0^2}, \tag{5.3}$$

where the angled brackets denote a time average. For a harmonic potential $\dot{z} = v_{z_0}\cos(\omega_z t)$, where v_{z_0} is the initial z-velocity, then

$$\langle \dot{z}^2 \rangle = v_{z_0}^2\langle \cos^2(\omega_{z_0}t) \rangle = \frac{1}{2}v_{z_0}^2 = \frac{E}{m}, \tag{5.4}$$

in terms of kinetic energy. Substituting for $\langle \dot{z}^2 \rangle$ in equation 5.3 results in

$$-\frac{dE}{dt} = \frac{q^2RE}{4mz_0^2}, \tag{5.5}$$

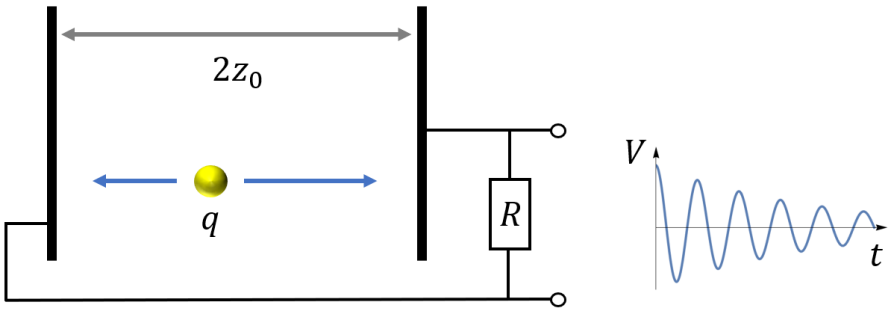

Figure 5.1: A schematic of a charged particle of mass m and charge q oscillating at ω_z between two parallel plates, which are separated by a distance of $2z_0$ and connected to a resistor R. The oscillating charge induces a time-varying image charge which flows through the resistor as an image current, as shown by the plot of $V(t)$.

which gives the damping of the particle energy. The trivial solution to this equation is an exponential decay with a time constant for the 'natural' process of

$$\tau_1 = \frac{4mz_0^2}{q^2 R}. \tag{5.6}$$

So resistive cooling is most effective for particles with a large charge to mass ratio, such as an electron or a positron.

Charged Particle Cloud

For the case where a number N of charged particles are moving with arbitrary phases between two infinite plates, the time averaged total current will be zero, but the mean squared value of the current is non-zero and is given by

$$\langle I_N^2(t)\rangle = \sum_{j=1}^{N} \langle I_j^2(t)\rangle + \sum_{\substack{j,k=1,\\ j\neq k}}^{N} \langle I_j^2(t)\ I_k^2(t)\rangle. \tag{5.7}$$

Let us suppose that the currents due to the j^{th} and k^{th} ion are given by

$$I_{j,k}(t) = \frac{qv_{z_0}}{2z_0}\sin(\omega t + \theta_{j,k}) \tag{5.8}$$

hence the first term in equation 5.7 is

$$\sum_{j=1}^{N}\langle I_j^2(t)\rangle = \frac{q^2 v_{z_0}^2}{4z_0^2}\sum_{j=1}^{N}\langle \sin^2(\omega t+\theta_j)\rangle = \frac{Nq^2 v_{z_0}^2}{8z_0^2}. \tag{5.9}$$

The second term in equation 5.7 is

$$\sum_{\substack{j,k=1,\\ j\neq k}}^{N}\langle I_j^2(t)\ I_k^2(t)\rangle = \frac{q^2 v_{z_0}^2}{4z_0^2}\sum_{\substack{j,k=1,\\ j\neq k}}^{N}\langle \sin(\omega t+\theta_j)\sin(\omega t+\theta_k)\rangle, \tag{5.10}$$

using trigonometric identities, then

$$\sum_{\substack{j,k=1,\\ j\neq k}}^{N}\langle I_j^2(t)\ I_k^2(t)\rangle = \frac{q^2 v_{z_0}^2}{8z_0^2}\sum_{\substack{j,k=1,\\ j\neq k}}^{N}\Big(\langle\cos(\theta_j-\theta_k)\rangle - \langle\cos(2\omega t+\theta_j+\theta_k)\rangle\Big) = 0, \tag{5.11}$$

as the time average of a cosine is zero. So the induced current for N particles is

$$\langle I_N^2(t)\rangle = N\frac{q^2 v_{z_0}^2}{8z_0^2} \equiv N\frac{q^2\langle \dot{z}^2\rangle}{4z_0^2} = N\langle I^2(t)\rangle, \tag{5.12}$$

where $I(t)$ is the single particle current from equation 5.2, so the root-mean-squared induced current for many particles increases with $\sqrt{N}$. The effect of this on the cooling time constant will be detailed in the next section.

5.1.2 Oscillations in a Cylindrical Penning Trap

A Single Charged Particle

In general, the induced current due to a single charged particle's axial motion is given by equation 5.2, but in a cylindrical Penning trap it is modified, such that

$$I(t) = \frac{q}{D}\dot{z}, \tag{5.13}$$

where the effective trap size D is obtained from the electrode geometry. It is given by

$$D = \frac{2z_0}{C_1}, \tag{5.14}$$

close to the trap centre, where C_1 is the first coefficient from the expansion of the trap potential [Vogel, 2018]. Infinite parallel plates separated by a distance $2z_0$

have $C_1 = 1$, such that $D = 2z_0$ and equation 5.13 is equivalent to equation 5.2. Modelling the resistive cooling as a friction force, then using the axial equation of motion with a non-ideal potential, equation 3.9 now becomes

$$\omega_z^2 z - \frac{q}{m}\frac{d\phi}{dz} - \kappa\dot{z} = 0, \tag{5.15}$$

where the cooling rate is κ. For a single particle, the induced current due to the axial motion from equation 5.13 in terms of axial kinetic energy is

$$I(t) = \frac{q}{D}\sqrt{\frac{E_z(t)}{m}}. \tag{5.16}$$

The instantaneous power in a resistive circuit is given by $P(t) = I^2(t)R$, whilst in general, $P(t) = dE/dt$, so equating these two expressions and substituting for $I(t)$ from equation 5.16 gives

$$P(t) = -\frac{dE_z(t)}{dt} = \frac{q^2R}{mD^2}E_z(t). \tag{5.17}$$

Resistive cooling therefore follows an exponential decay of the form

$$E_z(t) = E_z(0)e^{-\kappa t}, \tag{5.18}$$

where $E_z(0)$ is the initial axial energy, with a cooling time constant of

$$\tau_z = \kappa^{-1} = \frac{mD^2}{q^2R}. \tag{5.19}$$

Charged Particle Cloud

For a number N of charged particles moving incoherently in a cylindrical Penning trap, the discussion in section 5.1.1 for parallel plates is still valid, and so equation 5.12 holds for this geometry. The cooling time constant for N particles oscillating with random phases is then again identical to the single particle value τ_1, i.e.

$$\tau_N = \frac{mD^2}{q^2R}. \tag{5.20}$$

Thus, to obtain a small cooling time constant, τ_N, the resistance, R, must be as large as possible.

5.1.3 Non-destructive Particle Detection by a Tuned Circuit

A charged particle induces charges on nearby electrodes, and its motion results in a time-varying signal through an LCR non-destructive detection and cooling circuit [Dehmelt, 1968], which was originally called the 'bolometric technique' [Dehmelt and Walls, 1968]. The inductance is usually supplied by a traditional inductor coil, but a crystal resonator has also been proposed as an alternative, to produce a high quality factor circuit [Kaltenbacher *et al.*, 2011]. From the Shockley-Ramo theorem [Shockley, 1938; Ramo, 1939] (also detailed by a review article [He, 2001]), the induced charge on an electrode j, Q_j, depends on the radial position of the particle by

$$Q_j(\mathbf{r}) = qW_j(\mathbf{r}), \tag{5.21}$$

where $W_j(\mathbf{r})$ is a weighting potential, calculated from the ratio between the potential at $\mathbf{r}$ due to a unit electric potential applied to electrode j, with all other electrodes grounded and charges removed.

The induced current is then given by

$$I_j = q\mathbf{v} \cdot \nabla W_j(\mathbf{r}), \tag{5.22}$$

where $\mathbf{v}$ is the instantaneous particle velocity and $\nabla W_j(\mathbf{r})$ gives the weighting field. The weighting field allows easier calculation of the induced charge, Q, as it is independent of the moving charge. To consider the problem as electrostatic at each moment of charge movement, as above, the Shockley-Ramo theorem assumes that the electric field propagates instantaneously and that magnetic effects are negligible. Such a calculation has been performed for electron plasmas in open-ended cylindrical Penning traps [Di Domizio *et al.*, 2015]. The induced current for harmonically oscillating charged particles will be discussed in the next section.

5.1.4 Tuned Circuit Detection in a Cylindrical Penning Trap

The case of a harmonically confined cloud of charged particles in a cylindrical Penning trap will now be described. For an LCR resistive cooling circuit comprised

of an inductance L, capacitance C and resistance R, the resonant frequency is

$$f_0 = \frac{1}{2\pi\sqrt{LC}}. \tag{5.23}$$

This frequency must be in the neighbourhood of the axial bounce frequency, f_z, for axial cooling to occur, as the ohmic resistance then damps the coupled axial motion. A tuned detection circuit also allows non-destructive diagnostics of particles in equilibrium with the circuit. By measuring the power spectral density, a trough should be seen on the thermal noise signal of the circuit, at the frequency corresponding to the motion of the resonant particle. The trough is a short-circuit due to the particle motion being colder than the temperature of the circuit [Vogel, 2018]. From this measurement, the number of trapped particles can be deduced [Malmberg and Degrassie, 1975; Feng *et al.*, 1996].

Due to the symmetry of the electrodes, the weighting potential W_j only depends on the radial and axial cylindrical coordinates, (r, z). As nearly all the velocity is axial, the expression for the induced current from equation 5.22 can be simplified by neglecting any radial velocity components, giving

$$I_j(t) \approx q\dot{z}\frac{\partial W_j(r,z)}{\partial z}. \tag{5.24}$$

The current induced by the cloud is then the sum of the current induced by each particle.

5.2 Practical Circuit Design Considerations

Simulating the trajectories of confined ensembles, as opposed to single particles, is significantly complicated when considering a frictional force. For realistic results, the interaction of the cooling circuit with the particle ensemble must be included, which is not readily obtained [Vogel, 2018]. For a more accurate prediction of the expected behaviour, experimental non-idealities must be considered.

Thus far, ideal cases have been discussed using theory, but in reality there are practical complications when implementing the cooling circuit. In equation 5.6, it was shown that to decrease the cooling time, a large resistance R is required. This resistance is modified when it is part of a tuned LCR circuit, where an external inductance, L, is used along with the trap capacitance, C. This gives an effective

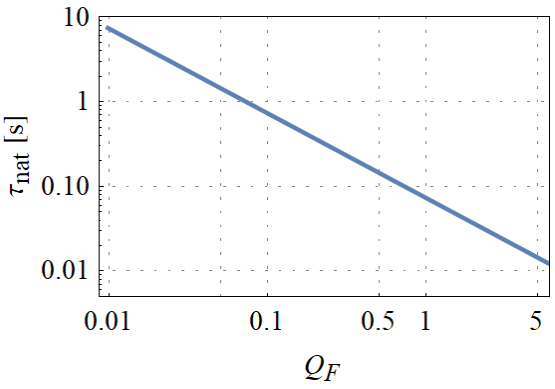

Figure 5.2: Resistive cooling time constant for a positron as a function of circuit quality factor, from equation 5.26. The constants are $z_0 = 38.5$ mm, $U_0 = 1$ V and $C = 1$ nF. To obtain a sufficiently short cooling time, as compared with the positron lifetime which is on the order of tens of seconds, necessitates $\tau_{\text{nat}} \lesssim 1$ s, which requires $Q_F \gtrsim 0.07$. A quality factor of this magnitude should enable the temperature change due to the resistive cooling of positrons to be observed during experiments in the 3rd stage harmonic well.

resistance of $R_{\text{eff}} = Q_F/(\omega_{0_z} C)$, where the quality factor is defined as the ratio of stored to dissipated energy per cycle,

$$Q_F = \frac{f_0}{BW}, \tag{5.25}$$

and BW is the -3 dB bandwidth of the circuit, which allows Q_F to be obtained from a resonance curve. Resistive cooling is effective only within the bandwidth of the external circuit [Winters *et al.*, 2006]. To calculate the exponential cooling natural time constant as a function of quality factor, $\tau_{\text{nat}}(Q_F)$, substituting for R and $\omega_{0_z} = \sqrt{eU/\left(mz_0^2\right)}$ in equation 5.6 gives

$$\tau_{\text{nat}} = \sqrt{\frac{mU_0}{e^3}} \frac{4z_0 C}{Q_F}, \tag{5.26}$$

where U_0 is the height of the confining electric potential. From figure 3.7, the bandwidth of the axial bounce frequency of the positron cloud is < 800 kHz, and a plot of $\tau_{\text{nat}}(Q_F)$ is given in figure 5.2. This shows that provided $Q_F > 0.07$ then $\tau_{\text{nat}} < 1$ s, which is much shorter than the positron lifetime in the 3rd stage accumulator, as desired. Resistive cooling experiments in this set-up are therefore viable. Some cooling is already present due to the diffused cooling gas from the 2-stage. An estimate for the gas cooling time constant, using that the pressure in

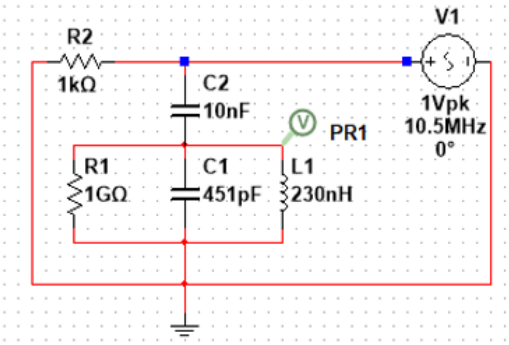

Figure 5.3: High pass filter and resistive cooling circuit diagram drawn in NI Multisim. The parallel LCR resistive cooling circuit has $L = 230$ nH, $C = 451$ pF and $R = 1$ GΩ. Induced positron current is modelled as an AC source with $f = f_z \approx 10.5$ MHz and an arbitrary amplitude of 1 V peak-to-peak. The DC bias on the high pass filter is arbitrarily grounded and 'PR1' denotes the location of the probe which measures the frequency sweep response, to produce a resonance curve as shown in figure 5.4.

the 3rd stage is $\sim 10\times$ lower than the 2-stage and scaling linearly, gives $\tau_{\text{gas}} \sim 10$ s.

The quality factor of a parallel LCR circuit can also be expressed in terms of the electrical components [Pozar, 2011], as $Q_F = 2\pi f_0 RC$, thus for a short cooling time, the resistor and capacitor should be as large as possible. A constraint on the capacitance comes from the resonant frequency of an LCR circuit from equation 5.23. This resonant frequency must be as close as possible to the axial bounce frequency of the cloud, $f_z \approx 10.5$ MHz, for maximal cooling. Thus the capacitance must be large, whilst the inductance is as small as possible, keeping $f_0 \approx 10.5$ MHz. A limiting factor is the inductance of an RG-58 BNC cable, which is used to connect the circuit and is around 340 nH/m, with a capacitance of 100 pF/m [Shi and Kanoun, 2015], thus the minimum inductance was set at the nearest purchasable inductor value of 230 nH (Bourns 9230-04-RC), as measured by a Wayne Kerr 4300 LCR meter. As the parasitic capacitance of each electrode was measured to be around 180 pF, the capacitance of the circuit was chosen as large as possible to dominate over this, whilst keeping f_0 at the desired frequency, thus a capacitor with a measured value of 451 pF was chosen.

The quality factor in a real detection system is affected by the coupling with external circuitry [Pozar, 2011], which lowers the ideal resonator quality factor to

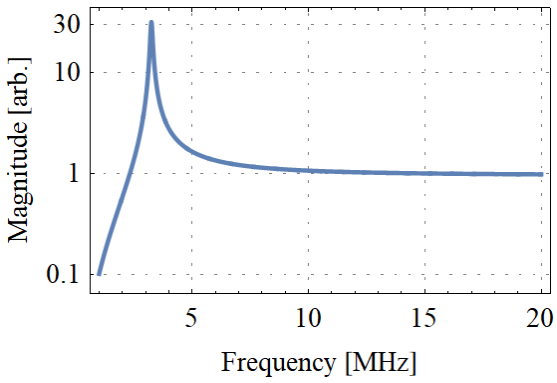

Figure 5.4: Simulated frequency sweep to obtain a resonance curve for the resistive cooling circuit model in NI Multisim. From the simulation, $f_0 = 3.246$ MHz and $BW = 45$ kHz giving $Q_F = 72$, but the parasitic capacitances of the real physical system and its connections were found to cause a shift to $f_0 \approx 11$ MHz and a significant increase in the bandwidth.

an overall 'loaded' quality factor of Q_L, where

$$\frac{1}{Q_L} = \frac{1}{Q_{\text{Resonator}}} + \frac{1}{Q_{\text{Electrode}}} + \frac{1}{Q_{\text{Connectors}}} + \frac{1}{Q_{\text{Amplifier}}} + \dots \tag{5.27}$$

is the inverse sum for all the detection components. In more sophisticated detection systems there may be more components which require consideration [Vogel, 2018]. Therefore, to maximise Q_L for a detectably strong signal, the resonator should be as close as possible to the 3rd stage accumulator pickup electrode. It is also clear that Q_L may be severely limited by only one small quality factor in the chain of detection components. First, considering only $Q_{\text{Inductor}} = 33$ from the inductor datasheet maximum, this limits $Q_L \leq 33$, and accounting for the other components will only decrease this value. The final temperature of a resistively cooled ion is also limited by the temperature of the cooling circuit [Werth *et al.*, 2009], which in this case is room temperature, but if further cooling is required, can be kept in liquid helium, e.g. [Ebrahimi *et al.*, 2018].

A resistive cooling model circuit was built in NI Multisim software, and is shown in figure 5.3. Using the software, a simulated frequency sweep was performed on the circuit and resonance curve obtained, seen in figure 5.4, which predicted $f_0 \approx 3$ MHz. Initially the model was set such that $f_0 \approx f_z \approx 10.5$ MHz, but upon connecting the circuit to the system, there was a significant increase of a few MHz in the resonant frequency, most likely caused by unaccounted parasitic capacitances. Therefore, the values shown in figure 5.3 were chosen, as they gave

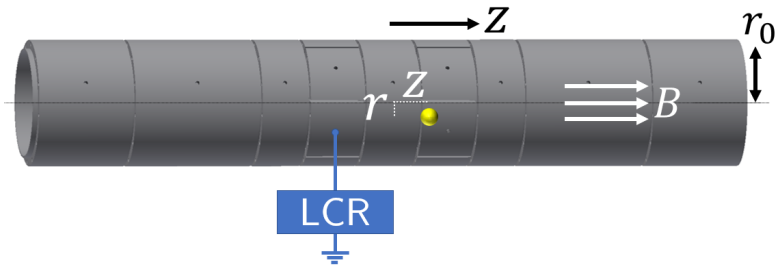

Figure 5.5: Schematic of the 3rd stage cylindrical Penning trap with the LCR resistive cooling circuit connected to an electrode, where the applied static bias is not shown. A positron cloud is shown as a yellow sphere at (r,z) in cylindrical coordinates, not to scale.

an experimental f_0 which was near $f_z \approx 10.5$ MHz.

5.3 Resistive Cooling Experiments

The LCR circuit was connected directly onto the BNC breakout box from the 3rd stage accumulator electrodes, as to minimise parasitic capacitances. A schematic diagram of the setup is shown in figure 5.5. The circuit, connected to a Tektronix RSA 3303A spectrum analyser, successfully detected RW signals from the 2-stage and the 3rd stage at 9.3 MHz and 10.5 MHz respectively. Applying white noise from a function generator to the circuit gave the resonance curve shown in figure 5.6, where the bandwidth was significantly broader than from the simulation, showing that the model did not account for some non-idealities. The resonant frequency was $f_0 = 14.2$ MHz, and the -3 dB bandwidth $BW = 9.8$ MHz, so substituting these values into equation 5.25, gave $Q_F = 1.44$. This value of Q_F corresponds to $\tau_{\text{nat}} = 50$ ms, from figure 5.2, which was sufficiently short to enable the observation of a temperature difference on the timescale of the temperature measurements (~ 5 s).

A low-noise preamplifier was used to amplify the detected signal from the LCR circuit, but no positron image current was observed. By varying the potential applied to the centre electrode, the axial bounce frequency was scanned, to test whether the positron signal then became resonant with the circuit, but no signal was observed. The centre of the trapping potential was also shifted off-centre to attempt detection using the longer centre electrode which should have resulted in a larger signal, but this was also unsuccessful. To obtain high sensitivity, the

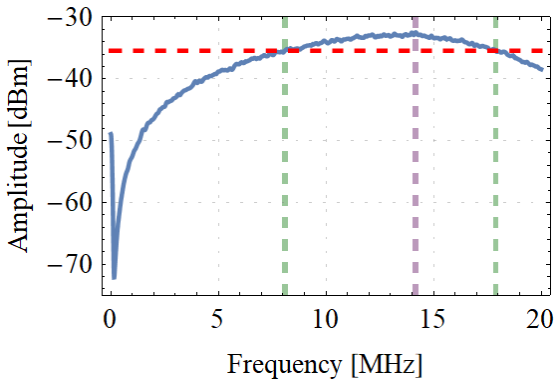

Figure 5.6: Experimental resonance curve, where the signal amplitude as a function of frequency was measured by a spectrum analyser. The resistive cooling circuit was connected to a white noise source, disconnected from the system, with the DC input grounded. The resonant frequency $f_0 = 14.2$ MHz is denoted by a purple dashed gridline, and the -3 dB bandwidth, BW $= 9.8$ MHz, is shown by green dashed gridlines. Substituting these values into equation 5.25, gives $Q_F = 1.44$ (to 2 decimal places).

thermal noise power of the circuit should be kept as low as possible [Werth *et al.*, 2009], and in this instance was kept at room temperature. The temperature of the laboratory was around $T \approx 300$ K, corresponding to 25.9 meV, which was therefore the lowest temperature attainable by resistive cooling in this configuration, and was around a factor of ~ 10 smaller than the measured positron temperature at equilibrium, shown in blue in figure 5.7. This temperature difference should not have prevented resistive cooling from being observed.

Although no positron image current was detected, it was nevertheless possible that resistive cooling was occurring, and so the temperature, as described in section 3.9, was monitored. The temperature was measured with and without the cooling circuit, but no difference was observed. When applying a single RW in the 3rd stage on the set of segmented electrodes downstream, with the cooling circuit connected to the segmented electrode set on the other side of the 3rd stage (upstream), a temperature difference was seen, albeit an increase, as shown in figure 5.7. As the RW was applied near f_z, this heating is attributed to the RW coupling to the LCR circuit and driving the motion of the cloud, instead of damping as intended. The interaction shows that the natural frequency of the LCR circuit was tuned near the correct range, and that parasitically picking up the (relatively large) RW signal was enough to affect the detected positron cloud temperature. This suggests that although f_0 and f_z were aligned, the image cur-

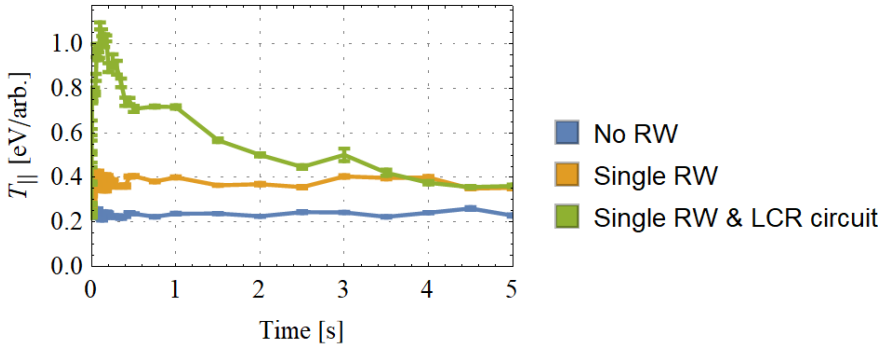

Figure 5.7: Plot of temperature as a function of hold time in the 3rd stage harmonic well after a 0.5 s initial hold for thermalisation, with: no RW (blue), single RW with $V_r = 300$ mV and $f_r = 10.2$ MHz (yellow), single RW with $V_r = 40$ mV and $f_r = 10.4$ MHz and the LCR resistive 'cooling' circuit connected (green). Significant positron cloud heating was observed when the rotating wall was applied with the LCR circuit connected. No temperature difference was seen when the LCR circuit was connected/disconnected with no RW. The mean and standard error of eight repeats are plotted and points are joined to guide the eye.

rent was too small to couple with the circuit and change the detected temperature in this configuration.

Chapter 6

Conclusions

> "Doing science means coming up hard against the limits of your ignorance on a daily basis – the innumerable things which you don't know, and can't do ... A scientist is someone who lives immursed in the awareness of our deep ignorance, in direct contact with our own innumerable limits, with the limits of our understanding."
>
> Carlo Rovelli [2018]

6.1 Summary

A harmonic potential well in the 3rd stage accumulator, with an electrostatic minimum near to the incoming parallel energy has been determined, implemented and characterised, as suggested by [Savage, 2019]. Optimisations to the particle ejection and recapture techniques increased the positron lifetime from around 50 ms to over 60 s, which is a significant improvement, allowing time to study RW and cooling techniques.

This work has built and implemented a function generator that can operate a single and double RW on four, six, and eight-segment electrodes. Applying a double RW in the 3rd stage allows a closer match to the electric fields in the single particle compression model [Isaac, 2013]. Enabling a RW in the 3rd stage accumulator also allows a further increase to the positron lifetime, which is particularly advantageous with long anharmonic potentials wells which are used for other applications, such as positron cloud 'stacking', which allows the study of non-neutral plasmas. A larger number of positrons, compressible by a RW, will

also improve the signal-to-noise ratio of the Ps spectroscopy studies, as identified by [Deller, 2013].

Further understanding the heating process caused by a RW might allow a reduction in the minimum attainable cloud width. A single-shot temperature measurement model has been justified and presented. The temperature measurement method has been reported on the system for the first time and will provide new insights into how manipulations affect the energy distribution.

A simulation of the RW compression model was developed, incorporating an exponential cooling term, which can be compared with experimental results and used for predictions. By obtaining experimental values for the model parameters, the simulation can be further improved. Incorporating further non-ideal features, as observed empirically, will aid in further understanding the mechanism for single particle compression.

The approximate RW frequency range near ω_m where expansion is seen, Δ, can now be predicted, knowing a, ω_z, and Ω_c. By measuring Δ experimentally, a different method for determining Ω_c has also been identified. Predicting the RW frequency range for radial expansion of charged particles may be important, e.g. in a multi-species trap where a particle species could be manipulated without ejecting another, or to purposely eject one species only.

Circuit design and testing has been performed to attempt image current measurements of the axial motion, and although unsuccessful, work has been performed towards realising the first resistive cooling of positron clouds. Obtaining a cooling mechanism which follows a Stokes' viscous drag term was a goal identified by [Isaac, 2010], to allow a more precise test of the compression model and remains a future goal.

6.2 Future Work

During this work, a relatively long electrode which may be used as an accelerator was installed below the MCP in X-4 (immediately downstream from the 3rd stage accumulator). This will allow retarding potential analysis measurements after ejecting particles from the 3rd stage, as opposed to leaving a barrier electrode raised. Experiments retarding positrons by biasing a metal grid upstream from the MCP did not follow the expected form and were disregarded, so using a cylindrical electrode instead would provide direct comparison with cloud energies from the 2-

stage trap. Doing so allows the effect of manipulations on the energy distribution of the particles to be quantified and compared.

Compression and expansion due to a rotating wall was measured but obtaining an estimate for the damping coefficient κ is difficult. Obtaining enough data for a reliable fit from $\Gamma(f_r)$ is not straightforward, as many unsuccessful attempts to collect a complete dataset for the single and double RW were performed but repeatedly failed due to hardware issues. These studies should be repeated to quantify κ, δ, and f_0, but another method to determine κ could also be used, as follows. A systematic study varying gas pressure and measuring the radial expansion of the cloud would give $\kappa(P)$, to better understand the expansion term. It would also allow more realistic parameters to be chosen for simulating the behaviour.

As the magnitude of the RW frequency response width near ω_m, Δ, is predicted to scale linearly with amplitude, a, from equation 4.72, this relationship should be experimentally verified. It could be achieved by varying the amplitude and measuring the frequency width where the expansion rate increases and leads to particle loss. These data should also be collected for the double RW to verify whether the results would be indistinguishable from the single RW, as the simulation in section 4.7.2 forecasted.

Unpredicted behaviour was seen in section 4.9 for RW frequencies below $f_z + f_m$, where a double minimum in cloud width was seen. The experiment could be repeated with smaller RW frequency increments and more amplitudes, for a more comprehensive comparison. Some suggestion of its source was given, but further work is required to probe and understand its origin.

The double RW could be used in the 3rd stage accumulator with electrons, as the number of particles can be significantly increased and may form a plasma. An electron gun allows the number of electrons to be nearly arbitrarily chosen and their kinetic energy controlled. The interaction with the double RW may change in a different particle number or energy regime, leading to new insights. Monitoring the fraction of the cloud which remains linear during the temperature measurement, may indicate when plasma effects become important. Experiments monitoring this fraction whilst increasing the particle number may be of interest to identify the onset of significant plasma effects.

Realising a function generator capable of controlling a six-segment RW electrode has enabled a rotating quadrupole electric field to be implemented, as op-

posed to the rotating dipole used in this work. This has advantages, at least in the plasma regime, as it can control single species plasmas, in contrast to the dipole field [Hasegawa *et al.*, 2005]. A double RW quadrupole electric field can also now be performed, which has not previously been studied.

Installing a pre-amplifier inside the vacuum system would enable low-noise amplification of the image current signals, without amplifying the thermal noise from the external wiring, connectors, and BNC cables of the 3rd stage accumulator. This would also assist with live non-destructive diagnostics, as the magnetron and axial bounce frequencies could be monitored and the RW frequency chirped to track shifts in the cloud frequencies as described in chapter 4. Live RW frequency tuning could minimise the radius of the cloud and keep the particle loss to a minimum, which is particularly advantageous when stacking particles where the hold time may be many seconds.

To identify whether resistive cooling of positron clouds is attainable in the current system, a large number of electrons could be used instead. This would indicate whether the electrode geometry allows such a measurement with a realistic signal, and confirm whether the image charge was too small to couple with the circuit. If this is unsuccessful, then an inductor with a larger quality factor could be used.

Implementing resistive cooling in the 2-stage trap would decrease the need for cooling gas, which is a major source of trapped particle loss. Buffer gas free positron trapping has been demonstrated in a hyperbolic Penning trap using multiple electrodes [Haarsma *et al.*, 1995], and with negative feedback [Schwinberg *et al.*, 1981]. Active negative feedback, by amplifying the detected image current and applying it with opposite phase to an opposite electrode, allows a reduction in the cooling time constant and final temperature as compared to the passive case [Dehmelt *et al.*, 1986]. Achieving resistive cooling with negative feedback could realise lower temperatures for charged particle clouds and plasmas, to enable larger numbers of trapped particles.

Appendix A

Custom-built AD9959 Function Generator

> "We are all in the depths of a cave, chained by our ignorance, by our prejudices, and our weak senses reveal to us only shadows. If we try to see further, we are confused: we are unaccustomed. But we try. This is science. Scientific thinking explores and redraws the world, gradually offering us better and better images of it, teaching us to think in ever more effective ways."
>
> Carlo Rovelli [2018]

To generate more than two synchronised sinusoidal signals at > 1 MHz in burst mode, a new function generator was assembled in-house. The AD9959 evaluation board from Analog Devices (figure A.1) has four DDS cores which share a common clock, so they are inherently synchronised. DDS devices offer fine frequency resolution and fast switching between output frequencies, as they generate a time varying digital signal prior to a 10-bit digital-to-analog conversion (DAC) here. Each of the four channels also has a phase offset for setting their relative phases. It is capable of outputting sinusoidal waves with a frequency of up to 200 MHz and a tuning resolution of 0.12 Hz.

The outputs from the device are set such that all channels can be enabled or disabled simultaneously by a single trigger on one input. Using amplifiers, the maximum amplitude produced around 10 MHz is 6.72 V peak-to-peak.

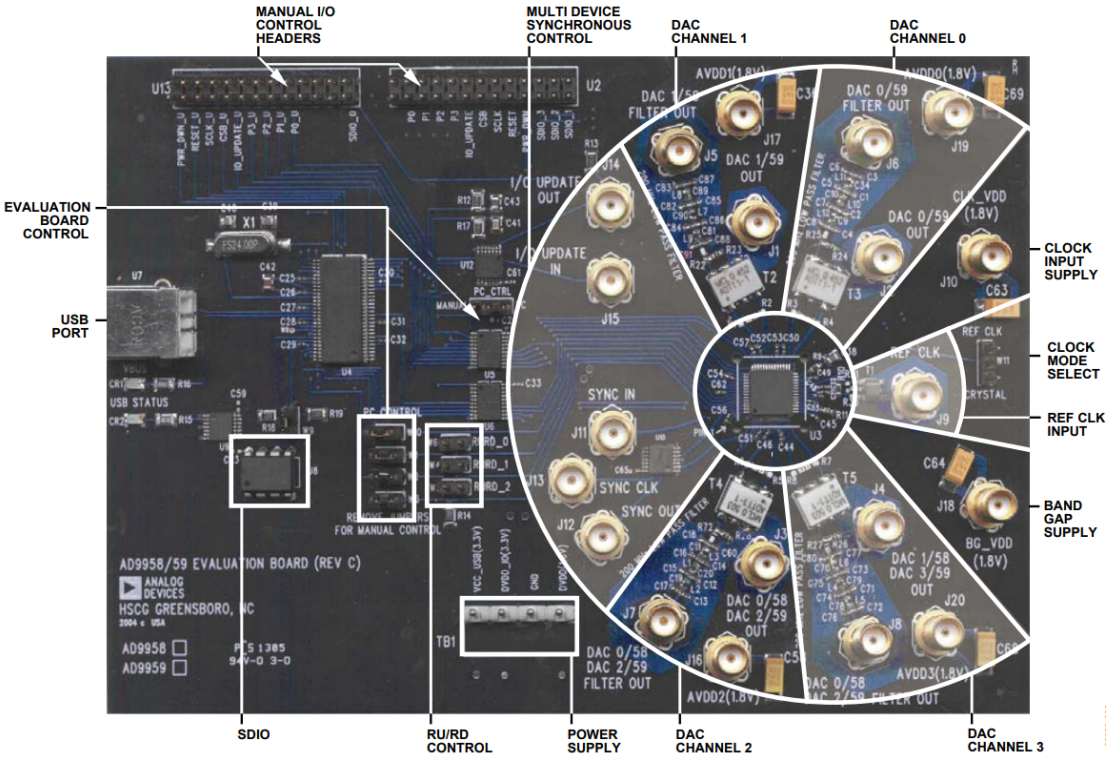

Figure A.1: Annotated photograph of the AD9959 evaluation board, taken from the datasheet. The manual I/O control headers are the interface for AD9959 communication when under manual control from an external controller.

Parts List

- AC/DC power supply (3.3 V, 5 V, 12 V) [ECM40UT34]
- Power distribution board:
  - AC/DC converter (± 15 V) [ECL15UD02]
  - DC/DC converter (5 V to 1.8 V) [MEZD71202A-D]
- 1 × AD9959 (4 channel DDS evaluation board) [Serial number: 3D50DAF53580]
- 2 × Amplifiers with + 21 gain [THS4022EVM]
- 500 MHz oscillator [RFPRO33-500.000]
- Yellow LED (12 V DC)
- 4 × SMA to BNC cables
- SMA to SMA corner joint (for clock)

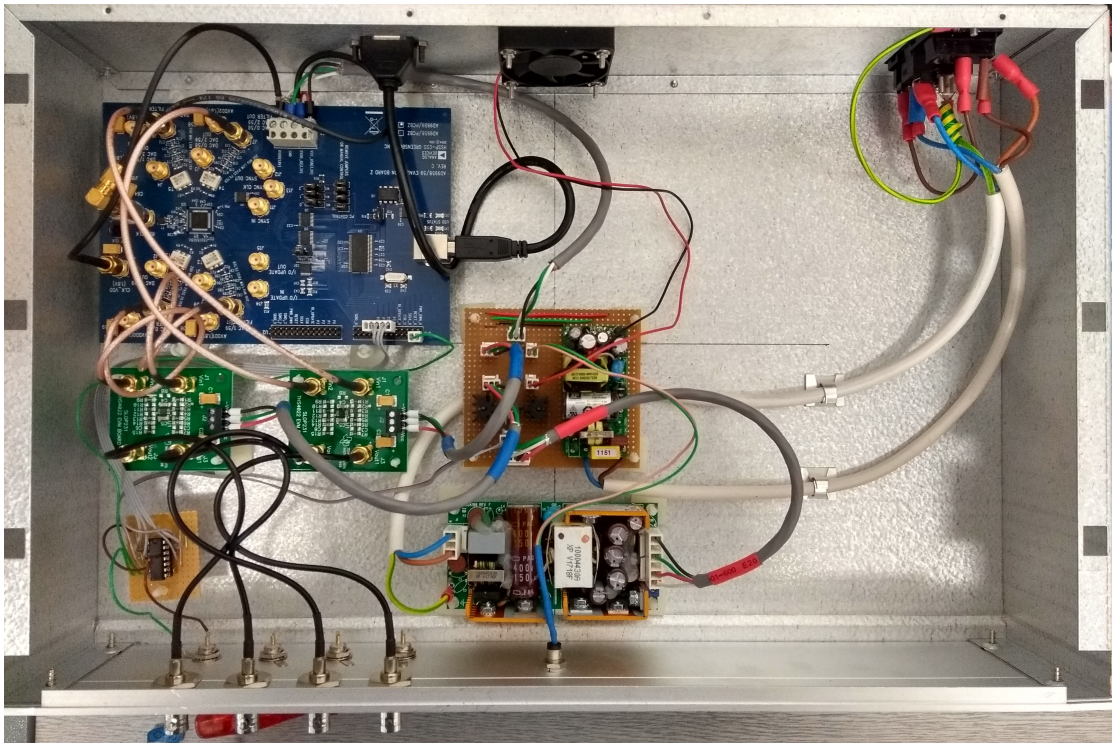

Figure A.2: Photograph inside the 19" rack-mount box of the AD9959 RW function generator. The AD9959 is blue and the amplifiers are green, where they are powered from the power distribution board which is at the centre in brown and shown schematically in figure A.4.

- 4 × 0.25 m SMA to SMA cables (from AD9959 output to amplifiers)
- 2 × 0.25 m SMA to fly leads (for powering clock and AD9959)
- Fan (12 V DC)
- 19" steel rack-mount box [20860-126]
- IEC fused inlet (1.25 A fuse) [BVA01/Z0000/01]
- 3 × 50 Ω line drivers [SN74128N] (for gated mode trigger buffer)
- 1 × USB type B male to female cable
- Heat sink (for DC/DC converter)

The total cost of the parts was $< £500$, and the function generator is shown in figure A.2.

a) b)

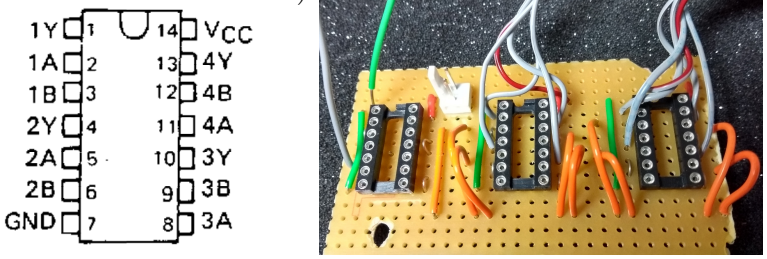

Figure A.3: a) Top view of the SN74128N line driver from the datasheet, where the 2-input NOR gates are A and B and Y is the output. b) Buffer for the double RW function generator, comprised of three 50 Ω line drivers [SN74128N] (only the mounts are shown here) with each A & B logic input shorted.

Triggering

For the digital output trigger from the FPGA to have sufficient drive, a TTL (transistor-transistor logic) buffer uses three 50 Ω line drivers, with each 2-input NOR (A & B) shorted (figure A.3). A signal to RESET places the DAC output to a known state for the synchronisation of multiple AD9959 boards. A high-level voltage on pin P1U on the AD9959 enables the output, while a low-level voltage disables the output.

AD9959 Configuration

The DDS core is powered by a 1.8 V supply, whilst the serial I/O interface requires 3.3 V. The AD9959 has its W7 jumper on PC control and W10, W1 W2, W3 and W9 are all connected for PC control. W4, W5, W6 are all disconnected. For operation, an IEC cable must be connected from mains electricity to the IEC inlet to power the power distribution board (figure A.4), and it must be connected via USB to a Windows PC.

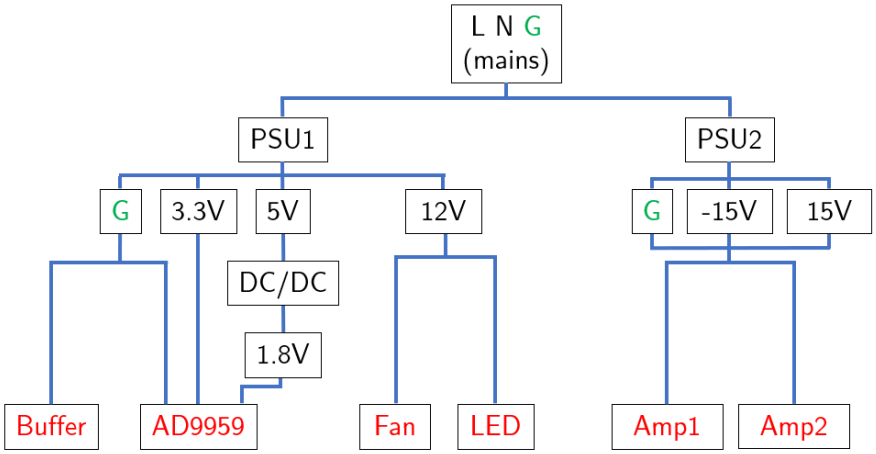

Figure A.4: Schematic of the power distribution board, containing two power supply units (PSU).

Control

Rudimentary firmware was provided with the AD9959 for GUI control, but it did not allow simple modification and could not be integrated into the beamline's existing sequencer system. To overcome this, Dynamic Link Library (DLL) wrappers were written in C++ to allow USB communications and hardware control via LabVIEW™. The USB 2.0 (480 Mb/s) programmable microcontroller on the board side is the Cypress EZ-USB® FX2LP™ [CY7C68013A]. To communicate with the microcontroller, wrappers were built on the Microsoft Visual C++ platform, using the Cypress SuiteUSB C# library 'CyUSB.dll'. The corresponding USB development tool for Microsoft Visual Studio is CySuiteUSB 3.4.7, which provides a programming interface from Windows to the driver.

There are two compiled versions of the code for use in either Windows 7 or Windows 10 operating systems (OS), compilation required the installation of the software development kit (SDK) and '.NET framework' for each OS. This then allows identification, initialisation and closing of the device, while the registry of the AD9959 can be updated using LabVIEW to set amplitude, frequency, phase, and

gated mode. During initialisation, the on-board random-access memory (RAM) is flashed with the new firmware, which is necessary each time the device is powered. LabVIEW programs allow the aforementioned functions to be completed along with toggles for: four or six segment RW; RW direction, i.e. clockwise and counter-clockwise (as viewed from the source end); and a toggle for the amplitude calibration with or without the amplifiers.

Software requirements:

- EZ-USB® FX2LP™ drivers
- CySuiteUSB 3.4.7
- LabVIEW™

Calibration

Amplitude calibration was performed following thermalisation, which is achieved after ~ 4 hours, as the temperature had an effect on the output characteristics.

Amplitude

Using the amplifiers, the maximum amplitude is 6.72 V peak to peak. The amplifiers are not required for RW compression at frequencies around $f_z \approx 10.5$ MHz, in which case the maximum amplitude is 0.65 V peak to peak. The amplitude calibration was performed twice: at ~ 50 kHz with the amplifiers, which is near f_m, and at ~ 10.5 MHz without the amplifiers. The amplitude deviates as a function of frequency from the desired value by $< 1\%$ between 5–15 MHz. The amplitude was found to scale linearly at any frequency.

Timing

The external clock oscillator frequency was measured as 500.01 MHz, which was stable as monitored for a month. Using the amplifiers, there is a $\approx$ 90 ns delay between trigger HIGH and output ON at the maximum amplitude of 6.72 V peak to peak at 10 MHz. The delay between trigger LOW and output OFF is $\approx$ 125 ns at the maximum amplitude of 6.72 V peak to peak at 10 MHz. No significant deviation was seen from these timings for a frequency range of 0.1–30.0 MHz. The sinusoidal signal shows negligible distortion when the output is switched on or off.

Bibliography

Aghion, S., Amsler, C., Ariga, A., Ariga, T., Belov, A. S., Bonomi, G., Bräunig, P., Bremer, J., Brusa, R. S., Cabaret, L., Caccia, M., Caravita, R., Castelli, F., Cerchiari, G., Chlouba, K., Cialdi, S., Comparat, D., Consolati, G., Demetrio, A., Di Noto, L., Doser, M., Dudarev, A., Ereditato, A., Evans, C., Fesel, J., Fontana, A., Forslund, O. K., Gerber, S., Giammarchi, M., Gligorova, A., Gninenko, S., Guatieri, F., Haider, S., Holmestad, H., Huse, T., Jernelv, I. L., Jordan, E., Kaltenbacher, T., Kellerbauer, A., Kimura, M., Koetting, T., Krasnicky, D., Lagomarsino, V., Lebrun, P., Lansonneur, P., Lehner, S., Liberadzka, J., Malbrunot, C., Mariazzi, S., Marx, L., Matveev, V., Mazzotta, Z., Nebbia, G., Nedelec, P., Oberthaler, M., Pacifico, N., Pagano, D., Penasa, L., Petracek, V., Pistillo, C., Prelz, F., Prevedelli, M., Ravelli, L., Rienäcker, B., Røhne, O. M., Rosenberger, S., Rotondi, A., Sacerdoti, M., Sandaker, H., Santoro, R., Scampoli, P., Sorrentino, F., Spacek, M., Storey, J., Strojek, I. M., Testera, G., Tietje, I., Vamosi, S., Widmann, E., Yzombard, P., Zavatarelli, S., and Zmeskal, J. (2015). Positron Bunching and Electrostatic Transport System for the Production and Emission of Dense Positronium Clouds Into Vacuum. *Nuclear Instruments and Methods in Physics Research, Section B: Beam Interactions with Materials and Atoms*, 362:86–92.

Ahmadi, M., Alves, B. X., Baker, C. J., Bertsche, W., Butler, E., Capra, A., Carruth, C., Cesar, C. L., Charlton, M., Cohen, S., Collister, R., Eriksson, S., Evans, A., Evetts, N., Fajans, J., Friesen, T., Fujiwara, M. C., Gill, D. R., Gutierrez, A., Hangst, J. S., Hardy, W. N., Hayden, M. E., Isaac, C. A., Ishida, A., Johnson, M. A., Jones, S. A., Jonsell, S., Kurchaninov, L., Madsen, N., Mathers, M., Maxwell, D., McKenna, J. T., Menary, S., Michan, J. M., Momose, T., Munich, J. J., Nolan, P., Olchanski, K., Olin, A., Pusa, P., Rasmussen, C. O., Robicheaux, F., Sacramento, R. L., Sameed, M., Sarid, E., Silveira, D. M., Stracka, S., Stutter, G., So, C., Tharp, T. D., Thompson, J. E., Thompson, R. I.,

van der Werf, D. P., and Wurtele, J. S. (2017). Antihydrogen Accumulation for Fundamental Symmetry Tests. *Nature Communications*, 8(1):1–6.

Amoretti, M., Amsler, C., Bonomi, G., Bouchta, A., Bowe, P., Carraro, C., Cesar, C. L., Charlton, M., Collier, M. J., Doser, M., Filippini, V., Fine, F. S., Fontana, A., Fujiwara, M. C., Funakoshi, R., Genova, P., Hangst, J. S., Hayano, R. S., Holzscheiter, M. H., Jørgensen, L. V., Lagomarsino, V., Landua, R., Lindelöf, D., Rizzini, E. L., Macrì, M., Madsen, N., Manuzio, G., Marchesotti, M., Montagna, P., Pruys, H., Regenfus, C., Riedler, P., Rochet, J., Rotondi, A., Rouleau, G., Testera, G., Variola, A., Watson, T. L., and van der Werf, D. P. (2002). Production and Detection of Cold Antihydrogen Atoms. *Nature*, 419(6906):456–459.

Anderson, C. D. (1933). The Positive Electron. *Physical Review*, 43(6):491–494.

Andresen, G. B., Ashkezari, M. D., Baquero-Ruiz, M., Bertsche, W., Bowe, P. D., Butler, E., Cesar, C. L., Chapman, S., Charlton, M., Deller, A., Eriksson, S., Fajans, J., Friesen, T., Fujiwara, M. C., Gill, D. R., Gutierrez, A., Hangst, J. S., Hardy, W. N., Hayden, M. E., Humphries, A. J., Hydomako, R., Jenkins, M. J., Jonsell, S., Jørgensen, L. V., Kurchaninov, L., Madsen, N., Menary, S., Nolan, P., Olchanski, K., Olin, A., Povilus, A., Pusa, P., Robicheaux, F., Sarid, E., Nasr, S. S. E., Silveira, D. M., So, C., Storey, J. W., Thompson, R. I., van der Werf, D. P., Wurtele, J. S., and Yamazaki, Y. (2010). Trapped Antihydrogen. *Nature*, 468(7324):673–676.

Baker, C. J., Edwards, D., Isaac, C. A., Telle, H. H., van der Werf, D. P., and Charlton, M. (2018). Excitation of positronium: From the Ground State to Rydberg Levels. *Journal of Physics B: Atomic, Molecular and Optical Physics*, 51(3):035006.

Baker, C. J., Isaac, C. A., Edwards, D., Evans, H. T., Clayton, R., van der Werf, D. P., and Charlton, M. (2020). Investigation of Buffer Gas Trapping of Positrons. *Journal of Physics B: Atomic, Molecular and Optical Physics*, 53(18):185201.

Beck, B. R. (1990). *Measurement of the Magnetic and Temperature Dependence of the Electron-Electron Anisotropic Temperature Relaxation Rate*. PhD thesis, University of California, San Diego.

Beck, B. R., Fajans, J., and Malmberg, J. H. (1996). Temperature and Anisotropic-Temperature Relaxation Measurements in Cold, Pure-Electron Plasmas. *Physics of Plasmas*, 3(4):1250–1258.

Briggs, M. S., Connaughton, V., Wilson-Hodge, C., Preece, R. D., Fishman, G. J., Kippen, R. M., Bhat, P. N., Paciesas, W. S., Chaplin, V. L., Meegan, C. A., Von Kienlin, A., Greiner, J., Dwyer, J. R., and Smith, D. M. (2011). Electron-Positron Beams From Terrestrial Lightning Observed With Fermi GBM. *Geophysical Research Letters*, 38(2):1–5.

Brown, L. S. and Gabrielse, G. (1982). Precision Spectroscopy of a Charged Particle in an Imperfect Penning Trap. *Physical Review A*, 25(4):2423–2425.

Brown, L. S. and Gabrielse, G. (1986). Geonium Theory: Physics of a Single Electron or Ion in a Penning Trap.

Canter, K. F. and Mills Jr., A. P. (1982). Slow Positron Beam Design Notes. *Canadian Journal of Physics*, 60(4):551–557.

Cassidy, D. B. (2018). Experimental Progress in Positronium Laser Physics. *European Physical Journal D*, 72(3).

Cassidy, D. B., Deng, S. H. M., Greaves, R. G., and Mills, A. P. (2006a). Accumulator for the Production of Intense Positron Pulses. *Review of Scientific Instruments*, 77(7):073106.

Cassidy, D. B., Deng, S. H. M., Tanaka, H. K. M., and Mills, A. P. (2006b). Single Shot Positron Annihilation Lifetime Spectroscopy. *Applied Physics Letters*, 88(19):137–140.

Charlton, M. and Humberston, J. W. (2000). *Positron Physics*. Cambridge University Press.

Chen, F. F. (2016). *Introduction to Plasma Physics and Controlled Fusion*. Springer International Publishing, Cham.

Chen, H., Wilks, S. C., Bonlie, J. D., Chen, S. N., Cone, K. V., Elberson, L. N., Gregori, G., Meyerhofer, D. D., Myatt, J., Price, D. F., Schneider, M. B., Shepherd, R., Stafford, D. C., Tommasini, R., van Maren, R., and Beiersdorfer, P. (2009). Making Relativistic Positrons Using Ultraintense Short Pulse Lasers. *Physics of Plasmas*, 16(12):122702.

Cherry, W. H. (1958). PhD thesis, Princeton University.

Clarke, J., van der Werf, D. P., Griffiths, B., Beddows, D. C., Charlton, M., Telle, H. H., and Watkeys, P. R. (2006). Design and Operation of a Two-Stage Positron Accumulator. *Review of Scientific Instruments*.

Coleman, P. (2000). *Positron Beams and Their Applications*. World Scientific.

Danielson, J. R., Dubin, D. H. E., Greaves, R. G., and Surko, C. M. (2015). Plasma and Trap-Based Techniques for Science With Positrons. *Reviews of Modern Physics*, 87(1):247–306.

de Swart, J. G., Bertone, G., and van Dongen, J. (2017). How Dark Matter Came to Matter. *Nature Astronomy*, 1(3):0059.

Dehmelt, H. (1968). Radiofrequency Spectroscopy of Stored Ions I: Storage. In *Advances in Atomic and Molecular Physics*, volume 617, pages 53–72. Academic Press.

Dehmelt, H. (1969). Radiofrequency Spectroscopy of Stored Ions II: Spectroscopy. In *Advances in Atomic and Molecular Physics*, volume 5, pages 109–154. Academic Press.

Dehmelt, H., Nagourney, W., and Sandberg, J. (1986). Self-Excited Mono-Ion Oscillator. *Proceedings of the National Academy of Sciences*, 83(16):5761–5763.

Dehmelt, H. G. and Walls, F. L. (1968). "Bolometric" Technique for the RF Spectroscopy of Stored Ions. *Physical Review Letters*, 21(3):127–131.

Deller, A. (2013). *Positron Accumulation and Laser Excitation of the Positronium Atom*. PhD thesis, Swansea University.

Deller, A. (2019). SSPALS: A Tool for Studying Positronium. *Nuclear Instruments and Methods in Physics Research, Section A: Accelerators, Spectrometers, Detectors and Associated Equipment*, 922(August 2018):91–97.

Deller, A., Edwards, D., Mortensen, T., Isaac, C. A., van der Werf, D. P., Telle, H. H., and Charlton, M. (2015). Exciting Positronium With a Solid-State UV Laser: The Doppler-Broadened Lyman-α Transition. *Journal of Physics B: Atomic, Molecular and Optical Physics*, 48(17):175001.

Deller, A., Mortensen, T., Isaac, C. A., van der Werf, D. P., and Charlton, M. (2014). Radially Selective Inward Transport of Positrons in a Penning-Malmberg Trap. *New Journal of Physics*, 16.

Di Domizio, S., Krasnicky, D., Lagomarsino, V., Testera, G., Vaccarone, R., and Zavatarelli, S. (2015). Toward Sub-Kelvin Resistive Cooling and Non Destructive Detection of Trapped Non-Neutral Electron Plasma. *Journal of Instrumentation*, 10(1).

Dirac, P. A. M. (1928). The Quantum Theory of the Electron. *Proceedings of the Royal Society of London. Series A, Containing Papers of a Mathematical and Physical Character*, 117(778):610–624.

Dirac, P. A. M. (1930). A Theory of Electrons and Protons. *Proceedings of the Royal Society of London. Series A, Containing Papers of a Mathematical and Physical Character*, 126(801):360–365.

Dirac, P. A. M. (1931). Quantised Singularities in the Electromagnetic Field. *Proceedings of the Royal Society of London. Series A, Containing Papers of a Mathematical and Physical Character*, 133(821):60–72.

Earnshaw, S. (1848). On the Nature of the Molecular Forces Which Regulate the Constitution of the Luminiferous Ether. *Transactions of the Cambridge Philosophical Society*, 7:97.

Ebrahimi, M. S., Guo, Z., Vogel, M., Wiesel, M., Birkl, G., and Quint, W. (2018). Resistive Cooling of Highly Charged Ions in a Penning Trap to a Fluidlike State. *Physical Review A*, 98(2):1–10.

Edwards, D. (2019). *Efficient Excitation of Rydberg Positronium*. PhD thesis, Swansea University.

Eggleston, D. L., Driscoll, C. F., Beck, B. R., Hyatt, A. W., and Malmberg, J. H. (1992). Parallel Energy Analyzer for Pure Electron Plasma Devices. *Physics of Fluids B*, 4(10):3432–3439.

Enomoto, Y., Kuroda, N., Michishio, K., Kim, C. H., Higaki, H., Nagata, Y., Kanai, Y., Torii, H. A., Corradini, M., Leali, M., Lodi-Rizzini, E., Mascagna,

V., Venturelli, L., Zurlo, N., Fujii, K., Ohtsuka, M., Tanaka, K., Imao, H., Nagashima, Y., Matsuda, Y., Juhász, B., Mohri, A., and Yamazaki, Y. (2010). Synthesis of Cold Antihydrogen in a Cusp Trap. *Physical Review Letters*, 105(24):1–4.

Evans, C. (2014). *Design and Implementation of a Third Stage Positron Accumulator Device*. MSc thesis, Swansea University.

Farrar, G. R. and Shaposhnikov, M. E. (1993). Baryon Asymmetry of the Universe in the Minimal Standard Model. *Physical Review Letters*, 71(1):210–210.

Feng, X., Charlton, M., Holzscheiter, M., Lewis, R. a., and Yamazaki, Y. (1996). Tank Circuit Model Applied to Particles in a Penning Trap. *Journal of Applied Physics*, 79(1996):8.

Fitzakerley, D. W., George, M. C., Hessels, E. A., Skinner, T. D. G., Storry, C. H., Weel, M., Gabrielse, G., Hamley, C. D., Jones, N., Marable, K., Tardiff, E., Grzonka, D., Oelert, W., and Zielinski, M. (2016). Electron-Cooled Accumulation of 4E9 Positrons for Production and Storage of Aantihydrogen Atoms. *Journal of Physics B: Atomic, Molecular and Optical Physics*, 49(6):064001.

Gabrielse, G., Bowden, N. S., Oxley, P., Speck, A., Storry, C. H., Tan, J. N., Wessels, M., Grzonka, D., Oelert, W., Schepers, G., Sefzick, T., Walz, J., Pittner, H., Hänsch, T. W., and Hessels, E. A. (2002). Background-Free Observation of Cold Antihydrogen With Field-Ionization Analysis of its States. *Physical Review Letters*, 89(21):2–5.

Gabrielse, G., Haarsma, L., and Rolston, S. L. (1989). Open-Endcap Penning Traps for High Precision Experiments. *International Journal of Mass Spectrometry and Ion Processes*, 88(2-3):319–332.

Gabrielse, G. and Mackintosh, F. C. (1984). Cylindrical Penning Traps with Orthogonalized Anharmonicity Compensation. *International Journal of Mass Spectrometry and Ion Processes*, 57(1):1–17.

Greaves, R. G. and Moxom, J. M. (2008). Compression of Trapped Positrons in a Single Particle Regime by a Rotating Electric Field. *Physics of Plasmas*, 15(7).

Greaves, R. G. and Surko, C. M. (2000). Inward Transport and Compression of a Positron Plasma by a Rotating Electric Field. *Physical Review Letters*, 85(9):1883–1886.

Greaves, R. G. and Surko, C. M. (2001). Radial Compression and Inward Transport of Positron Plasmas Using a Rotating Electric Field. *Physics of Plasmas*, 8(5):1879–1885.

Gribakin, G. F., Young, J. A., and Surko, C. M. (2010). Positron-Molecule Interactions: Resonant Attachment, Annihilation, and Bound States. *Reviews of Modern Physics*, 82(3):2557–2607.

Grieder, P. K. F. (2010). *Exentsive Air Showers and High Energy Phenomena*. Springer Berlin Heidelberg, Berlin, Heidelberg.

Haarsma, L., Abdullah, K., and Gabrielse, G. (1995). Extremely Cold Positrons Accumulated Electronically in Ultrahigh Vacuum. *Physical Review Letters*, 75(5):806–809.

Hart, G. W. and Peterson, B. G. (2006). Finding the Radial Parallel Temperature Profile in a Non-Neutral Plasma Using Equilibrium Calculations on Experimental Data. *Physics of Plasmas*, 13(2):022101.

Hasegawa, T., Jensen, M., and Bollinger, J. (2005). Stability of a Penning Trap With a Quadrupole Rotating Electric Field. *Physical Review A*, 71(2):023406.

Hawari, A. I., Gidley, D. W., Moxom, J., Hathaway, A. G., and Mukherjee, S. (2011). Operation and Testing of the PULSTAR Reactor Intense Slow Positron Beam and PALS Spectrometers. *Journal of Physics: Conference Series*, 262(1):2–6.

He, Z. (2001). Review of the Shockley-Ramo Theorem and its Application in Semiconductor Gamma-Ray Detectors. *Nuclear Instruments and Methods in Physics Research Section A: Accelerators, Spectrometers, Detectors and Associated Equipment*, 463(1-2):250–267.

Huang, X. P., Anderegg, F., Hollmann, E. M., Driscoll, C. F., and O'Neil, T. M. (1997). Steady-State Confinement of Non-Neutral Plasmas by Rotating Electric Fields. *Physical Review Letters*, 78(5):875–879.

Hugenschmidt, C., Löwe, B., Mayer, J., Piochacz, C., Pikart, P., Repper, R., Stadlbauer, M., and Schreckenbach, K. (2008). Unprecedented Intensity of a Low-Energy Positron Beam. *Nuclear Instruments and Methods in Physics Research, Section A: Accelerators, Spectrometers, Detectors and Associated Equipment*, 593(3):616–618.

Hyatt, A. W., Driscoll, C. F., and Malmberg, J. H. (1987). Measurement of the Anisotropic Temperature Relaxation Rate in a Pure Electron Plasma. *Physical Review Letters*, 59(26):2975–2978.

Imao, H., Michishio, K., Kanai, Y., Kuroda, N., Enomoto, Y., Higaki, H., Kira, K., Mohri, A., Torii, H. A., Nagata, Y., Kim, C., Matsuda, Y., Nagashima, Y., and Yamazaki, Y. (2010). Positron Accumulation and Manipulation for Antihydrogen Synthesis. *Journal of Physics: Conference Series*, 225:012018.

Isaac, C. A. (2010). *Axialisation of Particles in a Penning-type Trap by the Application of a Rotating Dipole Electric Field and its Application to Positron Accumulation.* PhD thesis, Swansea University.

Isaac, C. A. (2013). Motional Sideband Excitation Using Rotating Electric Fields. *Physical Review A - Atomic, Molecular, and Optical Physics*, 87(4):1–7.

Isaac, C. A., Baker, C. J., Mortensen, T., van der Werf, D. P., and Charlton, M. (2011). Compression of Positron Clouds in the Independent Particle Regime. *Physical Review Letters*.

Itano, W. M., Bergquist, J. C., Bollinger, J. J., and Wineland, D. J. (1995). Cooling Methods in Ion Traps. *Physica Scripta*, T59:106–120.

Jackson, J. D. (1998). *Classical Electrodynamics*. Wiley, third edition.

Jean, Y. C., Mallon, P. E., and Schrader, D. M. (2003). *Principles and Applications of Positron and Positronium Chemistry*, volume 1. World Scientific.

Jeffries, J., Barlow, S., and Dunn, G. (1983). Theory of Space-Charge Shift of Ion Cyclotron Resonance Frequencies. *International Journal of Mass Spectrometry and Ion Processes*, 54(1-2):169–187.

Jørgensen, L. V., Amoretti, M., Bonomi, G., Bowe, P. D., Canali, C., Carraro, C., Cesar, C. L., Charlton, M., Doser, M., Fontana, A., Fujiwara, M. C., Funakoshi,

R., Genova, P., Hangst, J. S., Hayano, R. S., Kellerbauer, A., Lagomarsino, V., Landua, R., Lodi Rizzini, E., Macrì, M., Madsen, N., Mitchard, D., Montagna, P., Rotondi, A., Testera, G., Variola, A., Venturelli, L., van der Werf, D. P., and Yamazaki, Y. (2005). New Source of Dense, Cryogenic Positron Plasmas. *Physical Review Letters*, 95(2):1–5.

Kaltenbacher, T., Caspers, F., Doser, M., Kellerbauer, A., and Pribyl, W. (2011). Resistive Cooling Circuits for Charged Particle Traps Using Crystal Resonators. *Review of Scientific Instruments*, 82(11).

Knoll, G. F. (2010). *Radiation Detection and Measurement*. Number 4. Wiley, fourth edition.

Knoop, M., Madsen, N., and Thompson, R. C. (2016). *Trapped Charged Particles*. Advanced Textbooks in Physics. World Scientific (Europe).

Kurihara, T., Yagishita, A., Enomoto, A., Kobayashi, H., Shidara, T., Shirakawa, A., Nakahara, K., Saitou, H., Inoue, K., Nagashima, Y., Hyodo, T., Nagai, Y., Hasegawa, M., Inoue, Y., Kogure, Y., and Doyama, M. (2000). Intense positron beam at KEK. *Nuclear Instruments and Methods in Physics Research, Section B: Beam Interactions with Materials and Atoms*, 171(1):164–171.

Liszkay, L., Kajcsos, Z., Barthe, M.-F., Henry, L., Duplâtre, G., and Nagy, A. (2002). Improved Tungsten Moderator Structures for Slow Positron Beams. *Applied Surface Science*, 194(1-4):16–19.

Lynn, K. G., Gramsch, E., Usmar, S. G., and Sferlazzo, P. (1989). Development of a Cone-Geometry Positron Moderator. *Applied Physics Letters*, 55(1):87–89.

Major, F. G., Gheorghe, V. N., and Werth, G. (2005). *Charged Particle Traps*, volume 37 of *Springer Series on Atomic, Optical, and Plasma Physics*. Springer-Verlag, Berlin/Heidelberg.

Malmberg, J. H. and Degrassie, J. S. (1975). Properties of Nonneutral Plasma. *Physical Review Letters*, 35(9):577–580.

Malmberg, J. H. and Driscoll, C. F. (1980). Long-Time Containment of a Pure Electron Plasma. *Physical Review Letters*, 44(10):654–657.

Marler, J. P. and Surko, C. M. (2005). Positron-Impact Ionization, Positronium Formation, and Electronic Excitation Cross Sections for Diatomic Molecules. *Physical Review A*, 72(6):062713.

Mills, A. P. and Gullikson, E. M. (1986). Solid Neon Moderator for Producing Slow Positrons. *Applied Physics Letters*, 49(17):1121–1123.

Mortensen, T. (2013). *Manipulation of the Magnetron Orbits of Particles and Clouds in a Two-Stage Buffer Gas Accumulator*. PhD thesis, Swansea University.

Mortensen, T., Deller, A., Isaac, C. A., van der Werf, D. P., Charlton, M., and Machacek, J. R. (2013). Manipulation of the Magnetron Orbit of a Positron Cloud in a Penning Trap. *Physics of Plasmas*, 20(1):012124.

Murphy, T. J. and Surko, C. M. (1992). Positron Trapping in an Electrostatic Well by Inelastic Collisions With Nitrogen Molecules. *Physical Review A*, 46(9):5696–5705.

Niang, S., Charlton, M., Choi, J. J., Chung, M., Cladé, P., Comini, P., Crivelli, P., Crépin, P. P., Dalkarov, O., Debu, P., Dodd, L., Douillet, A., Froehlich, P., Gafriller, J., Guellati, S., Heinrich, J., Hervieux, P. A., Hilico, L., Husson, A., Indelicato, P., Janka, G., Jonsell, S., Karr, J. P., Kim, B. H., Kim, E. S., Kim, S. K., Kleyheeg, A., Ko, Y., Kosinski, T., Kuroda, N., Latacz, B., Lee, H., Lee, J., Leite, A. M., Lim, E., Liszkay, L., Louvradoux, T., Lunney, D., Lévéque, K., Manfredi, G., Mansoulié, B., Matusiak, M., Mornacchi, G., Nesvizhevsky, V. V., Nez, F., Nishi, R., Nourbaksh, S., Park, K. H., Paul, N., Pérez, P., Radics, B., Regenfus, C., Reynaud, S., Roussé, J. Y., Rubbia, A., Rzadkiewicz, J., Sacquin, Y., Schmidt-Kaler, F., Staszczak, M., Tuchming, B., Vallage, B., van der Werf, D. P., Voronin, A., Welker, A., Wolf, S., Won, D., Wronka, S., Yamazaki, Y., Yoo, K. H., and Baker, C. J. (2020). Accumulation of Positrons fFom a LINAC Based Source. *Acta Physica Polonica A*, 137(2):164–166.

Northrop, T. G. (1961). The Guiding Center Approximation to Charged Particle Motion. *Annals of Physics*, 15(1):79–101.

Notte, J. and Fajans, J. (1994). The Effect of Asymmetries on Non-Neutral Plasma Confinement Time. *Physics of Plasmas*, 1(5):1123–1127.

Oppenheimer, J. R. (1930a). Note on the Theory of the Interaction of Field and Matter. *Physical Review*, 35(5):461–477.

Oppenheimer, J. R. (1930b). On the Theory of Electrons and Protons. *Physical Review*, 35(5):562–563.

Paul, W. (1990). Electromagnetic Traps for Charged and Neutral Particles (Nobel Lecture). *Angewandte Chemie International Edition in English*, 29(7):739–748.

Peebles, P. J. and Ratra, B. (2003). The Cosmological Constant and Dark Energy. *Reviews of Modern Physics*, 75(2):559–606.

Pozar, D. (2011). *Microwave Engineering*. Wiley, 4th edition.

Ramo, S. (1939). Currents Induced by Electron Motion. *Proceedings of the IRE*, 27(9):584–585.

Rich, A. (1981). Recent Experimental Advances in Positronium Research. *Reviews of Modern Physics*, 53(1):127–165.

Rovelli, C. (2018). *Reality Is Not What It Seems: The Journey to Quantum Gravity*. Penguin Publishing Group.

Sarri, G., Schumaker, W., Di Piazza, A., Vargas, M., Dromey, B., Dieckmann, M. E., Chvykov, V., Maksimchuk, A., Yanovsky, V., He, Z. H., Hou, B. X., Nees, J. A., Thomas, A. G., Keitel, C. H., Zepf, M., and Krushelnick, K. (2013). Table-Top Laser-Based Source of Femtosecond, Collimated, Ultrarelativistic Positron Beams. *Physical Review Letters*, 110(25):1–5.

Sato, K., Xu, Q., Yoshiie, T., Sano, T., Kawabe, H., Nagai, Y., Nagumo, K., Inoue, K., Toyama, T., Oshima, N., Kinomura, A., and Shirai, Y. (2015). Development of a Mono-Energetic Positron Beam Line at the Kyoto University Research Reactor. *Nuclear Instruments and Methods in Physics Research, Section B: Beam Interactions with Materials and Atoms*, 342:104–107.

Savage, T. (2019). *Towards Non-Destructive Diagnostics of Trapped Positrons*. MSc thesis, Swansea University.

Schultz, P. and Lynn, K. (1988). Interaction of Positron Beams. *Rev. Mod. Phys.*, 60(3):701–779.

Schwinberg, P. B., van Dyck, R. S., and Dehmelt, H. G. (1981). Trapping and Thermalization of Positrons for Geonium Spectroscopy. *Physics Letters A*, 81(2-3):119–120.

Shi, Q. and Kanoun, O. (2015). Wire Fault Diagnosis in the Frequency Domain by Impedance Spectroscopy. *IEEE Transactions on Instrumentation and Measurement*, 64(8):2179–2187.

Shockley, W. (1938). Currents to Conductors Induced by a Moving Point Charge. *Journal of Applied Physics*, 9(10):635–636.

Siegel, R. W. (1980). Positron Annihilation Spectroscopy. *Annual Review of Materials Science*, 10(1):393–425.

Smorra, C., Sellner, S., Borchert, M. J., Harrington, J. A., Higuchi, T., Nagahama, H., Tanaka, T., Mooser, A., Schneider, G., Bohman, M., Blaum, K., Matsuda, Y., Ospelkaus, C., Quint, W., Walz, J., Yamazaki, Y., and Ulmer, S. (2017). A Parts-Per-Billion Measurement of the Antiproton Magnetic Moment. *Nature*, 550(7676):371–374.

Sullivan, J. P., Jones, A., Caradonna, P., Makochekanwa, C., and Buckman, S. J. (2008). A Positron Trap and Beam Apparatus for Atomic and Molecular Scattering Experiments. *Review of Scientific Instruments*, 79(11):113105.

Surko, C. M., Gribakin, G. F., and Buckman, S. J. (2005). Low-Energy Positron Interactions With Atoms and Molecules. *Journal of Physics B: Atomic, Molecular and Optical Physics*, 38(6).

Tuomisto, F. and Makkonen, I. (2013). Defect Identification in Semiconductors With Positron Annihilation: Experiment and Theory. *Reviews of Modern Physics*, 85(4):1583–1631.

Ulmer, S., Blaum, K., Kracke, H., Mooser, A., Quint, W., Rodegheri, C. C., and Walz, J. (2013). A Cryogenic Detection System at 28.9 MHz for the Non-destructive Observation of a Single Proton at Low Particle Energy. *Nuclear Instruments and Methods in Physics Research, Section A: Accelerators, Spectrometers, Detectors and Associated Equipment*, 705:55–60.

van der Werf, D. P., Isaac, C. A., Baker, C. J., Mortensen, T., and Charlton, M. (2012). Compression of Positron Clouds Using Rotating Wall Electric Fields. *Hyperfine Interactions*, 212(1-3):125–132.

van Veen, A., Schut, H., Labohm, F., and De Roode, J. (1999). Positron Extraction and Transport in a Nuclear-Reactor-Based Positron Beam. *Nuclear Instruments and Methods in Physics Research, Section A: Accelerators, Spectrometers, Detectors and Associated Equipment*, 427(1-2):266–270.

Vehanen, A., Lynn, K. G., Schultz, P. J., and Eldrup, M. (1983). Improved Slow-Positron Yield Using a Single Crystal Tungsten Moderator. *Applied Physics A Solids and Surfaces*, 32(3):163–167.

Vogel, M. (2018). *Particle Confinement in Penning Traps*, volume 100. Springer.

Vogel, M., Haeffner, H., Hermanspahn, K., Stahl, S., Steinmann, J., and Quint, W. (2014). Resistive and Sympathetic Cooling of Highly-Charged-Ion Clouds in a Penning Trap. *Physical Review A - Atomic, Molecular, and Optical Physics*, 90(4):1–12.

Wagner, A., Butterling, M., Liedke, M. O., Potzger, K., and Krause-Rehberg, R. (2018). Positron Annihilation Lifetime and Doppler Broadening Spectroscopy at the Elbe Facility. *AIP Conference Proceedings*, 1970.

Wardle, J. F., Homan, D. C., Ojha, R., and Roberts, D. H. (1998). Electron-Positron Jets Associated With the Quasar 3C279. *Nature*, 395(6701):457–461.

Watkeys, P. R. (2008). *Towards Laser Excitation of Positronium and Advances in Positron Accumulation Techniques*. PhD thesis, Swansea University.

Werth, G., Gheorghe, V. N., and Major, F. G. (2009). *Charged Particle Traps II*, volume 54 of *Springer Series on Atomic, Optical, and Plasma Physics*. Springer Berlin Heidelberg, Berlin, Heidelberg.

Wineland, D. J. and Dehmelt, H. G. (1975). Principles of the Stored Ion Calorimeter. *Journal of Applied Physics*, 46(2):919–930.

Winters, D. F. A., Vogel, M., Segal, D. M., and Thompson, R. C. (2006). Electronic Detection of Charged Particle Effects in a Penning Trap. *Journal of Physics B: Atomic, Molecular and Optical Physics*, 39(14):3131–3143.

Publications List

- Baker, C. J., Isaac, C. A., Edwards, D., Evans, H. T., Clayton, R., van der Werf, D. P., and Charlton, M. (2020). Investigation of Buffer Gas Trapping of Positrons. *Journal of Physics B: Atomic, Molecular and Optical Physics*, 53(18):185201.
- Evans, H. T., Isaac, C. A. (2021). Cronni Plasma o Bositronau. *Gwerddon*, 33:55–67.